Numerical Analysis of Electrical Parameter Effects on a Nanosecond Pulsed Dielectric Barrier Discharge Actuator

by

Katrina Mullane

A thesis submitted to the
Faculty of Graduate and Postdoctoral Affairs
in partial fulfillment of the requirements
for the degree of

Master of Applied Science in Aerospace Engineering

Department of Mechanical and Aerospace Engineering
Carleton University
Ottawa, Canada

January 22, 2025

Abstract

Dielectric barrier discharge (DBD) plasma actuators are active flow control devices that have shown promising capabilities of enhancing aerodynamic performance. To study the underling mechanisms occurring within the plasma produced by a nanosecond pulsed DBD actuator and the effect the input electrical parameters have on plasma generation, a numerical model has been developed. Because this work is focused on the plasma behaviour, the impact on the bulk flow has been neglected. The plasma properties analysed here include the charged particle densities, surface charge along the dielectric, and the ion sheath propagation. As the applied voltage amplitude and pulse duration was increased, a larger plasma region formed due to the electric field expanding further throughout the domain. The results highlight a significant relationship between the residual surface charge on the dielectric and the propagation of the ion sheath. The ion sheath speed showed to be dependent on a combination of the residual surface charge and secondary electron emission. Additionally, the results suggest the presence of an electron void at the end-phase of the voltage cycle significantly effects the plasma formation by reducing ionization ahead of the plasma region and limiting propagation downstream. Analysing the plasma properties over five voltage cycles showed a significant time dependency of the parameters during the first two voltage cycles before reaching a quasi-steady state for the remaining cycles, indicating time-averaging plasma parameters over the first few cycles of operation would not produce representative results.

Acknowledgments

I would like to thank my supervisor, Dr. Jason Etele, for his guidance and mentorship while completing this work. The opportunities provided to travel and share my work at the AIAA conference in Las Vegas was invaluable. Additionally, I would like to acknowledge Dr. Aliaksandr Murzionak for developing the foundation of this work and sharing his knowledge whenever requested.

I would also like to extend my gratitude to Carleton University and the Department of Mechanical and Aerospace Engineering for allowing me to pursue this degree and providing such an excellent learning experience. Lastly, I would like to extend a special thank you to my friends and family for their enthusiasm and unwavering support.

Contents

List of Tables

List of Figures

List of Acronyms

Acronym	Definition
AC	Alternating current
DBD	Dielectric barrier discharge
EHD	Electrohydrodynamic
e^-	Electron
GCI	Grid convergence index
H.O.T	Higher order terms
N_2	Nitrogen
N_2^+	Nitrogen ion
N_4^+	Tetranitrogen cation
NO	Nitric Oxide
NS	Nanosecond
O^-	Oxygen anion
O_2	Oxygen
O_2^+	Oxygen ion
O_4^+	Tetraoxygen cation
PIC	Particle-in-cell
VW	Variable weight

Nomenclature

Symbol	Unit	Definition
A	V	Applied voltage amplitude
B	s	Period of voltage signal
$\mathbf{B}$	T	Magnetic field
c	m/s	Speed of light $(3 \cdot 10^8)$
D_k	m^2/s	Diffusion coefficient of particle k
E	J	Total energy
$\mathbf{E}$	V/m	Electric field
e_0	C	Elementary charge (1.6022×10^{-19})
e_i	-	Discretization error of i^{th} grid
E_i	-	Estimated error of i^{th} grid
$\mathbf{f}$	N/m^3	Volumetric force
$\mathbf{f}_E$	N/m^3	Electrodynamic force
f_i	-	Numerical solution of i^{th} grid
h_i	-	Normalized spacing of i^{th} grid
$\mathbf{J}$	A/m^2	Current density
k_B	J/K	Boltzmann constant $(1.3806 \cdot 10^{-23})$
$\mathbf{n}$	-	Surface normal vector
N_k	m^{-3}	Number density of particle k
P	Pa	Pressure
p	-	Order of convergence
$\mathbf{q}$	W/m^2	Heat flux vector
r	-	Grid refinement ratio

S_k	$m^{-3}s^{-1}$	Source term of particle k
s_k	-	Charge sign of particle k
t	s	Time
T	K	Temperature
$\mathbf{V}$	m/s	Velocity
V	m^3	Volume
V_{d_e}	m/s	Electron drift velocity
α	m^{-1}	Ionization rate
β	m^3/s	Recombination rate
δ_σ	-	Surface charge delta
ε	-	Relative error
ϵ	F/m	Absolute permittivity
ϵ_0	F/m	Absolute permittivity of a vacuum ($8.85 \cdot 10^{-12}$)
ϵ_r	-	Relative permittivity
$\mathbf{\Gamma}_k$	$m^{-2}s^{-1}$	Particle k flux
γ	-	Secondary electron coefficient
ϕ_E	V	Electric potential
ψ	-	Van Leer limiter
ρ	kg/m^3	Mass density
ρ_C	C/m^3	Charge density
σ_C	C/m^2	Surface charge density
$\boldsymbol{\tau}$	N/m^2	Stress tensor
μ_B	H/m	Vacuum permeability ($4\pi 10^{-7}$)
μ_k	m^2/Vs	Mobility of particle k

Subscript

$diel$	Dielectric region
e	Electron
$fluid$	Fluid region
k	Species k (electron or positive ion)
$\parallel$	Parallel
$\perp$	Perpendicular
$+$	Positive ion

Chapter 1

Introduction

1.1 Dielectric barrier discharge plasma actuators

Active and passive flow control techniques have long been used in the aerospace industry to manipulate flow fields and influence aerodynamic performance. The main difference between the techniques is that active flow control methods require some sort of energy input into the system to affect the flow, where passive flow control methods do not. Actuators and sensors are typical devices used as active flow control methods, where modifying the geometry, surface roughness, or porosity of the material to influence the flow are examples of passive flow control techniques. Both applications have advantages and disadvantages; active flow control can offer greater flexibility and adaptability for flow control in some cases, however, it does require an energy source and can be difficult to integrate into systems. Passive flow control techniques can be technically simpler to implement and economically efficient compared to active flow control techniques, however, passive flow control techniques cannot be turned on or off if required.

An active flow control method currently of interest in the aerospace industry is

dielectric barrier discharge (DBD) plasma actuators due to their lightweight design and fast response time. Additionally, DBD actuators are electronic and therefore do not require any moving parts. DBD actuators are simple devices consisting of two electrodes; one electrode mounted on the surface exposed to the flow and connected to a voltage supply, with the other electrode embedded in a dielectric barrier and grounded. When supplied with an applied voltage, a DBD actuator generates an electric field over a small region above the dielectric surface, accelerating free electrons and ionizing the surrounding air generating non-thermal plasma. This new presence of plasma can be used to modify the airflow and has shown to be effective at preventing or exciting boundary layer separation and modifying the properties of shock waves. Additional applications include aircraft and wind turbine blade de-icing or ice mitigation via the thermal effects produced by DBD plasma generation.

The DBD actuator electrode configuration has been shown to dictate the perturbations imposed on a flow. For example, if the grounded electrode is placed downstream of the charged electrode, the generated force accelerates the flow downstream towards the surface therefore delaying boundary layer separation. If the grounded electrode is placed upstream of the charged electrode, the force then acts upstream and can assist in inducing boundary layer separation. When two DBD actuators are placed facing each other, a synthetic jet can be generated away from the surface. DBD actuators can also be used to generate vortices when placed in parallel to increase the mixing of a flow. A common configuration studied, and the configuration used for this work, is the flat-plate surface DBD plasma actuator shown in Figure 1.1. In this configuration, the charged and grounded electrodes are placed parallel to each other and the flow is accelerated downwind from the exposed electrode. Most DBD plasma actuators used in experiments are supplied with alternating current (AC)

waveforms operating in the kHz range. The plasma developed from these waveforms transfers momentum to the flow from the accelerated charged particles colliding with the neutral flow particles, inducing velocity in the flow.

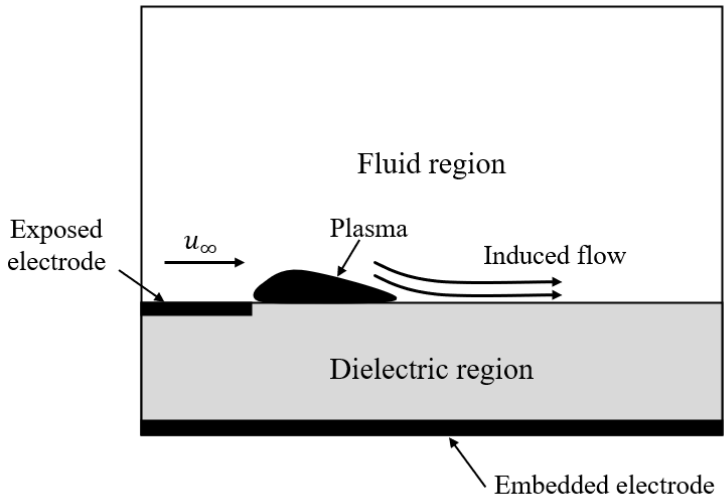

Figure 1.1: Surface DBD plasma actuator configuration

1.2 Current work

The literature reviewed in the following chapter details the promising capabilities of DBD actuators for flow control applications including enhancing aerodynamic performance, aeroacoustic noise reduction, and shock wave manipulation. DBD plasma actuators have been studied extensively both experimentally and numerically to increase understanding of how the electric field interacts with and manipulates external flows. Experimental work has been successful at allowing the structure of the plasma to be studied using light intensity measurements, while numerical work has allowed for analysis of the physical phenomena occurring within the plasma region.

As discussed in the previous section, DBD plasma actuators require an external power source to provide a charge to the exposed electrode. The charge supplied to the

electrode generates the electric field, ionizes the air and produces plasma; therefore, the electrical parameters of the power source directly influence the plasma developed. Supplying DBD actuators with AC waveforms operating in the kHz range has shown to be effective at modifying low-speed flow, while DBD actuators supplied with nanosecond pulses have shown the capability of influencing flows in supersonic conditions. Extensive experimental work has been completed analysing the plasma-flow interaction for high-speed flows, while numerical studies have focused on the compression wave generated from the rapid heating in the plasm region. The characteristics of the plasma produced by AC-DBD actuators have shown to be dependent on the input voltage and frequency, however, limited studies have investigated the dependency of the discharge from an NS-DBD actuator on the input electrical parameters. Additionally, recent studies have demonstrated that the residual surface charge on the dielectric following a pulse significantly effects the subsequent pulse.

Therefore, to investigate the relationship between the plasma characteristics and the input electrical parameters as well as the time dependency of the plasma, this work numerically simulates an NS-DBD actuator supplied with various input voltages and pulse durations. The resulting ion and electron densities, surface charge, and ion sheath propagation are examined to determine if similar behaviour is observed from an NS-DBD actuator compared to a DBD actuator operating in the kHz range. Each simulation completes a total of five pulse cycles to study the evolution of the plasma over time and identify when a quasi-steady plasma configuration has been achieved.

Chapter 2

Literature Review

2.1 Numerical modelling

The physical phenomena that drive the plasma behaviour such as charged particle ionization, recombination, generation, decay, drift and diffusion have been investigated numerically to study the basic physics of DBD actuators. Numerical modelling offers a way to analyse plasma behaviour without requiring costly experimental equipment and is thus a critical component in advancing the understanding of DBD plasma actuators. Some methods currently used to simulate DBD plasma actuators include phenomenological, kinetic, and fluid models.

2.1.1 Phenomenological models

Phenomenological models are used to describe observed relationships of phenomena without explaining the underlying mechanisms as to why the phenomena behave in such a way. These models agree with fundamental theory but are not derived from fundamental theory. When modelling DBD plasma actuators, phenomenological models estimate the force on the flow due to the presence of plasma by adding a body

force term in the momentum equations. This method is computationally inexpensive compared to other models, however, it does not preserve the plasma physics and is not well suited for analysing the underlying mechanisms of the plasma behaviour. In most cases, these models are used to test the implementation of a DBD plasma actuator in a physical problem, not to study the properties of the plasma.

The linear electric field model developed by Shyy et al. [1] is an example of a phenomenological model and is based on an electromagnetic model used in conjunction with the Navier-Stokes equations to investigate the effects of glow discharge on the fluid flow. Here, the paraelectric force is modelled as a body force field in the plasma region and the electric field is modelled to linearly decrease away from the edge of the exposed electrode while the charge density is assumed to remain constant. The linearization of the electric field and assumption of constant charge density significantly simplifies the implementation of the model into numerical simulations. When incorporated into a model of a flat-plat surface DBD plasma actuator, the results showed the presence of plasma induced a wall jet, producing flow velocities in agreement with estimated and experimental values obtained by Roth et al. [2, 3].

The linear electric field model has been used in simulations completed by Cho and Shyy [4, 5] which involved modelling a DBD plasma actuator on an SD7003 airfoil for aerodynamic force control at high angles of attack. The DBD actuator was shown to reduce lift fluctuations by advancing and reducing the separation bubble and modifying the local wall pressure distributions. The work of Abdelraouf et al. [6] also used the linear electric field model to simulate a DBD actuator on a NACA0012 airfoil at high angles of attack. The influence of the DBD plasma actuator was shown to delay the stall angle by 2° and increase the coefficient of lift by 6.1%. The skin friction coefficient was investigated to determine when separation occurred, and it

was found that the DBD actuator allowed for a delay of separation by approximately 50%. Similar results were obtained by Zhang et al. [7], where the presence of a DBD plasma actuator was observed to delay the separation point on an NCCR 1510-7067N airfoil.

Although the linear electric field model has been implemented in many models to study flow control over airfoils, the experimental work completed by Enloe et al. [8] showed a high level of symmetry in the plasma region. The optical measurements obtained from the experiments showed the plasma discharge was ignited at the edge of the exposed electrode and propagated down the dielectric surface at a constant rate. The authors noted differences in the plasma structure in the spanwise direction, however, the chordwise plasma structure was symmetric. The observed symmetric chordwise plasma structure is in disagreement with the model developed by Shyy et al. [1], where the model indicates that the electric field would have enough energy to only ionize the air in the region closest to the edge of the exposed electrode producing an asymmetric plasma region, suggesting that the linear electric field model does not accurately represent the plasma.

Another common phenomenological model used is the one developed by Suzen et al. [9] which incorporates the effects of plasma actuators into the body force in the Navier-Stokes equations. Here, the body force is calculated as a product of the electric field and net charge density. Maxwell's equations are used to solve the electric field generated from the charged electrode while the charge density is prescribed to agree with experimental results and represented as a half Gaussian distribution. This is in contrast to the model developed by Shyy et al. [1] which used a linear distribution for the electric field and constant charge density. The Suzen model requires calibration of the Debye length, which is the maximum distance between two

charged particles not shielded from each others electric field, and the maximum charge density on the dielectric using an experiment consisting of pure plasma-driven flow in a quiescent environment. The requirement of the calibration of both the Debye length and maximum charge density makes implementing the Suzen model into a numerical model more involved than the linear electric field model from Shyy et al. [1].

The Suzen model was implemented in the GHOST two-dimensional code, which is a pressure-based code using the SIMPLE algorithm with second-order accuracy in time and space [9]. The model was applied to simulate a low-pressure turbine flow with large separation to determine the effect of the plasma actuator on the flow separation [9–11]. The results showed the presence of plasma successfully delayed the onset of separation and that manipulation of the maximum charge density value allowed for control over the onset of separation and the extent of the separation zone.

The work completed by Reasor et al. [12] implemented the Suzen model in the UNCLE three-dimensional solver for comparison between 2-D and 3-D results. Both 2-D and 3-D solvers produced similar results, however, when compared to experimental results obtained by Santhanakrishnan [13] discrepancies were observed between the maximum velocity location produced by the 3-D solver. The simulations produced a maximum velocity location 0.4 cm from the edge of the exposed electrode while the experimental results show a maximum occurring 1.6 cm from the edge of the exposed electrode, indicating the model did not accurately capture the plasma influence on the flow.

The work presented by Dennis et al. [11] implemented the Suzen model to simulate flow control over a PAK-B blade via a DBD plasma actuator. The results were compared to experimental data gathered by Huang [14]. Although the numerical simulations displayed the ability to delay flow separation on the turbine blade, there

was a discrepancy between the pressure coefficient profile obtained numerically versus experimentally. This error was indicated to be due to differences in actuator configurations, however, with tuning of the simulations Debye length value better agreement was achieved suggesting that the Suzen model is sensitive to the calibrated values and fine tuning is required to obtain accurate results.

In an attempt to improve on the current phenomenological models used, Orlov [15] developed the lumped element circuit model. This model is based on data collected from time-resolved light intensity measurements of plasma discharge from a single DBD actuator. A time-dependent charge distribution was used to provide boundary conditions to the electric field, in contrast to the half Gaussian model used by Suzen et al. [9]. The behaviour of the plasma actuator was modelled as a network of electric circuit elements, with the circuit consisting of N elementary subcircuits. Each subcircuit represented a small, finite physical domain consisting of the air capacitor, dielectric capacitor, plasma resistive element and diodes to govern the presence of the plasma. The model was validated by experimental results obtained by Enole et al. [16] and Post and Corke [17]. The thrust produced by the plasma actuator in the lumped element circuit model was in agreement with the values obtained by Enloe et al. [16], while the maximum plasma induced velocity was similar to that obtained by Post and Corke [17].

Orlov [15] implemented the model in a numerical simulation on a NACA 0021 airfoil to analyse leading edge separation control using a DBD plasma actuator. The DBD plasma actuator was simulated for steady and unsteady actuation. Both cases displayed the ability of the plasma actuator to significantly delay separation and increase the stall angle of attack. Steady actuation was observed to increase the stall angle by 2°, while unsteady actuation increased the stall angle by 5°. The presence of

plasma decreased the size of the separation bubble, thereby delaying separation and causing the lift of the airfoil to increase and the drag to decrease. The simulation results were consistent with experimental results using the same conditions.

Mertz and Corke [18] compared the lumped element circuit model to the Suzen model to determine which model best captures the physics of the plasma actuator. By analysing the body force each simulation produced and its variation with the maximum applied voltage, Mertz and Corke concluded that the lumped element circuit model produced a better agreement with experimental results. The authors then proceeded to implement the lumped element surface model in a simulation of a circular cylinder in cross-flow. The results showed the DBD actuators were able to eliminate vortex shedding, similar to the experimental results obtained by Thomas et al. [19].

2.1.2 Kinetic models

Kinetic models use the kinetic equations of particles and statistical modelling of particle interactions to solve the flow by considering the interactions of the particles within the plasma. These models focus on the behaviour of individual particles such as ionization, recombination, and attachment. Kinetic models are better suited for understanding the mechanisms of the plasma behaviour compared to phenomenological models as they capture the dynamics of the charged particles within the plasma; however, they are much more computationally expensive.

The work done by Font [20] utilized particle-in-cell (PIC) and Monte-Carlo methods to numerically model a plasma actuator and investigate the plasmas interaction with the fluid flow. The PIC method represent thousands of charged particles of one species (ions or electrons) as a single computational particle whose motion is updated in time under the influence of the electric field. The electric field is calcu-

lated by differentiating the electric potential, which is computed by solving Poisson's equation. The particle positions are used to determine the charge distribution for the solution to Poisson's equation. The Monte-Carlo method was used to evaluate the collisions occurring between the charged particles in the plasma region and the neutral air particles, while the motion of the neutral particles was neglected.

The simulation consisted of pure nitrogen with the exposed electrode supplied with a square wave voltage input of +/-5000 V at a frequency of 8 MHz. The electrode was first charged at -5000 V during the first 60 ns of the simulation, then the charge was reversed to +5000 V from 60 ns and onward. The results from the first half of the simulation showed that the electrons were accelerated along the electric field lines towards the embedded electrode, while the positive ions collided with the neutral particles and trailed behind. This behaviour is commonly observed for the Townsend phase of streamer discharge. After approximately 30 ns, a sufficient amount of electrons had struck the surface of the dielectric and the local vertical electric field had diminished. The loss of the local vertical electric field caused the electrons to begin landing further away from the exposed electrode, however, further ionization was not observed. During this half of the simulation, an average force of 0.2×10^{-6}N directed toward the exposed electrode was inflicted on the neutral particles.

When the charge was reversed to +5000 V, the electrons began accelerating back towards the exposed electrode and the positive ions were pushed towards the dielectric. During this time, the average ion density was observed to be 10 times greater than when the electrode was negatively charged. Additionally, the average force inflicted on the neutral particles while the electrode was positively charged was 7 times greater than what was observed when the electrode was negative (1.4×10^{-6}N compared to 0.2×10^{-6}N) due to the significant increase in the ion density. The results

were compared to the experimental work completed by Enloe et al. [8] and were in good agreement.

Font and Morgan [21] extended the previously discussed work to include oxygen particles in the simulation. The addition of oxygen to the model is significant as negative oxygen ions add momentum in the opposite direction of the positive ions and should reduce the net force imparted on the background flow. Here, the exposed electrode was supplied with a square wave voltage input of +/-5200 V at a frequency of approximately 10 MHz, where the results similar to Font [20] were obtained. However, during the negative going part of this simulation, the plasma was extinguished after approximately 3000 ns. This is significantly longer than the time observed in the pure nitrogen model where the plasma was extinguished after 30 ns.

The presence of oxygen was observed to increase levels of ionization which resulted in a greater net force being imparted on the flow. When the results were compared to experimental work completed by Enloe et al. [22], the slope of the normalized net force versus the applied voltage from the simulation was steeper than the experimental results. However, both the simulation and experimental results correctly predict that the net force produced is higher with the presence of oxygen and as the applied voltage increases. Font and Morgan [21] suggest the difference in force magnitudes may be due to dissociated and meta-stable plasma products accumulating in the vicinity of the plasma actuator over the cycles which would alter ionization levels.

Font et al. [23] compared the numerical results from the PIC model to a fluid model and found that the kinetic model predicted a Townsend type breakdown while the fluid model predicted a glow discharge. However, in both simulations, large regions of non-neutrality were observed where the positive ion concentration was

significantly higher than the electron concentration. The regions of non-neutrality suggest that the plasma density was insufficient to shield itself from the electric field. When the numerical results were compared to experimental results, the presence of an electric field within the plasma confirmed this. The experimental force measurements agreed with the plasma density predicted by the fluid model, while the experimental plasma resistivity was in agreement with the plasma density predicted by the kinetic model. Therefore, the authors suggest that both modes of Townsend breakdown and glow discharge may be present at the same time.

In an attempt to develop a computationally efficient kinetic model of a DBD actuator, Likhanskii [24] used the PIC code VORPAL. The plasma was modelled as a five-species mixture consisting of neutral oxygen and nitrogen particles, positive oxygen and nitrogen ions and electrons. The solver used Poisson's equation to determine the electric potential and Boris push to determine the charged particles motion.

In PIC codes, charged particles are typically represented as macroparticles (particle consisting of several real particles) to reduce computational time. For this work, VORPAL used the concept of nominal density of macroparticles to define the number of real particles in a macroparticle. The nominal density was selected for the two-dimensional case as the macroparticles represent the charged particle per unit length. An issue with the PIC method is the exponential growth of charged particles in the plasma region which significantly impacts the computational efficiency. To resolve this issue, VORPAL uses the concept of variable-weight (VW) particles which defines macroparticles by position, velocity, and weight. Here, the weight defines the number of macroparticles in a particular VW macroparticle. By assigning a weight to a VW macroparticle, standard macroparticles can be combined into one thereby reducing the number of macroparticles in the domain while also restricting the size

of macroparticles to prevent the generation of extremely large macroparticles.

An important element for plasma propagation is the presence of an electron source in front of the plasma front as shown by Boeuf et al. [25]. This electron source is due to photoionization occurring in regions of high electric fields and high electron concentrations. The VORPAL code does not have a photoionization model, therefore a few microparticles were randomly loaded into the simulation at each time step above the DBD surface. The source of electrons was relatively small compared to the generated plasma but was sufficient to support plasma propagation.

The simulations were completed in both two and three dimensions with the exposed electrode being supplied with a 3 kV, 4 ns positive pulse. All essential physical phenomena of the plasma generation and propagation were resolved. The plasma generated from this model was observed to be thicker and propagated higher above the surface compared to plasma generated from a fluid model operating under the same conditions, however; the model provided an accurate solution to the plasma generated by a DBD actuator while remaining computationally feasible.

Likhanskii and Poggie [26] compared the results from the PIC method using VORPAL to multiple fluid models and found both methods produced similar results for the plasma thickness, plasma height above the dielectric surface, electron density, and electric fields. The authors found the main discrepancy between the two models to be the electron density within the streamer, where the fluid model produced a smooth electron distribution while the kinetic model produced a grainy distribution. This result highlights how the kinetic approach resolved the stochastic nature of the plasma discharge producing results similar to experimentally observed plasma filament formation.

2.1.3 Fluid models

Although kinetic models produce very accurate solutions for the plasma discharge region, the computational resources required to run them typically result in researchers employing fluid models instead. Fluid models consist of modelling the ions, electrons, and neutral particles as different species rather than tracking individual particles like kinetic models. These models are useful for understanding the plasma dynamics and the interaction between the charged particles and the electric field. Fluid models are more computationally demanding than phenomenological models, but less so than kinetic models.

Signh et al. [27] developed a fluid model consisting of nitrogen and oxygen to study the discharge produced from an asymmetric DBD actuator in air. The model captured the ionization, dissociation, and dissociative recombination of nitrogen, as well as the ionization, dissociation, dissociative attachment, recombination, and dissociative recombination of oxygen. Metastable species (N_4^+ and O_4^+) were neglected due to their recombination rates, while NO was neglected to reduce the complexity of the model. An atmospheric ratio of 3.6 was taken for nitrogen to oxygen molecules while the drift-diffusion form of the continuity and Poisson's equations were used to solve the charged particle number densities.

The simulation involved supplying the exposed electrode with a sinusoidal voltage with an amplitude of 1000 V at 5 kHz. The authors state that after a few cycles, little change in the particle densities was observed and therefore assumed a steady-state had been reached. The concentration of electrons was observed to increase from $10^3\ cm^{-1}$ at initialization to $10^{11}\ cm^{-1}$ by the time steady-state behaviour was observed. During the sinusoidal cycle, the electrons were observed to be attracted to the exposed electrode during the positive half of the cycle, while being repelled

during the negative half of the cycle. This caused the dielectric surface to behave as a negative electrode after the negative peak voltage due to the electrons depositing along the surface. Previous works by Roy and Gaitonde [28, 29] completed similar simulations in helium where the same behaviour was observed.

The nitrogen and oxygen particles produced through dissociation are neutral and therefore do not respond to the electric field, so the concentration was observed to remain constant throughout the positive and negative halves of the cycles. However, the N_2^+ and O_2^+ particles produced through ionization behaved in a manner opposite to the electrons. They were observed to be repelled from the exposed electrode during the positive half of the cycle and attracted to it during the negative half. Because the ions are significantly heavier than electrons, they remained closer to the dielectric surface. The O^- ions produced through the dissociative attachment of oxygen with electrons behaved similarly to the electrons and moved towards the exposed electrode during the positive half of the cycle and repelled away during the negative half; however, due to their weight little change in the distribution of O^- ions was observed.

Singh and Roy [30] used the work of Singh et al. [27] to develop a relationship between the electrohydrodynamic (EHD) force and electric and physical control parameters. Nine cases were studied where voltage amplitudes of 800, 1000, and 1200 V were applied at frequencies of 2.5, 5, and 10 kHz. The magnitude of the EHD force was observed to increase with the fourth power of the applied voltage amplitude. Thus the induced velocity in the flow was increased as the voltage amplitude increased, meanwhile, a small increase in the induced velocity was observed with increasing frequency. When comparing the results from the approximated EHD force equation to the results from the fluid model, very similar spatial profiles of velocity

were observed suggesting that the EHD force approximation equation could be a way to efficiently model DBD actuators operating within the range of values studied.

Previous work completed by Nishida and Abe [31,32] consisted of a two-dimensional fluid model assuming spanwise uniformity. This model was validated using the experimental work of Enloe et al. [33] and Abe et al. [34] which conducted an optical analysis of the plasma in the chord-wise direction. However, the experimental work completed by Orlov et al. [35] and Enloe et al. [36], which optically analysed the plasma from a top view, showed that the plasma discharge is strongly time-dependent and non-uniform in the spanwise direction. Therefore, Nishida et al. [37] extended the two-dimensional model from [31,32] to be three-dimensional, allowing for analysis of the DBD actuator in the spanwise direction.

The three-dimensional fluid model consisted of three species; electrons, positive ions, and negative ions. The charged particle densities were solved using continuity equations with a drift-diffusion flux coupled with Poisson's equation. The EHD force produced by the plasma was assumed to be equal to the rate of momentum transfer per unit volume due to the collisions between the charged particles and background fluid particles, while the background fluid was assumed to be air with a nitrogen to oxygen ratio of 0.8 to 0.2.

The exposed electrode was supplied with a sinusoidal voltage with an amplitude of 6 kV applied at a frequency of 50 kHz. The model successfully simulated the streamer-type and glow-type discharge observed in experimental studies. The streamer discharge was observed to intermittently form during the positive half of the sinusoidal cycle, where the duration of a streamer was on the order of several tens of nanoseconds and spanned from several tens to several hundreds of micrometers. The glow discharge formed intermittently during the negative half of the cycle at a

frequency higher than the streamer discharge with the duration of several nanoseconds. However, the glow discharge was more diffusive than the streamer discharge, spanning up to one millimeter. The EHD force was also analysed and was found to act downstream during both the positive and negative halves of the cycle. Although a negative-directional EHD force was observed next to the exposed electrode during the negative half of the cycle, the region was small compared to the positive-directional force generated in the rest of the plasma which resulted in the net force remaining positive.

Nishida et al. [38, 39] compared the results of the three-dimensional model to those produced by the two-dimensional model to analyse the effects of the spanwise non-uniformity. The number of current spikes produced in the two-dimensional simulation was much lower than in the three-dimensional model due to the two-dimensional model corresponding to the simulation of a single discharge, while multiple discharges are simulated in the three-dimensional model. The overall characteristics of the EHD force field were the same for both models, however, the two-dimensional model slightly underestimated the plasma length and body force amplitude. The authors conclude that the two-dimensional model is useful for preliminary studies, but the three-dimension simulation is required for the analysis of the plasma structure and actuator performance.

2.2 Effects of voltage waveform on plasma discharge

Extensive research has been conducted both numerically and experimentally examining the dependency of plasma discharge on the supplied voltage waveform. Commonly used voltage profiles include a constant applied voltage pulse, a square pulse, a ramp input, positive and negative sawtooth waveforms, and sinusoidal waveforms.

Boeuf and Pitchford [25] numerically simulated a DBD plasma actuator supplied with a constant input voltage amplitude of 1200 V using a two-species (positive ions and electrons) fluid model. Their results showed that as the exposed electrode was charged, Townsend breakdown occurred between the edge of the exposed electrode and the dielectric surface. Here, the ion space charge was built due to electron avalanching until a quasi-neutral plasma region formed. The plasma region was observed to have a non-neutral tip called the ion sheath. Once the plasma had formed, the ions flowed down the dielectric surface to where the electric potential was lower. As the positive ions impacted the dielectric surface, secondary electrons were generated and released from the dielectric surface. The secondary electrons were then accelerated and multiplied in the ion sheath which allowed the sheath to propagate further down the dielectric surface. This highlighted a direct relationship between plasma propagation and secondary electron emission.

For this work, secondary electron emission was the only mechanism of electron generation ahead of the sheath and produced an ion sheath velocity of 3 $\mu m/ns$ while a maximum EHD force of $1 \cdot 10^9 N/m^3$ was obtained. Although this force is large, each particle in the ion sheath only experienced this force for a very short time due to the fast propagation of the ion sheath. When taking the time-average of the force generated, it was comparable to the estimated force in direct-current surface corona discharge, and therefore the authors concluded that the DBD studied in the paper and corona discharges cause comparable EHD effects.

Building off of the work presented in [25], Boeuf et al. [40] revisited the constant applied voltage case and also considered DBD plasma actuators supplied with time-varying voltage waveforms. The constant input voltage showed that for the ion sheath to propagate along the dielectric surface, a method of electron generation at the ion

sheath edge is required. This case also displayed that as the constant input voltage increased in magnitude, the plasma propagation velocity increased, however, the EHD force did not continue to increase in magnitude for voltage levels above 2 kV. When the voltage level was increased, a larger electric field developed in the vicinity of the plasma actuator. As soon as the electric field reached the background electrons, the electrons were accelerated and collided with neutral particles beginning ionization. This allowed the ion sheath to propagate faster for higher applied voltage levels and caused the particles to experience the EHD force for a shorter time.

To analyse the effects of the voltage rise time on the plasma, a linearly increasing (ramp) voltage waveform with various slopes was applied to the exposed electrode. A voltage slope of 100 V/μs was first used in the simulation. The resulting current developed consisted of several short pulses distributed uniformly in time. This is in contrast to the constant case which produced a square current waveform. In between the large current pulses, a small, non-zero and increasing current was present. At this time a non-neutral ion dense region was observed to form next to the exposed electrode which slowly expanded along the dielectric surface. For times less than 136.84 μs, the discharge was similar to corona discharge as it was self-sustained and dependent on secondary electron emission with a large geometric field distortion at the exposed electrode tip. The large current pulse observed at 136.87 μs caused a breakdown in the plasma formation, leading to a transition equivalent to a corona discharge transitioning to a glow discharge. The dielectric surface was observed to be completely charged after the breakdown, and the plasma region was diffused. Due to the applied voltage on the exposed electrode continuing to increase over time, eventually, the voltage difference between the electrode and the dielectric surface was great enough to generate new plasma.

The EHD force was observed to be much larger during the current pulses than in between pulses. However, due to the pulses being so rapid, when averaged over time the low current phase was found to contribute more to the EHD force. When the voltage slope was varied from 50 V/μs to 200 V/μs, the time between successive current pulses was decreased and the successive plasma breakdown was observed at higher voltages. The time evolution of the EHD force was different for the various slopes due to the corona-like phase being reduced as the slope increased; however, the space integrated time averaged EHD force was similar and not significantly dependent on the slope of the voltage.

A sinusoidal waveform with a voltage amplitude of 5 kV applied at a frequency of 5 kHz was also investigated. During the positive half of the sinusoidal cycle, only one current pulse was noted, while many current pulses of much smaller magnitudes were observed throughout the negative half of the cycle. At 320 μs (during a current pulse) plasma breakdown was observed similar to the ramp case. The EHD force parallel to the dielectric surface was found to be directed away from the exposed electrode during the positive half of the cycle and directed toward the exposed electrode during the negative half of the cycle. The EHD force was larger during the positive half of the cycle and pushed the neutral gas in the same direction, producing similar behaviour observed in corona discharges. As the voltage amplitude was increased and the frequency was decreased, similar features were observed except with the addition of another current pulse during the positive half cycle.

Similar to Boeuf et al. [40], the work of Benard and Moreau [41] compared the influence time-dependent waveforms on the resulting plasma morphology, body force production, and time-averaged electric wind. Sine, square, and positive and negative ramp waveforms were investigated experimentally in quiescent flow conditions. A

voltage amplitude of 20 kV with an AC frequency maintained at 1 kHz was selected for the simulations. The current was measured by the voltage across a non-inductive shunt resistor connected to the grounded electrode, while the plasma formation was recorded by a fast gateable iCCD camera placed above the plasma directed towards the dielectric surface.

Observing the results, positive current peaks were formed during the positive-going part of the cycle for each case due to the generation of ionization channels. The density of the positive current peaks was noticed to be influenced by the slew rate of the input signal. The input signals with high positive slew rates (the square and negative ramp waveforms) had a high density of current peaks and a high density of ionization channels. When the positive slew rate was lower (the sine and positive ramp waveforms) the current peaks and ionization channels were lower in density. However, the ionization channels generated from the sine and positive ramp waveforms were straighter than those generated by the square and negative ramp waveforms which resulted in the current peaks reaching larger magnitudes of approximately 60 mA compared to approximately 40 mA for the square and negative ramp cases.

The slew rate during the negative-going part of the cycle influenced the plasma development as well. When the negative slew rate was small (sine and negative ramp waveforms), the charged particles were concentrated in straight channels that propagated a few millimeters from the exposed electrode. Comparatively, the charged particles were observed to propagate more than 10 mm downstream of the exposed electrode for the cases with larger negative slew rates (square and positive ramp waveforms). The square and positive ramp waveform cases produced only a few current peaks during the negative-going part of the cycle, while the sine and negative ramp cases produced more current peaks but at lower magnitudes.

The time-averaged thrust generated by the EHD force was measured for each case using a force balance. The waveforms were classified into two categories: symmetric (sine and square) and asymmetric (positive and negative ramp). The symmetric waveforms produced a larger average thrust compared to the asymmetric waveforms. The author suspects that a charge build-up effect may reduce the thrust generated by the asymmetric cases. Each case was run at voltage levels ranging from 14 to 20 kV at a constant frequency of 1500 Hz, where the average thrust increased with the applied voltage. Additionally, the frequency was varied from 250 to 1500 Hz with the voltage kept constant at 20 kV, where the higher frequencies generated higher thrust. Lastly, the electrical power consumption was compared to the generated thrust, with the authors recommending a sine wave input as the optimal choice in terms of force generated by electrical power consumption. Although the square wave produced the largest average thrust force, it consumed more electrical power compared to the sine case.

The effectiveness of each waveform was compared by the induced velocity of the background flow. The velocity measurement was taken 5 mm downstream from the exposed electrode and 1 mm above the dielectric surface where the electrode was supplied with a voltage of 18 kV at a frequency of 1000 kHz. The square input generates the largest mean flow velocity, approximately 1.35 m/s, while the sine wave produced a slightly smaller mean velocity of 1.1 m/s. Performance continued to degrade when the ramp inputs where applied. This is in agreement with the results from the thrust measurements, as the square and sine wave produced larger mean thrust values compared to the ramp cases. The amplitude of the fluctuations of the induced velocity was also examined, where the sine waveform produced the largest fluctuations (1 m/s) and the positive ramp case produced the smallest fluctuations

(0.5 m/s). The induced velocity fluctuations are of interest for applications requiring the manipulation of highly turbulent and unsteady flows, where the use of a DBD actuator can increase and decrease the acceleration of the flow and assist with flow separation control. The results suggest that the sine wave would be the optimal choice for flow control applications based on unsteady forcing.

The experimental work completed by Nakanao and Nishida [42] and Nakano et al. [43] agreed with the results observed by Benard and Moreau [41], where the square and sine waveforms induced the strongest thrust in the flow with the sine wave being the most efficient as per electrical power consumption. The authors furthered their investigation and proposed an optimal waveform to maximize the thrust-power ratio where a steep-gradual negative and positive voltage profile was effective for inducing thrust. When the AC cycle was modified to have a waveform with an 80% negative-going cycle, the thrust was increased by 35% and the efficiency increased by 25% compared to the sinusoidal waveform.

2.3 Effects of voltage and frequency on plasma discharge

For continuous actuation of a DBD plasma actuator, the studies discussed have shown a sinusoidal waveform seems to be the optimal choice for actuator efficiency when not considering optimized waveforms. Experimental and numerical work has been conducted to understand how varying the applied voltage and frequency of a sinusoidal waveform effect the plasma. This has led to relationships being derived between input and output parameters, allowing for the optimization of plasma actuators.

Pons et al. [44] conducted experiments to examine the effects of varying the applied voltage amplitude and frequency on the plasma discharge properties. The

voltage was supplied to the exposed electrode using a Trek high-voltage power amplifier that was driven by a function generator producing a sine waveform. The current was measured using a resistive probe and the charge transferred by the circuit was measured using a capacitive probe. The background flow was kept quiescent with zero velocity to allow for focus on the electrical properties such as the power dissipated through the plasma and the velocity induced in the flow.

The time-averaged power dissipated by the plasma discharge was calculated using the area of the charge-voltage curve obtained from a full cycle. By multiplying this value by the frequency the authors obtained the power. The variation of the power was studied over a range of voltage amplitudes (U_{max}) from 10-30 kV at a frequency of 300 Hz and a range of frequencies from 300-1000 Hz at a voltage amplitude of 14 kV. The power was observed to vary with $(U_{max} - U_0)^2$ where $U_0 = 6.5$ kV, and increased almost linearly with frequency. Similar results were obtained by Roth et al. [45], where voltage amplitudes of 2-8 kV at frequencies of 100-2500 Hz were used to analyse the effects of the electrical input parameters on the dielectric heating power. Here, the results concluded that the heating power grew proportionally to the square of the voltage amplitude and linearly with frequency.

To study the influence of voltage on the induced velocity in the flow, the velocity profiles were taken 1.5 cm downstream from the edge of the exposed electrode using a capillary tube connected to a micromanometer. The induced velocity increased linearly within the range of voltages tested. Extrapolating the results showed a threshold value for the flow production of $U_{max} = 6.5$ kV (previously defined as U_0), indicating that below this voltage the induced velocity will not increase proportionally to the voltage. The induced velocity was also proportional to the square root of the time-averaged power dissipated by the plasma, in agreement with the expression

relating power to the voltage amplitude. When the frequency was increased from 300-1000 Hz, the maximum induced velocity increased almost linearly, similar to the time-averaged power dissipated.

The mechanical power supplied to the system was determined using methods outlined in [46], where the mechanical power corresponds to the kinetic energy density flow rate. The results from the velocity profiles showed that the mechanical power was proportional to $(U_{max} - U_0)^3$. By comparing the mechanical power to the time-averaged dissipated power, a relationship between input and output parameters was obtained to determine the efficiency of the plasma actuator as 0.05%. This indicates that the majority of the power was lost to heating, however, the authors suggest selecting a different dielectric or electrode material could reduce the amount of power dissipated and improve the efficiency.

Forte et al. [47] extended the range of frequencies analysed by Pons et al. [44] from 1000 Hz to 2000 Hz to observe the plasma development at higher frequencies. Increasing the frequency increases the slope of the applied voltage, which was found to enhance ionization in the plasma region. Additionally, the mean transferred charge increases with frequency, thereby inducing more collisions in the plasma region. The results showed the maximum induced velocity in the flow increased asymptomatically and began to plateau after 1200 Hz. The effects of varying the applied voltage amplitude were investigated in conjunction with the frequency, where the induced velocity increased linearly with the voltage, in agreement with Pons et al. [44].

More recently, the numerical work completed by Shi et al. [48] tested similar voltage levels (14-22 kV) and frequencies (500-2000 Hz) under quiescent conditions using a two species fluid model consisting of positive and negative ions. The presence of free electrons was neglected as they have been shown experimentally [49, 50] and

numerically [40] to not have a significant influence on the EHD force. The results from the simulations were in agreement with the experimental results from Pons et al. [44] and Forte et al. [47], where the power was found to have a cubic relationship with the voltage amplitude and a linear relationship with frequency, while the induced velocity in the flow increased with both the voltage amplitude and frequency. The authors extended their study to include a background flow with velocities ranging from 1-12 m/s. As the velocity was increased beyond 6 m/s, the effects of the DBD actuator became significantly reduced even as the voltage amplitude and frequency were increased.

Additionally, Shi et al. [48] analysed the effect the voltage amplitude and frequency had on the current density, space charge density, and surface charge density. The current was found to increase almost linearly with both the voltage and frequency, in agreement with the experimental work completed by Valdivia-Barrientos et al. [51]. The current had similar magnitudes during both the positive and negative halves of the sinusoidal cycle, however, the maximum current increased during the first two cycles before reaching a repeatable value for the remaining cycles. This indicated that the electric parameters required at least three voltage cycles to reach a quasi-steady state. The space charge density was observed to increase with the frequency due to the ions having less time to move away from the electrode and diffuse throughout the domain, while the surface charge was found to reverse polarity every half cycle with the voltage.

Experimental work completed by Tang et al. [52] analysed the effect voltage and frequency have on the plasma. By varying the voltage from 12-19.5 kV and the frequency from 500-2000 Hz, the authors used the results to develop empirical relations for the plasma discharge properties within the range of parameters tested.

Here, the plasma length was observed to increase linearly with the voltage in agreement with the results obtained by Orlov [15] and Enloe et al. [22], while the plasma length increased asymptotically with the frequency.

A relationship between the plasma length and height was noted, where the ratio was found to remain constant at approximately 5.2 for the various voltages and frequencies tested. The current density and induced velocity were observed to increase linearly with the voltage, in conformance with the previous studies discussed [44, 47, 48]. However, both the current density and space charge density were found to be independent of the frequency in contrast to the numerical results obtained by Shi et al. [48]. Although the distribution of the space charge density changed with the input parameters, the average charge density did not change significantly. Tang et al. [52] computed a mechanical power efficiency of 0.03%, which is similar to the value obtained by Pons et al. [44].

2.4 Nanosecond pulsed DBD plasma actuators

The previous section focused on studies examining DBD actuators operating with voltage levels of 10-30 kV at frequencies of 500-2000 Hz, where the results showed the plasma induced velocity in the flow via momentum transfer and was successful at delaying separation, increasing the lift force, and decreasing the drag force over airfoils. However, as the background flow velocity increased to tens of m/s, the effectiveness of the DBD actuators significantly declined even when the applied voltage amplitude and frequency were increased. This led to Roupassov et al. [53] performing experimental work, supplying a DBD actuator with a series of high-voltage pulses lasting tens of nanoseconds. The results showed that the actuator was successful at reattaching flows over airfoils at much higher velocities, examining speeds up to Mach

0.85. During these experiments, a near zero velocity was found to be induced in the flow, instead, measurements showed overheating in the plasma discharge region where the rapid, localized heat generation induced compression waves. The results suggest that the main mechanism affecting the background flow is significantly different for a nanosecond (NS) pulsed DBD actuator and one supplied with a sinusoidal voltage operated in the kHz range.

To study the influence of the NS-DBD actuator on the external flow, Roupassov et al. [53,54] performed an experimental analysis of a C-16 airfoil where the actuator was mounted 5 mm downstream from the leading edge. The exposed electrode was supplied with a 25 kV, 12 ns pulse using two different regimes: one consisted of a single pulse being supplied to the electrode with the time between each pulse ranging from 0.1-2 ms, while the other supplied 5-100 pulses in a burst with the time between bursts ranging from 1-100 ms. The external velocity was varied from 10-20 m/s and the pressure distribution data was collected to observe the changes in the lift and drag forces. The single pulse demonstrated the ability to partially reattach the flow at all frequencies tested. When operating under the burst mode regime, two large vortices were generated which increased the pressure peak near the leading edge. Overall, the authors were able to decrease the drag force by approximately 45% and increase the lift force by approximately 30%. Further experiments were performed on a NACA-0015 airfoil at an angle of attack of 18° in flow velocities up to 110 m/s, where the NS-DBD actuator was successful in reattaching the flow. Another study was performed on a Lockheed-Georgia C-141 transonic wing in velocities up to Mach 0.74 where the NS-DBD actuator was successful at reattaching the flow and also significantly reduced the aeroacoustic noise by removing high-frequency pulsations in the wake of the model.

Little et al. [55] performed experimental work on a simplified high-lift model of the NASA Energy Efficient Transport airfoil in flow speeds up to 62 m/s. Due to the small radius of curvature at the leading edge of this airfoil, it is susceptible to stalling at low angles of attack and a deflectable slat is typically included. Although slats are effective at increasing lift, they add weight and increase manufacturing costs and mechanical complexity. Therefore, an NS-DBD actuator was mounted near the leading edge to analyse its capability of flow reattachment which would remove the necessity of a leading edge slat. When supplied with a 100 ns pulse with a peak voltage amplitude of 15 kV, the NS-DBD actuator was successful at delaying the stall angle from 10° to 16°.

The work completed by Little et al. [55,56] compared the resulting current and induced velocity from the NS-DBD actuator to an AC-DBD actuator supplied with a sinusoidal wave form with a peak-to-peak voltage of approximately 15 kV at a frequency of 2 kHz. The maximum current produced by the NS-DBD actuator was approximately 25 times larger than the current produced by the AC-DBD actuator, resulting in power levels up to 600 kW. However, when the power was averaged over time, both cases produced similar values. When comparing the induced velocities in the flow, the NS-DBD actuator transferred significantly less momentum to the flow. Velocities up to 0.5 m/s were observed from the NS-DBD actuator, while velocities up to 3.5 m/s were seen by the AC-DBD actuator, supporting the claim that momentum transfer is not the main mechanism of NS-DBD actuators influencing the flow.

Takashima et al. [57] extended the work from Little et al. [55, 56] to experimentally characterize an NS-DBD actuator by varying the pulse peak voltage, pulse repetition rate (i.e. the time between each pulse), and electrode length. The results showed the pulse energy per unit length was mainly dependent on the peak voltage

and was independent of the electrode length. The plasma region was observed to be uniform during the initial phase of development, however, it became filamentary as time progressed and as the pulse repetition rate was increased. Examination of the compression wave produced by the NS-DBD actuator showed that the wave may be a superposition of individual waves generated by discharge filaments. Additionally, a temperature rise of 350 K in the filament was inferred from UV/visible emission spectroscopy measurements which is similar to the values obtained by Roupassov et al. [53].

The previous studies focused on NS-DBD actuators operating in subsonic flows, however, the work of Nishihara et al. [58] and Adamovich et al. [59] researched flow control capabilities in supersonic flows. Their work consisted of testing a cylinder cross-section with an NS-DBD actuator mounted both symmetrically and asymmetrically to the stagnation line in flow speeds up to Mach 5. When supplied with a high-voltage single-pulse (up to 30 kV) with a duration of 5 ns at a pulse repetition frequency of 100 Hz (i.e. 10 ms between each pulse), the generated compression wave caused the bow shock to be displaced upstream. The experiment was repeated, where a burst of two pulses was supplied to the exposed electrode at a pulse repetition rate of 100 kHz and a burst repetition rate of 200 Hz (i.e 0.01 ms between the two pulses and 5 ms between the sets of pulses). Similar behaviour to the single-pulse case was observed up until the second pulse, where a second compression wave was generated. The single-pulse and first pulse when operating in burst mode increased the shock stand-off distance by 26%, while the second pulse when operating in burst mode increased the stand-off distance by 25%.

The experimental work discussed mainly focused on the ability of NS-DBD actuators as flow control devices, without examining what was occurring within the

plasma region. To expand the quantitative understanding of the mechanisms that occur within the plasma, Unfer and Boeuf [60] developed a two-dimensional fluid model consisting of electrons, positive ions, and negative ions. A 14 kV pulse with a total duration of 35 ns was supplied to the exposed electrode to study the resulting current, ion sheath, electron density, and compression wave. The current peaked as the pulse reached its peak potential, having a maximum amplitude on the order of 10^3 A/m. During this time, an ion sheath developed along the surface of the dielectric and generated a positive surface charge as it propagated away from the exposed electrode. The ion sheath reached speeds up to 500 μm/ns, which is similar to the values obtained experimentally by Starikovskii et al. [61]. As the voltage returned to zero, the current rapidly decayed reaching a negative peak before returning to zero, while the ion sheath returned to the edge of the exposed electrode as its potential became lower than the dielectric surface. During both the rise and fall of the voltage pulse, the electron density was on the order of 10^{18} to 10^{21} m^{-1}. Additionally, the compression wave was observed to propagate like a micro shock wave, travelling at 450 m/s during the first 100 ns before decreasing to 350 m/s.

One of the most significant challenges of modelling NS-DBD actuators is the wide range of time scales required: 10^{-12} s for plasma formation, 10^{-6} s for discharge energy heat generation and compression wave formation, and 10^{-3} s for flow structure. Unfer and Boeuf [60] made their model computationally feasible by employing an asynchronous time integration method coupled with an adaptive mesh refinement technique. The method allows for the mesh to be refined in the plasma region based on Debye length and particle velocities, thereby reducing the number of elements in the mesh and decreasing computational time. Additionally, a simple phenomenological model of energy transfer was implemented in the work instead of modelling the kinetic

processes that govern the energy transfer. In an attempt to develop a computationally feasible model that includes the kinetic processes such as electron impact, excitation, quenching and electron-ion kinetics, Takashima et al. [62] developed a self-similar, local ionization model.

The model used experimental results compared with energy coupling results from a kinetic model to predict discharge parameters such as ionization wave speed, propagation distance, electron density, electric field generation, and plasma thickness. The pulse supplied to the electrode had the same values used by Unfer and Boeuf [60], a 14 kV pulse lasting 35 ns. The ion sheath was found to have a velocity of 570 μm/ns, while the current peak was 11.8 A, where both values are only slightly higher than the values obtained by Unfer and Boeuf [60]. The authors also varied the voltage rise time to analyse the effects on the plasma. Both the ion sheath velocity and current peak increased almost linearly as the voltage rise time was reduced, while the plasma thickness and extent were not significantly affected.

The previous work focused on analysing the behaviour of a single, positive pulse, however, NS-DBD actuators are typically operated in burst mode and sometimes with alternating polarity. The work completed by Deng et al. [63] has shown experimentally that the residual surface charge on the dielectric surface from an initial pulse significantly impacts the propagation of the discharge during the second pulse. The plasma extent increased gradually during each subsequent pulse, while the speed of the plasma front increased 3-8 times during the second pulse compared to the first on an uncharged surface. Additionally, the work from Simeni Simeni et al. [64] demonstrated how the accumulated charge on the dielectric from repeated pulses significantly offsets the electric field before each pulse which effects the overall energy within the plasma. More recently, the experimental work of Peng et al. [65]

found a strong dependency of the plasma and electrical characteristics on the residual surface charge produced by previous pulses.

Due to the residual surface charge affecting the plasma development as pulses are repeated, researchers have used different characteristics of the plasma to determine how many pulses are required to achieve a self-repeating or quasi-steady plasma configuration. Both Shi et al. [48] and Kourtzanidis et al. [66] used the value of the current to determine when the plasma had reached a quasi-steady state, where the current showed self-repeating behaviour from the third cycle and onwards. Bouef et al. [40] also determined the plasma had reached a quasi-steady state by the third cycle, however, their observations were based on the averaged force parallel to the dielectric surface. However, the worked completed by Nakai et al. [67] assumed the plasma had not reached a quasi-steady until the fourth cycle, in agreement with Unfer and Bouef [68] who used the EHD force to determine when the plasma was quasi-steady. Furthermore, Parent et al. [69] indicated a minimum of five cycles are required for the plasma to fully form due to recirculation affecting the temperature distribution near the electrodes.

Chapter 3

Computational Domain

The simulation geometry used for this work consists of a fluid region and a dielectric region as shown in Figure 3.1. The exposed electrode has a length of 0.1 mm and lies flush with the dielectric surface. The embedded electrode spans the entire length of the domain so that the downstream extent of the plasma is not limited by the length of the grounded electrode.

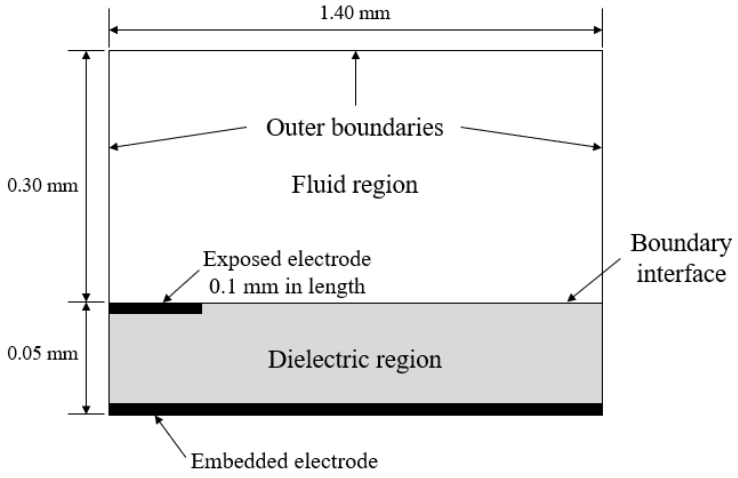

Figure 3.1: Computational domain for simulations

3.1 Governing equations

The fluid dynamics examined for this work are governed by the laws of the conservation of mass (Eq. 3.1) and momentum (Eq. 3.2).

$$\frac{\partial \rho}{\partial t} + \nabla \cdot (\rho \mathbf{V}) = 0 \tag{3.1}$$

$$\frac{\partial (\rho \mathbf{V})}{\partial t} + \nabla \cdot (\rho \mathbf{V} \times \mathbf{V}) = -\nabla p + \nabla \cdot \boldsymbol{\tau} + \mathbf{f}_E \tag{3.2}$$

This work focuses on studying the development of an NS-DBD generated plasma. This requires time scales of such short duration that changes in the background flow are negligible, and therefore the background flow remains quiescent throughout the simulations. This greatly simplifies the above equations, limiting the momentum equation to solving the electrodynamic force $\mathbf{f}_E$ in Eq. 3.2.

3.1.1 Electrodynamic force and electric field calculations

The electrodynamic force $\mathbf{f}_E$ in Eq. 3.2 is included to model the electromagnetic relationships within the plasma region. This term is defined as,

$$\mathbf{f}_E = \rho_c \mathbf{E} + \mathbf{J} \times \mathbf{B} \tag{3.3}$$

where ρ_c is the charge density, $\mathbf{E}$ is the electric field, $\mathbf{J}$ is the current density, and $\mathbf{B}$ is the magnetic field. Maxwell's equations are used to solve for the electric and magnetic fields. The first of Maxwell's equations considered is Ampere's law, given as,

$$\nabla \times \mathbf{B} = \mu_B \mathbf{J} + \frac{1}{c^2}\frac{\partial \mathbf{E}}{\partial t} \tag{3.4}$$

where μ_B is the vacuum permeability ($4\pi 10^{-7}$ H/m) and c is the speed of light in a vacuum ($3 \cdot 10^8$ m/s). Looking at the terms on the right-hand side of Equation 3.4, the induced magnetic field from $\mathbf{J}$ or $\mathbf{E}$ can be neglected for small values of current density and $\frac{\partial \mathbf{E}}{\partial t}/c^2 \approx 0$. For this work the applied magnetic field is 0 which reduces Eq. 3.3,

$$\mathbf{f}_E = \rho_c \mathbf{E} \tag{3.5}$$

The next of Maxwell's equations considered is Faraday's law of induction. This equation is used to relate the time varying magnetic field to the spatial variation in the electric field,

$$\nabla \times \mathbf{E} = -\frac{\partial \mathbf{B}}{\partial t} \tag{3.6}$$

When the magnetic field is neglected, Eq. 3.6 is reduced to,

$$\nabla \times \mathbf{E} = 0 \tag{3.7}$$

Gauss's law for magnetism is,

$$\nabla \cdot \mathbf{B} = 0 \tag{3.8}$$

However, this equation can be neglected due to the absence of an applied magnetic field. Lastly, Gauss's law for electricity is used to relate the charge distribution to the electric field,

$$\nabla \cdot \mathbf{E} = \frac{\rho_c}{\epsilon} \tag{3.9}$$

where ϵ is the permittivity. The dielectric region is modelled as a non-conductive solid and therefore maintains a charge density (ρ_c) of 0. This simplifies Eq. 3.9 to,

$$\nabla \cdot \mathbf{E} = 0 \tag{3.10}$$

for the dielectric region. Due to the presence of free charges, Eq. 3.9 must be used in the fluid region. The permittivity ϵ is calculated as a product of relative permittivity ϵ_r and vacuum permittivity ($\epsilon_0 = 8.85 \cdot 10^{-12}$ F/m) using,

$$\epsilon = \epsilon_r \epsilon_0 \tag{3.11}$$

The electric field $\mathbf{E}$ is expressed as the gradient of the electric potential ϕ_E,

$$\mathbf{E} = -\nabla \phi_E \tag{3.12}$$

Combining Eq. 3.12 with Eq. 3.9 and Eq. 3.10 yields Eq. 3.13 for the plasma region and Eq. 3.14 in the dielectric region.

$$\nabla \cdot (\epsilon \nabla \phi_E) = -\rho_c \tag{3.13}$$

$$\nabla \cdot (\epsilon \nabla \phi_E) = 0 \tag{3.14}$$

The charge density (ρ_c) is used to relate Eq. 3.5 and Eq. 3.13, leading to the next section.

3.1.2 Charge density calculations

The charge density is the difference between the concentration of positive ions and electrons and can be determined by summing the charged particle densities,

$$\rho_c = e_0 \sum_k s_k N_k \tag{3.15}$$

where e_0 is the elementary charge (1.6022×10^{-19} C) and s_k is equal to +1 for positive ions, -1 for electrons. The solution for the particle number density N_k is determined using the continuity equation,

$$\frac{\partial N_k}{\partial t} + \nabla \cdot \mathbf{\Gamma}_k = S_k \tag{3.16}$$

where the source term S_k determines the rate at which particles are generated or extinguished and is dependent on the species and ionization model used. The flux term $\mathbf{\Gamma}_k$ is solved using the drift diffusion model,

$$\mathbf{\Gamma}_k = s_k \mu_k \mathbf{E} N_k - D_k \nabla N_k \tag{3.17}$$

This equation accounts for the movement of charged particles due to both the electric field ($s_k \mu_k \mathbf{E} N_k$) and gradients in concentrations ($D_k \nabla N_k$). The diffusion coefficients are determined from the Einstein relation,

$$D_k = \frac{\mu_k k_B T_k}{e_0} \tag{3.18}$$

where k_B is the Boltzmann constant ($1.3806 \cdot 10^{-23}$ J/K) and T_k is the temperature in Kelvin (assuming 11600 K for electrons, 116 K for positive ions [21]). Substituting these values into Eq. 3.18, the values for the diffusion coefficients for the electrons

and positive ions are $D_e = 1\mu_e$ and $D_+ = 0.01\mu_+$ respectively. These values are consistent with those used by Boeuf and Pitchford [25] and Sato et. al [70].

The value for electron mobility (μ_e) is determined from a drift velocity (V_{d_e}),

$$\mu_e = \frac{V_{d_e}}{E} \tag{3.19}$$

where V_{d_e} is calculated from a curve fit based on data from Grigoriev and Meilikhov [71],

$$V_{d_e} = (E/N)^{0.69813} e^{42.267}(1 + (E/N)^{-0.66345} e^{-33.703}) \tag{3.20}$$

while the positive ion mobility (μ_+) is taken from Kaye and Laby [72] as,

$$\mu_+ = 1.8 \cdot 10^{-4} \cdot 2.69 \cdot 10^{25} \frac{k_B T}{p} \tag{3.21}$$

As previously mentioned, the source term S_k is dependent on the type of charged particle and the ionization model used. All simulations in this work model the fluid as pure Nitrogen gas and only consist of electrons, positive ions, and neutral particles of N_2. Therefore the reactions consist of a single ionization-recombination set,

$$e^- + N_2 \rightleftharpoons 2e^- + N_2^+ \tag{3.22}$$

In the forward direction, this reaction shows for every positive ion generated, an electron is also generated. While in the reverse direction, for every positive ion extinguished, an electron is also extinguished. Therefore the source terms for both electrons and positive ions in pure Nitrogen are equal and can be written as,

$$S_k = S_e = S_+ = \alpha|\mathbf{\Gamma}_e| - \beta N_e N_+ \tag{3.23}$$

where α is the ionization coefficient and β is the recombination coefficient. The ionization coefficient (α) is taken from Raizer [73],

$$\alpha = \begin{cases} 8.8 \cdot 0.750pe^{-\frac{27500}{1.333E/p}} & \text{if } E/p < 150 \cdot 1.333 \\ 12 \cdot 0.750pe^{-\frac{34200}{1.333E/p}} & \text{if } E/p > 150 \cdot 1.333 \end{cases} \tag{3.24}$$

The recombination coefficient β is taken from [25] and set to $10^{-13}\ m^3/s$. With the particle number density, source term and flux term defined, the charged density can now be solved.

3.2 Boundary conditions

This section will discuss the boundary conditions imposed on the computational domain for the electric potential ϕ_E, particle fluxes $\mathbf{\Gamma}_k$, and particle number densities N_k. A summary of the initial conditions is included at the end.

3.2.1 Outer boundaries

As previously mentioned, the fluid region consists of electrons, positive ions, and neutral particles, while the dielectric region is modelled as a non-conductive solid. The outer boundaries are modelled as outlets for these regions with the embedded electrode modelled as the bottom boundary of the dielectric region (displayed in Figure 3.1). For the outer boundaries located in the fluid region, the particle fluxes ($\mathbf{\Gamma}_e$ and $\mathbf{\Gamma}_+$) are solved using Eq. 3.17, while the particle number densities (N_e and N_+) are set to a zero gradient. These conditions are not solved at the outer boundaries located in the dielectric region, including the embedded electrode, as there are no free charges present here. For the outer boundaries in both regions, the electric potential (ϕ_E) is set to a zero gradient, while the value for ϕ_E is set to 0 V for the embedded

electrode for the duration of all simulations.

3.2.2 Fluid-dielectric interface

The equations used to solve the flow must be coupled at the fluid-dielectric interface (the exposed electrode is included in this interface). In the fluid region, the electric potential is calculated using Eq. 3.13, while Eq. 3.14 is used for the dielectric region. Therefore, at the fluid-dielectric interface, the electric field component parallel ($\mathbf{E}_{\parallel}$) to the surface must be equal across the surface such that,

$$(\mathbf{E}_{\parallel})_{fluid} = (\mathbf{E}_{\parallel})_{diel} \tag{3.25}$$

Any difference in the normal component of the electric displacement ($\mathbf{E}_{\perp}$) is equal to the surface charge (σ_c) accumulated on the dielectric (σ_c),

$$(\epsilon\mathbf{E}_{\perp})_{fluid} - (\epsilon\mathbf{E}_{\perp})_{diel} = \sigma_c \tag{3.26}$$

The surface charge (σ_c) is calculated through a time integral of the fluxes of the electrons and positive ions,

$$\sigma_c = \delta_\sigma e_0 \int (\mathbf{\Gamma}_+ - \mathbf{\Gamma}_e) \cdot \mathbf{n} dt \tag{3.27}$$

where the term δ_σ is used to ensure the surface charge is only computed at the fluid-dielectric interface and is set to 1 at the interface and 0 everywhere else including at the exposed electrode.

While the charged particle fluxes are calculated at the boundaries of the fluid and dielectric domain using Eq. 3.17, at the fluid-dielectric interface (including the exposed electrode) the particle flux is dependent on the direction of the electric field.

Positive ions move along the electric field lines while electrons move in the opposite direction, as shown in Figure 3.2. When the electric field is positive and directed away from the surface (Figure 3.2 (a)) the positive ions move away from the surface while electrons embed into the surface, causing the dielectric surface to become negatively charged. When the electric field is negative and directed towards the surface (Figure 3.2 (b)) the positive ions move toward the surface, causing the surface to become positively charged. During this process, an electron can be ejected from the surface, generating free electrons that will assist with ionization in the fluid region.

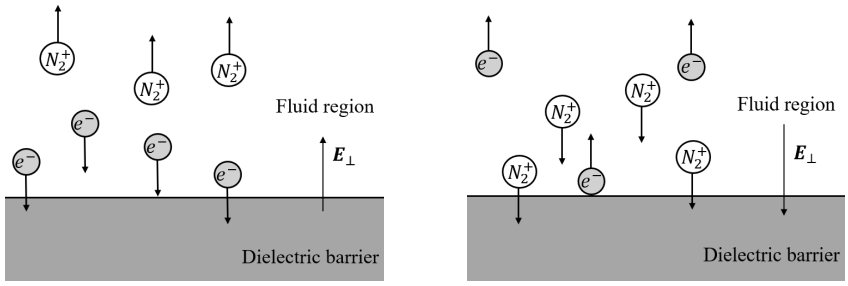

(a) $\mathbf{E}_\perp > 0$ (b) $\mathbf{E}_\perp < 0$

Figure 3.2: Charged particle motion due to electric field

Therefore, the boundary conditions for the particle fluxes along the fluid-dielectric interface are governed by the following set of equations and dependent on the direction of the electric field,

$$\mathbf{\Gamma}_e = \begin{cases} -\mu_e \mathbf{E} N_e & \text{if } E_\perp > 0 \\ -\gamma \mathbf{\Gamma}_+ & \text{if } E_\perp < 0 \end{cases} \tag{3.28}$$

$$\mathbf{\Gamma}_+ = \begin{cases} 0 & \text{if } E_\perp > 0 \\ \mu_+ \mathbf{E} N_+ & \text{if } E_\perp < 0 \end{cases} \tag{3.29}$$

where γ is the secondary emission coefficient (set to 0.05 for all simulations) and

represents the ejection of free electrons when the positive ions move toward the surface. The boundary conditions for the charged particle densities (N_e and N_+) at the fluid-dielectric interface are as follows,

$$N_e = \begin{cases} \nabla(N_e) = 0 & \text{if } E_\perp > 0 \\ \gamma N_+ \frac{\mu_+}{\mu_e} & \text{if } E_\perp < 0 \end{cases} \tag{3.30}$$

$$N_+ = \begin{cases} 0 & \text{if } E_\perp > 0 \\ \nabla(N_+) = 0 & \text{if } E_\perp < 0 \end{cases} \tag{3.31}$$

3.2.3 Exposed electrode

Although the boundary conditions imposed on the exposed electrode are discussed in the previous section, it is worth taking time to discuss the electric potential applied to the electrode throughout the simulations. The goal of this work is to analyse how varying the supplied voltage amplitude and pulse duration effect plasma developed by an NS-DBD actuator. Therefore, a sinusoidal waveform was applied to the exposed electrode and the electric potential on the electrode can be expressed as,

$$\phi_E = A \sin(\frac{2\pi t}{B}) \tag{3.32}$$

where A is the voltage amplitude, t is the time, and B is the pulse duration. Each simulation was run for a total of five cycles for $t = 5B$. A summary of initial and boundary conditions is presented in Table 3.1.

Location	Variable	Condition
Fluid region	ϵ_r	1
	T	300 K
	P	100 kPa
	ϕ_{E_i}	0 V
	N_{e_i}, N_{+_i}	$1 \cdot 10^{13} m^{-3}$
Dielectric region	ϵ_r	10
	ϕ_{E_i}	0 V
Fluid-dielectric interface	ϕ_E	Coupled (Eq. 3.25, 3.26)
	N_e, N_+	Calculated (Eq. 3.30, 3.31)
	$\mathbf{\Gamma}_e, \mathbf{\Gamma}_+$	Calculated (Eq. 3.28, 3.29)
	δ_σ	1
Outer boundaries	ϕ_E, N_e, N_+	Zero gradient
	$\mathbf{\Gamma}_e, \mathbf{\Gamma}_+$	Calculated (E. 3.17)
	δ_σ	0
Exposed electrode	ϕ_E	Calculated (Eq. 3.32)
	N_e, N_+	Calculated (Eq. 3.30, 3.31)
	$\mathbf{\Gamma}_e, \mathbf{\Gamma}_+$	Calculated (Eq. 3.28, 3.29)
	δ_σ	0
Embedded electrode	ϕ_E	0 V
	δ_σ	0

Table 3.1: Initial and boundary conditions

3.3 Numerical methods

The software used for this work is OpenFOAM, an open-source software application that utilizes libraries written in C++ to solve fluid dynamics problems. The solver used for this analysis is based on the conjugate heat transfer with multiple regions solver supplied in OpenFOAM with modification to incorporate plasma development and follows the work of Murzionak [74]. Using first order implicit Euler time marching with time steps on the order of $1 \cdot 10^{-14}$ seconds to capture the behaviour of the charged particles, the convective terms are discretized using second-order Van-Leer discretization, Laplacian terms are discretized using a second-order Gauss linear corrected scheme, and scalar gradients are solved using a linear Gauss integration

scheme.

It is important to note that OpenFOAM uses Gaussian integration to discretize the spatial terms. Gaussian integration is a method to numerically approximate the integral of a function over a finite interval by using points within the interval and corresponding weights to compute the integral accurately. By applying Gaussian integration at the faces between cells and interpolating values (such as pressure or velocity) from cell centres to face centres, the flux integrals of said values can be computed. The Gauss (or Divergence) theorem (Eq. 3.33) can then be used to allow conversion between surface and volume integrals for the spatial terms.

$$\int_V (\nabla \cdot \mathbf{F}) dV = \oint_S \mathbf{F} \cdot d\mathbf{S} \tag{3.33}$$

The theorem states that for a control volume V bounded by surface S, the divergence of $\mathbf{F}$ over the region V is equal to the flux of $\mathbf{F}$ across the boundary S (assuming $\mathbf{S}$ is oriented outward). The theorem is used to relate how much $\mathbf{F}$ is diverging inside the control volume V to how much of $\mathbf{F}$ is passing through the surface boundary S that encloses the control volume V. The theorem provides a link between the local behaviour of the flow (divergence) and the global behaviour of the flow (flux through a closed surface) while also ensuring conservation of fluxes across boundaries.

The discretization and interpolation schemes used for this work are summarized in Table 3.2.

The Gauss Van Leer scheme in OpenFOAM combines the upwind and central differencing schemes and adds a Van Leer limiter $\psi(r)$. The upwind differencing scheme is robust, but only first-order accurate which is generally too inaccurate for use; while the central differencing scheme is second-order accurate, but not well suited to cases with high gradients. Therefore, the Van Leer limiter is added to reduce the

Term	Discretization Scheme	Interpolation Scheme	Order of Accuracy
Time	Euler	-	$O(h)$
Gradient	Gauss	Linear	$O(h^2)$
Divergence	Gauss	Van Leer	$O(h^2)$
Laplacian	Gauss	Linear Corrected	$O(h^2)$

Table 3.2: Numerical methods used to solve the governing equations

errors imposed from each scheme,

$$\psi(r) = \frac{r + |r|}{1 + |r|} \tag{3.34}$$

where r is the ratio of gradients around the integration point and defined as,

$$r = \frac{upwind\ side\ gradient}{downwind\ side\ gradient} \tag{3.35}$$

The limiter will switch the interpolation scheme to upwind differencing at locations of high gradients, while using central differencing everywhere else, keeping the overall scheme second-order accurate in space.

Chapter 4

Grid Sensitivity Study

The mesh used to solve the computational domain is a two-dimensional mesh using two levels of refinement as shown in Figure 4.1. The element size is reduced by a factor of 2 with each successive refinement level, having a maximum element length of 2 μm in the unrefined region and a minimum element length of 0.5 μm within the plasma region. This spacing is selected based on an average particle density of 10^{20} m^{-3} and an electron temperature of 1 eV to produce an element size in the plasma region smaller than the Debye lenth. The refinement regions are increased in length as the voltage amplitude and pulse duration are increased so that the plasma region is always within the maximum refinement region.

A grid refinement study was performed using the methods outlined in [75] to estimate the influence of the grid on the solution accuracy.

4.1 Order of convergence

Before proceeding with the grid sensitivity study, it is important to establish an observed order of convergence. The order of convergence is used to quantify the

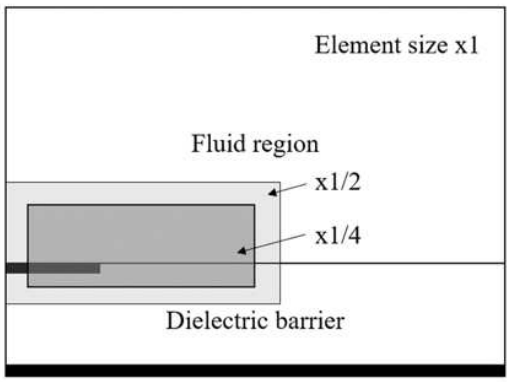

Figure 4.1: Mesh refinement regions

rate at which the simulation approaches the exact solution as the grid spacing is refined. The exact solution is considered to be the value obtained from a grid with zero spacing. The difference between the grid solution (f_h) and exact solution ($f_{h=0}$) can be expressed as,

$$e = f_h - f_{h=0} = Ch^p + H.O.T \tag{4.1}$$

where C is a constant, h is the grid spacing, p is the observed order of convergence and $H.O.T$ is higher-order terms. Assuming the grid is sufficiently refined such that the results do not vary significantly with each grid refinement, the higher order terms can be neglected. By using three grids (f_1, f_2, f_3) with different grid spacings (h_1, h_2, h_3), Eq. 4.1 can be written as,

$$
\begin{aligned}
e_1 &= f_1 - f_{h=0} = Ch_1^p \\
e_2 &= f_2 - f_{h=0} = Ch_2^p \\
e_3 &= f_3 - f_{h=0} = Ch_3^p
\end{aligned}
\tag{4.2}
$$

These expressions can be combined to eliminate $f_{h=0}$ and C,

$$
\frac{e_3 - e_2}{e_2 - e_1} = \frac{f_3 - f_2}{f_2 - f_1} = \frac{h_3^p - h_2^p}{h_2^p - h_1^p} \tag{4.3}
$$

The grid refinement ratios can be defined as,

$$
\begin{aligned}
r_{21} &= \frac{h_2}{h_1} \\
r_{32} &= \frac{h_3}{h_2}
\end{aligned}
\tag{4.4}
$$

Rewriting Eq. 4.3 in terms of the grid refinement ratios gives,

$$
\frac{f_3 - f_2}{f_2 - f_1} = \frac{r_{21}^p (r_{32}^p - 1)}{(r_{21}^p - 1)} \therefore r_{21}^p = \frac{(f_3 - f_2)(r_{21}^p - 1)}{(f_2 - f_1)(r_{32}^p - 1)} \tag{4.5}
$$

The observed order of convergence (p) can then be determined by taking the natural logarithm of Eq. 4.5,

$$
p = \ln \left[\frac{(f_3 - f_2)(r_{21}^p - 1)}{(f_2 - f_1)(r_{32}^p - 1)} \right] / \ln [r_{21}] \tag{4.6}
$$

For this work, the grid was refined by adding successive levels of refinement in the plasma region that reduced the element length by half in both the x and y directions. Therefore, $r_{32} = r_{21} = r$, and Eq. 4.6 can be reduced to,

$$
p = \ln \left[\frac{(f_3 - f_2)}{(f_2 - f_1)} \right] / \ln [r] \tag{4.7}
$$

4.2 Richardson extrapolation

With the order of convergence defined, the Richardson extrapolation is used to estimate the exact solution with zero grid spacing. The Richardson extrapolation is presented in [76], where the discrete solutions f, in the grid spacing h, are assumed to have a series representation,

$$f = f_{h=0} + g_1 h + g_2 h^2 + g_3 h^3 + ... \tag{4.8}$$

where g_i is a function defined in the computational domain that does not depend on any discretization. Richardson [76] proposed if $g_1 = 0$ (a second-order method), then two separate discrete solutions f_1 and f_2, on two different uniform grids with spacings h_1 (fine grid) and h_2 (coarse grid), can be combined to solve for g_2. By substituting this into Eq. 4.8 one obtains,

$$f_{h=0} = \frac{h_2^2 f_1 - h_1^2 f_2}{h_2^2 - h_1^2} + H.O.T \tag{4.9}$$

By dropping the higher order terms and introducing the grid refinement ratio, $r_{21} = h_2/h_1$, Eq. 4.9 can be rewritten as,

$$f_{h=0} \simeq f_1 + \frac{f_1 - f_2}{r_{21}^2 - 1} \tag{4.10}$$

However, Roache [75] highlights several issues with the Richardson extrapolation including the assumption of the absence of odd powers in the expansion of Eq. 4.8 and a monotone truncation error convergence in grid spacing. Other issues identified by Roache [75] include the requirement of integer grid refinement ratios and the magnification of machine round-off errors. Roache's proposed solution is the

Grid Convergence Index (GCI), a method aimed at reporting the results of a grid convergence study in a consistent manner, regardless if Richardson extrapolation is used.

4.3 Grid convergence index (GCI)

Roache's [75] GCI is based on the generalization of the Richardson extrapolation. Including odd powers in the expansion of Eq. 4.8, the Richardson extrapolation can be generalized to *pth*-order methods as,

$$f_{h=0} \simeq f_1 + \frac{f_1 - f_2}{r^p - 1} \tag{4.11a}$$

$$f_{h=0} \simeq f_2 + \frac{(f_1 - f_2)r^p}{r^p - 1} \tag{4.11b}$$

In Eq. 4.11, the second term is an error estimator for either f_1 or f_2. The error estimator for f_1 can be expressed as an estimated fractional error E_1,

$$E_1 = \frac{f_1 - f_{h=0}}{f_1} = \frac{1}{f_1}\frac{f_2 - f_1}{r^p - 1} \tag{4.12}$$

The expression for the fractional error estimator can be reduced to,

$$E_1 = \frac{\varepsilon}{f_1(r^p - 1)} \tag{4.13a}$$

$$E_2 = \frac{\varepsilon r^p}{f_1(r^p - 1)} \tag{4.13b}$$

where ε is the relative error and is defined as,

$$\varepsilon = f_2 - f_1 \tag{4.14}$$

The estimated fractional error (E) is an improvement of the relative error (ε) as it considers both the grid refinement ratio (r) and the observed order of convergence (p). The value of ε can be made artificially small by selecting a grid refinement ratio close to 1, thus the value of E is recommended to quantify the error induced by the grid resolution.

The GCI is the percent difference between the computed numerical value and the true solution. It also indicates an error band on how far the solution is from the asymptotic numerical value as well as how much the solution will change with further grid refinement [77]. The GCI for the fine grid 1 is defined as,

$$GCI_{f_1} = F_s|E_1| \tag{4.15}$$

where F_s is a safety factor. When a coarser grid is required due to computational restraints, the GCI for coarse grid 2 can be calculated as,

$$GCI_{f_2} = F_s|E_2| \tag{4.16}$$

Although the estimated fractional errors E_1 and E_2 are dependent on only the numerical results of grids 1 (f_1) and 2 (f_2), the solution to grid 3 (f_3) is required to determine the order of convergence p. This results in a recommended safety factor of 1.25 in Equations 4.15 and 4.16 when 3 or more grids are compared.

$$GCI_{f_1} = 1.25|E_1| \tag{4.17}$$

$$GCI_{f_2} = 1.25|E_2| \tag{4.18}$$

4.4 Grid sensitivity results

For the purpose of the grid sensitivity study, two additional refinement regions are added as listed in Table 4.1. For each refinement, the number of grid points in the x and y direction is doubled while the number of grid points in the z direction remains constant.

Refinement Level	x - Limits [μm]	y - Limits [μm]	Minimum Element Length [μm]
0	-100 to 1400	-50 to 300	2
1	-100 to 1000	-10 to 100	1
2	-100 to 900	-3 to 75	0.5
3	-100 to 800	-1 to 50	0.25
4	-100 to 600	-1 to 25	0.125

Table 4.1: Refinement region parameters

A total of three grids are used to evaluate the GCI where the coarsest grid uses two refinement regions and the finest grid has four levels of refinement (see Table 4.2). The total number of elements is approximately doubled with each successive refinement region added such that the finest grid has a total of 1.2 million elements and a minimum grid resolution of 0.125 μm. Each case was run on 16 cores of an *Intel*® Core™ i9-13900KF 3.0 GHz CPU.

The results for the grid sensitivity study are evaluated over the first positive half of the sinusoidal voltage cycle. The electrode is supplied with a sinusoidal waveform having a peak potential of 1500 V and a pulse duration of 100 ns. The parameters analysed are the current per unit width along the exposed electrode, the surface

Grid	Normalized Grid Spacing	Refinement Levels	Number of Elements	Computational Time [hr]
Fine	1	0, 1, 2, 3, 4	1 221 789	64
Medium	2	0, 1, 2, 3	744 511	39
Coarse	4	0, 1, 2	360 582	23

Table 4.2: Grid descriptions

charge along the dielectric, and the plasma front position. The global maximum of the variable of interest produced by the finest grid in Figures 4.2, 4.3, and 4.4 is used to determine the time and or location to calculate the GCI.

The current per unit width along the exposed electrode for each grid is displayed in Figure 4.2. The current peaks at 20 ns, where the element size causes a difference of 14.7% between the coarse grid and the fine grid, while the results are indistinguishable between the medium and fine grid. Here, the fine and medium grids produced GCI values of 0.0075% and 0.37% respectively.

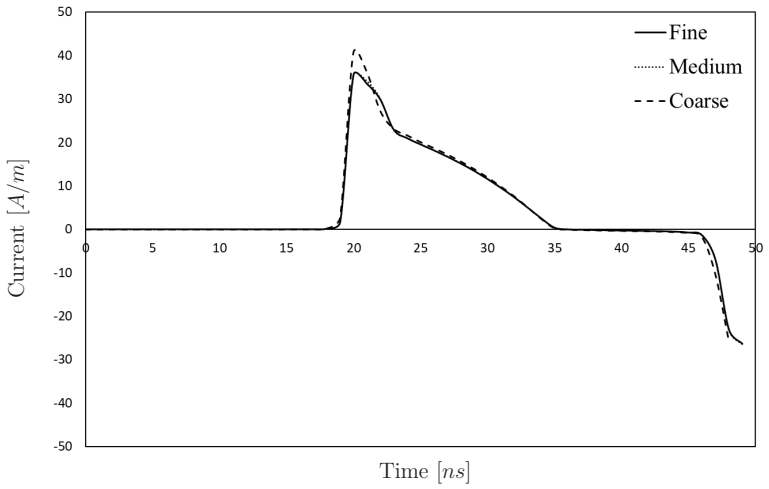

Figure 4.2: Current per unit width along the exposed electrode for different grids

Figure 4.3 displays the surface charge on the dielectric at 50 ns. The surface charge has two positive peaks: one peak at the edge of the exposed electrode and a second peak 129 μm downstream from it. The results from the three grids are

indistinguishable until approximately 100 μm downstream from the electrode. Using the second peak in the surface charge, the coarse grid predicts the peak a distance 6.5 μm downstream compared to the fine and medium grids (which are too close to be distinguished). This results in a difference of 4.7% between the coarse and fine grid. However, all three grids produce the same surface charge maximum of 0.0018 C/m^2. Using the distance of this peak surface charge, the GCI values for the fine and medium grids are 0.005% and 0.46% respectively.

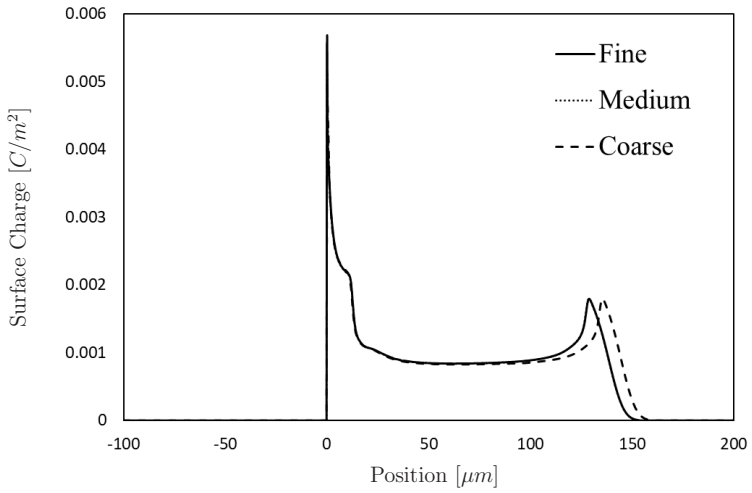

Figure 4.3: Surface charge on the dielectric surface at 50 ns for different grids

Lastly, using the plasma front position as shown in Figure 4.4 there are two regions of discrepancy (A and B). In region A ionization is observed to begin 2 ns earlier for the coarse grid as compared to the fine grid. This results in the plasma region reaching a maximum downstream extent 6.5 μm further for the coarse grid as compared to the medium and fine grids (a difference of 4.7%, similar to the results of the surface charge). Based on the position of the plasma front, the GCIs for the fine and medium grids are 0.009% and 0.23% respectively.

A summary of the GCI results is included in Table 4.3. Small increases in accuracy were noted from the GCIs of the fine and medium grids, where using three

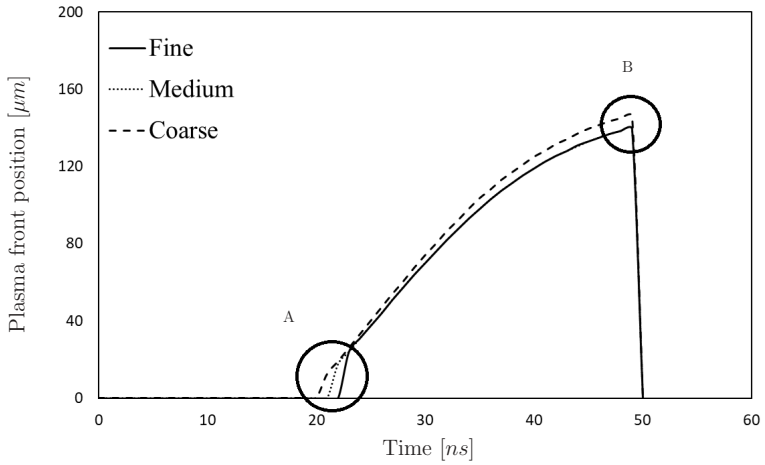

Figure 4.4: Plasma front position for different grids

measures the fine grid has a GCI less than 0.01% compared to the theoretical no grid error solution while the medium grid is within 0.5%.

	Current $[A/m]$	Surface Charge $[C/m^2]$	Plasma Front Position $[\mu m]$
Fine Grid	35.49	0.00179	139.25
Medium Grid	35.59	0.00178	139.5
Coarse Grid	40.70	0.0012	146
p	5.62	6.50	4.70
$f_{h=0}$	35.48	0.0018	139.24
$GCI_{FineGrid}$	0.0075%	0.0054%	0.0090%
$GCI_{MediumGrid}$	0.37%	0.49%	0.23%

Table 4.3: Grid convergence results

In addition to the proceeding analysis, a probe position is chosen to be placed 15 μm downstream from the exposed electrode and 5 μm above the dielectric at 25 ns as shown in Figure 4.5(a). The electric potential (ϕ_E) and charged particle densities (N_e, N_+) at this location (at a time of 25 ns) from the medium and coarse grids are normalized by the results from the fine grid and are shown in Figure 4.5(b). The differences observed between the medium and fine grids is 0.3% for these variables while the coarse grid differs by a maximum of 5% from the fine grid. Although the medium

grid does yield an accuracy to within 0.3% of the fine grid, it also approximately doubles the computational time for a single positive pulse simulation. Given that the maximum difference between the fine grid and the coarse grid is 5% or less, the coarse grid is considered sufficient and thus selected for the remaining simulations. Additionally, the solver has previously been compared to the work of Boeuf and Pitchford [25] and Abdollahzadeh et al. [78] in the work completed by Murzionak [74] using two refinement regions (the coarse grid), with the results in good agreement.

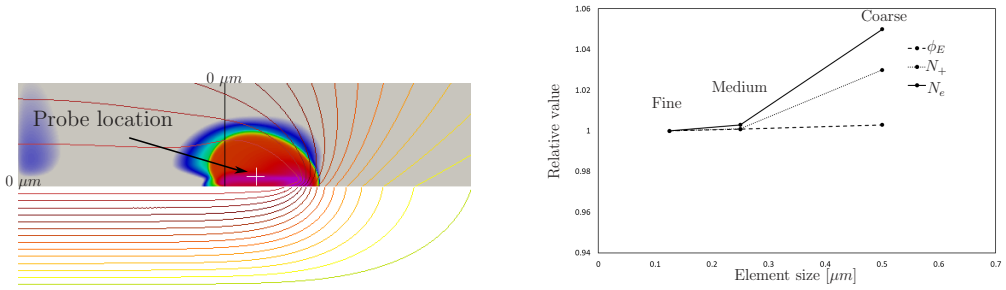

(a) Probe location)

(b) Normalized values

Figure 4.5: Probe location and normalized values for grid sensitivity study

Chapter 5

Results: Effects of applied voltage on plasma development

Several simulations are completed where the peak potential on the exposed electrode is set to 1, 1.2, 1.5 and 2 kV, while keeping the pulse duration constant at 100 ns. This sinusoidal pulse is repeated a total of five times resulting in the applied voltage waveforms shown in Figure 5.1.

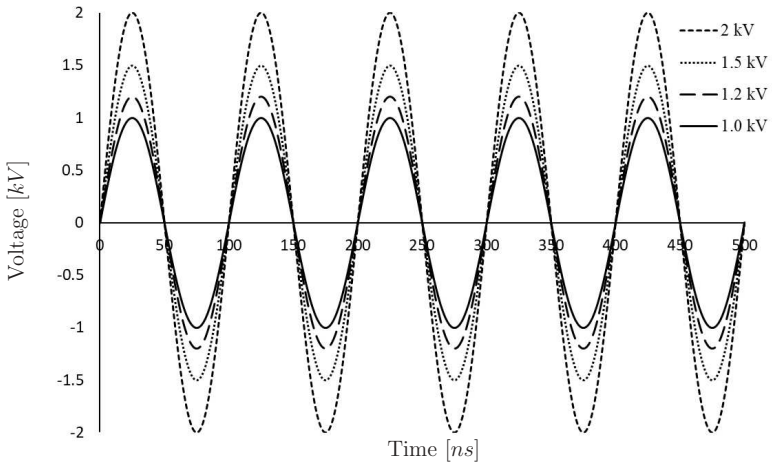

Figure 5.1: Applied voltage profiles

5.1 Plasma Geometry

The plasma region in the fluid domain is identified by the presence of an elevated number of charged particles as shown in Figures 5.2 (a) and (b). The figures show when the electrode is supplied with a sinusoidal waveform having a peak potential of 2 kV with a pulse duration of 100 ns, a plasma region of approximately 100 μm in length and 50 μm in height forms by 25 ns. The remainder of the fluid domain has a charged particle concentration less than 10^{15} m^{-3} and thus can be treated as neutral gas. The contour lines included in the figures show the electric potential throughout the domain.

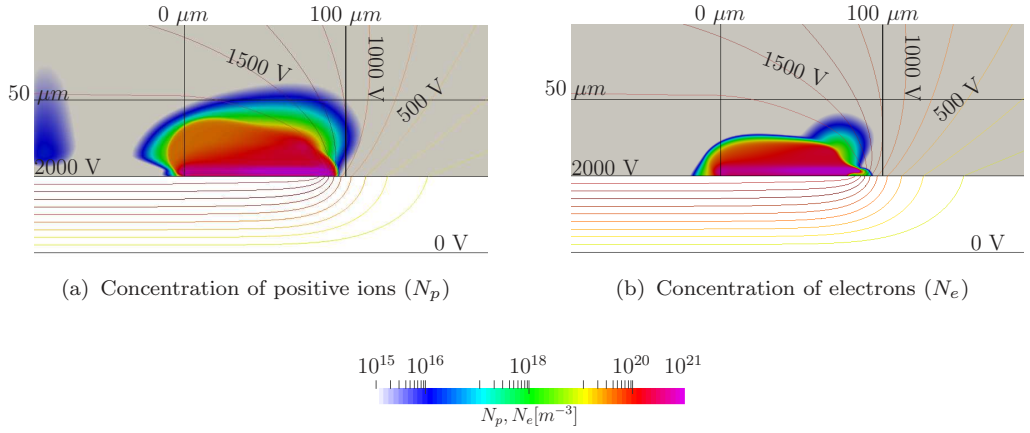

(a) Concentration of positive ions (N_p)

(b) Concentration of electrons (N_e)

Figure 5.2: Charged particle concentrations at 25 ns

The electric field is strongest at the downstream end of the plasma region which causes an unequal distribution in the charged particles in Figures 5.2 (a) and (b). This results in a region within the plasma having an elevated positive charge density as shown in Figure 5.3, and allows the plasma to be separated into two regions: a neutral plasma region and an ion sheath region. The ion sheath is used to define the leading edge of the plasma to evaluate the plasma propagation and can be identified by either the concentration of positive ions, the electric field strength, the charge density, or

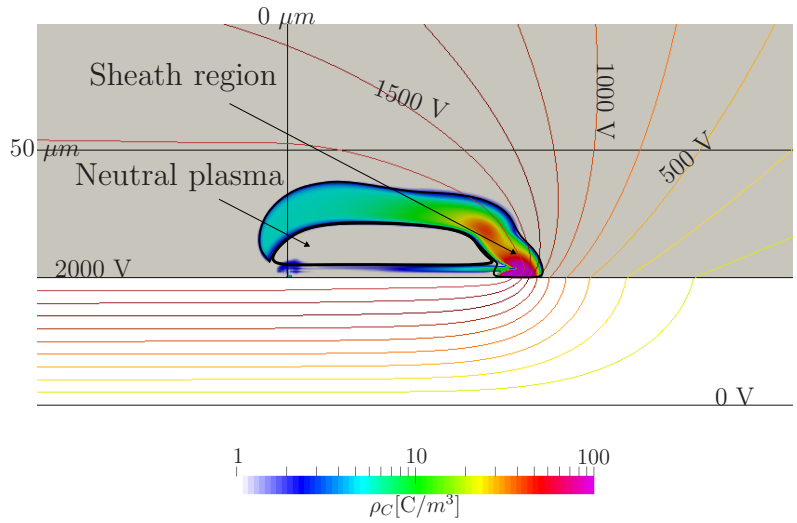

Figure 5.3: Charge density (ρ_c) at 25 ns

the reaction rates occurring within the plasma. For this work, all methods mentioned are used to identify the position of the ion sheath at various points throughout the voltage cycles. The ion sheath also assists with shielding the neutral plasma region from the electric field, preventing the electric potential lines from penetrating through the plasma region as displayed in Figure 5.4. This figure also clearly displays that the maximum strength of the electric field is located within the ion sheath region.

5.2 Applied voltage effect on charged particle distribution and surface charge

This section compares the resulting charged particle distributions and the surface charge generated on the dielectric from the 2 kV case and the 1 kV case when the electrode is supplied with a sinusoidal waveform having a pulse period of 100 ns. For all figures, the top figure displays the 2 kV results and the bottom figure displays the 1 kV results which have been flipped in the vertical direction to mirror the 2 kV case.

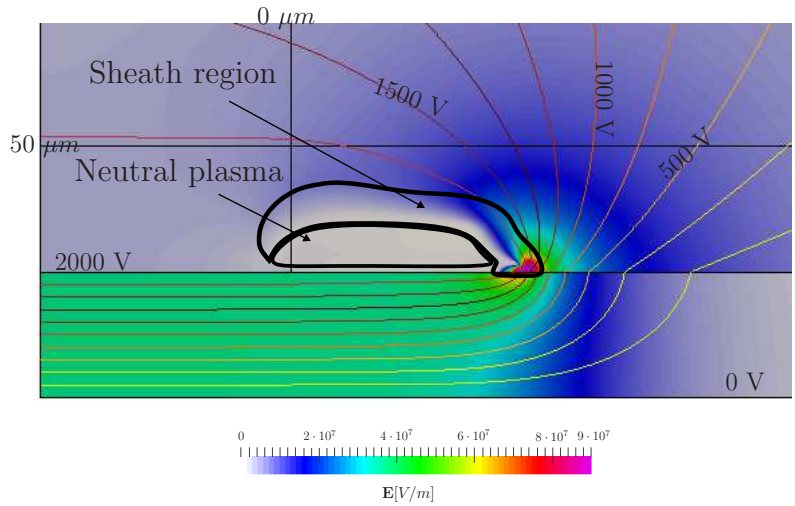

Figure 5.4: Electric field (**E**) at 25 ns

5.2.1 Cycle 1

The distribution of the positive ions at 25 ns when the peak positive potential is first reached is displayed in Figures 5.5 while the resulting surface charge generated on the dielectric is displayed in Figure 5.6. Observing the positive ions, the 2 kV case generates an electric field with enough strength to establish a plasma region spanning approximately 100 μm. This is in contrast to the 1 kV case, where the electric field is too weak to begin ionization. The ion sheath for the 2 kV case is identifiable from the electric potential lines and is directed away from the exposed electrode.

As the voltage on the electrode is increasing, the positive ions propagate downstream from the positively charged electrode causing the dielectric surface to become positively charged as seen in Figure 5.6. The extent of the charge coincides with the extent of the plasma region generated by the 2 kV case, where the magnitude of the surface charge peaks in region A (100 μm downstream from the electrode). This region is where the electric field is strongest and contains the highest concentration of positive ions as observed in Figure 5.5 and indicates the latest location of the positive

ion sheath. Because a plasma region has not formed for the 1 kV case by this time (25 ns), no surface charge is generated along the surface in Figure 5.6.

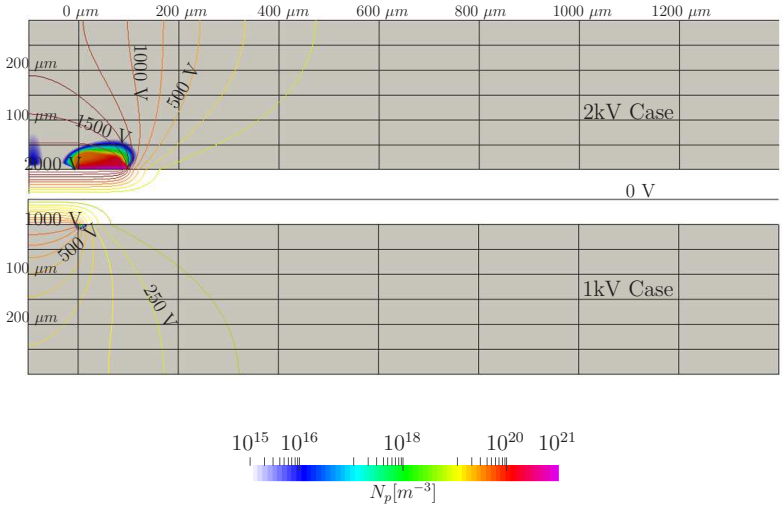

Figure 5.5: Positive ion concentration at 1/4 phase during cycle 1

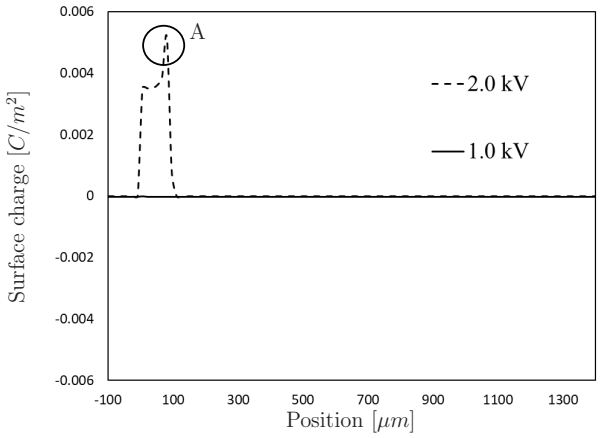

Figure 5.6: Dielectric surface charge at 1/4 phase during cycle 1

As the voltage of the exposed electrode decreases, returning to 0 V by 50 ns, the electric potential on the dielectric surface becomes higher than the exposed electrode as shown in Figure 5.7 where the dielectric surface has a charge of approximately 500 V and 200 V for the 2 kV and 1 kV case respectively. This causes the positive ion sheath that has been established by the 2 kV case to split, where a high concentration of

positive ions reverse in direction and congregate at the edge of the electrode while the rest remain downstream as shown by the charge density in Figure 5.8. Additionally, the size of the plasma region for the 2 kV case has tripled, spanning approximately 300 μm due to the electric field generated by the electrode expanding throughout the domain.

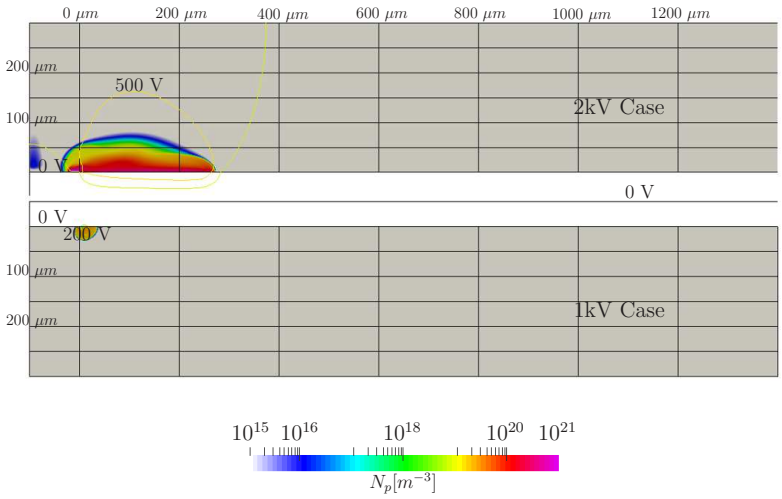

Figure 5.7: Positive ion concentration at 1/2 phase during cycle 1

During the positive half of the voltage cycle, the dielectric remains positively charged as seen in Figure 5.9. The extent of the surface charge is again observed to coincide with the size of the plasma region, where two positive peaks (A and B) are noted for the 2 kV case. The location of peak A coincides with the positive ions that remained at the downstream extent of the plasma region, while peak B coincides with the positive ions that migrated towards the edge of the electrode. Observing the charge density in Figure 5.8 and that the magnitude of peak B is nearly double that of peak A in Figure 5.9, the result suggest that the ion sheath is now located at the edge of the electrode for the 2 kV case.

Due to the onset of ionization for the 1 kV case, a positive surface charge peak (A) is seen in Figure 5.9. This peak for the 1 kV case is similar to the peak observed

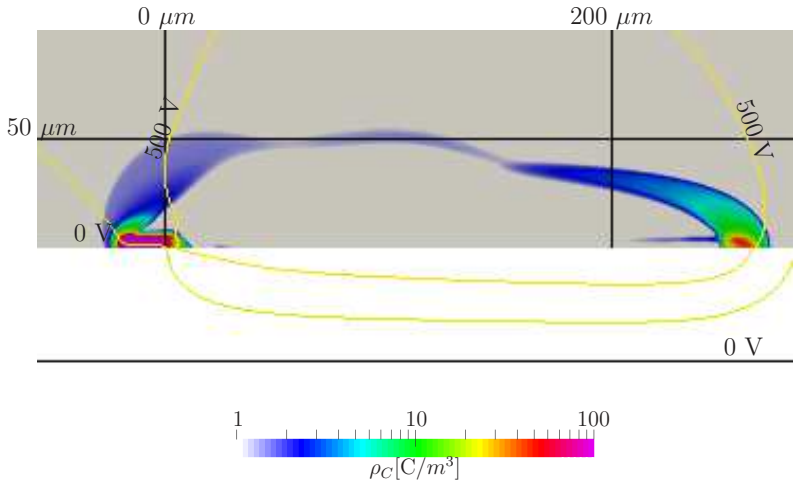

Figure 5.8: Charge density (ρ_c) at 50 ns

at 25 ns for the 2 kV case in Figure 5.6. At 25 ns plasma had not yet formed for the 1 kV case, however, now at 50 ns a small region of plasma (approximately 50 μm in length) has developed for the 1 kV case as seen in Figure 5.7. At this time, the slope of the voltage waveform is constant and decreasing which allows the electric field to gain enough strength to begin ionization, forming an ion sheath as indicated by the positive peak A in the 1 kV case surface charge in Figure 5.9. The positive charge generated on the dielectric from the 1 kV case has a magnitude just under 50% of the magnitude of the charge from the 2 kV case, where the maximum charge is 0.0014 C/m^2 for the 1 kV case compared to 0.0032 C/m^2 from the 2 kV case.

When the charge of the electrode reverses polarity and reaches its negative peak potential, the ion sheath and direction of the plasma becomes difficult to identify due to the plasma region becoming more diffuse. In Figures 5.10(a) and (b), the electric potential lines penetrate through the plasma region, suggesting there is no longer an ion sheath present to shield the plasma. A similar feature was noted in the numerical work completed by Font et al. [23], where the electric field was observed to be penetrating the plasma region and experimental measurements confirmed the

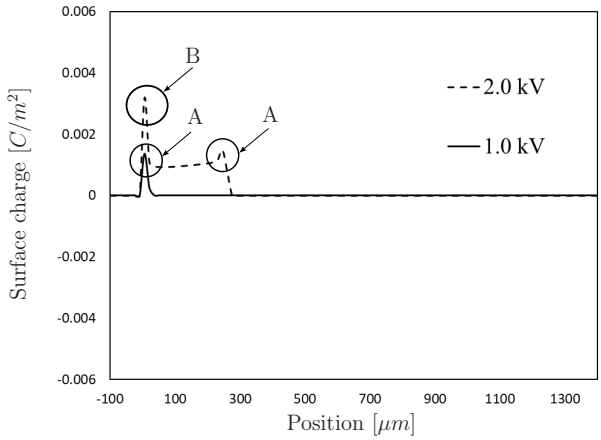

Figure 5.9: Dielectric surface charge at 1/2 phase during cycle 1

presence of an electric field within the plasma. The electric field penetrating the plasma indicates that the plasma density iss insufficient to shield itself from the electric field. Similar behaviour is observed here, where the electric field successfully penetrates through the plasma regions generated by both the 1 kV and 2 kV cases.

In Figure 5.10(a), two distinct ion bubbles are observed for both the 1 kV and 2 kV case. Bubble A has a higher concentration of positive ions located near the negatively charged exposed electrode and is similar in shape to the positive ion distribution observed at 50 ns in Figure 5.7, while bubble B has a lower concentration of ions and is more diffuse. The plasma region generated by the 2 kV case is more than double the length and height of the plasma generated by the 1 kV case (denoted by the concentration of positive ions) as the electric field is significantly stronger and spans further throughout the domain. The negative charge on the exposed electrode repels the electrons downstream and diffuses them throughout the domain as shown in Figure 5.10(b). The diffuse electrons are accelerated by the electric field to a high enough energy to ionize neutral particles and thus generate the positive ion bubble B.

The reaction rates occurring within the plasma at this time (75 ns) are shown

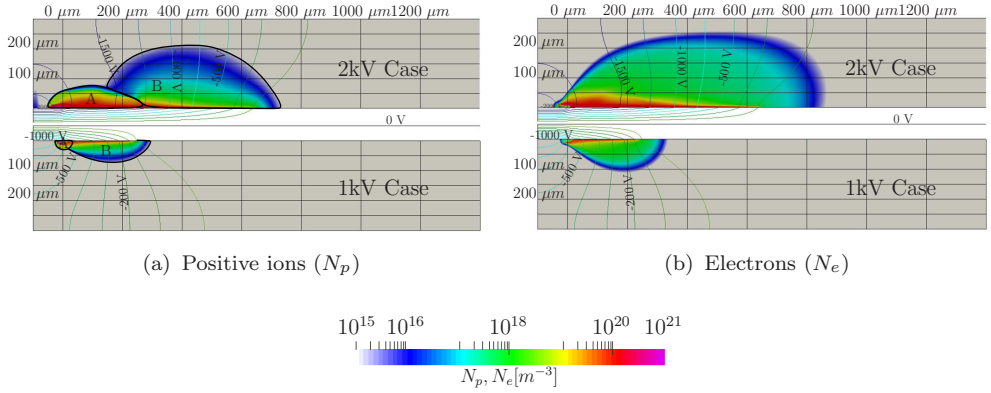

(a) Positive ions (N_p) (b) Electrons (N_e)

Figure 5.10: Charged particle concentrations at 3/4 phase during cycle 1

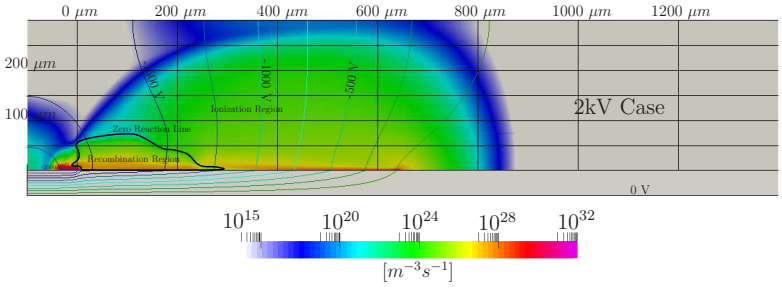

Figure 5.11: Reaction rate for 2 kV case at 3/4 phase during cycle 1

in Figure 5.11. This figure is separated into an ionization region and a recombination region by a zero reaction line. Observing the figure, the ionization rate occurring at the edge of the electrode is four orders of magnitude higher than the recombination rate. This indicates that although the ion sheath is no longer shielding the plasma from the electric field as previously discussed, it is still present and now located next to the edge of the electrode. Comparing Figure 5.11 to the positive ions in Figure 5.10(a), the recombination region is almost entirely located within the ion bubble A while ion bubble B consists entirely of ionization. Therefore, ion bubble A consists of the movement of ions that were previously generated during the positive half of the cycle while ion bubble B consists of newly generated positive ions by the diffuse electrons.

As the electrons propagate along the dielectric away from the negatively charged electrode, a negative charge is generated on the surface as observed in Figure 5.12. This negative surface charge repels the electrons away from the surface, resulting in the increased diffusion of electrons. The charge on the dielectric continues to coincide with the extent of the plasma throughout the negative half of the voltage cycle, spanning approximately 700 μm for the 2 kV case and 250 μm for the 1 kV case. Both cases have surface charges with peak negative values next to the electrode that gradually return to zero downstream from the electrode. The 1 kV case has a positive peak charge before becoming negative which is not observed for the 2 kV case. Looking at the charged particle concentrations in Figures 5.10(a) and (b), while the concentration of both the positive ions and electrons is on the order of 10^{20} for the 2 kV case, the positive ions are an order of magnitude higher than the electrons in the 1 kV case near the edge of the electrode. The increase in positive ions for the 1 kV case could be due to the late formation of the ion sheath. For the 2 kV case, an ion sheath was present prior to the reverse of the slope of the voltage (before 25 ns) which resulted in the positive ions being separated as the ion sheath reversed direction and moved towards the electrode (at 50 ns), leaving a high concentration of positive ions at the downstream extent of the plasma (as shown in Figure 5.8). However, the ion sheath for the 1 kV case was not formed until the slope of the voltage had already begun decreasing (between 25 and 50 ns) which resulted in the ion sheath forming next to the electrode (not splitting like the 2 kV case). The congregation of positive ions causes the positive peak in the surface charge near the electrode observed in Figure 5.12.

As the voltage returns to 0 V, the positive ion bubbles remain similar in shape with only bubble B increasing in length as seen in Figure 5.13(a). The charge on the

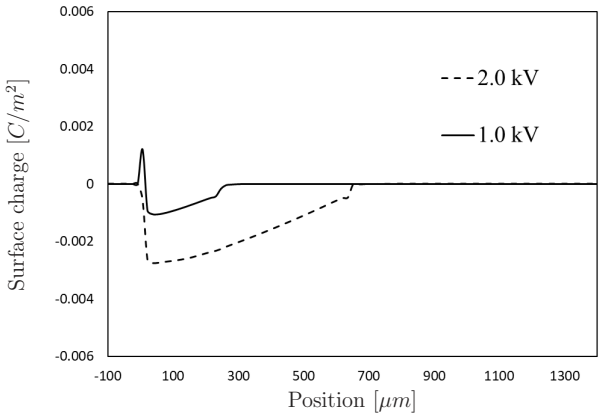

Figure 5.12: Dielectric surface charge at 3/4 phase during cycle 1

dielectric is now lower than the charge on the exposed electrode, where the surface has a charge of approximately -1000 V for the 2 kV case and -500 V for the 1 kV case compared to the charge of 0 V on the electrode. The negative charge encourages the ion bubbles to expand downstream to the area of lower potential similar to the behaviour observed during the 1/4 phase. The charge density at this time is included in Figure 5.14 and shows the ion sheath expanding away from the electrode which also assists with increasing the size of the plasma region (again, similar to the behaviour of the ion sheath observed at the 1/4 phase). The negative surface charge is also responsible for further repelling the electrons making them significantly more diffuse across the entire domain as seen in Figure 5.13(b). Additionally, a high concentration of electrons has moved towards the electrode in an attempt to move away from the peak negative charge on the dielectric surface. Comparing the two voltage cases, the plasma generated by the 2 kV case is nearly triple the length and height of the region observed from the 1 kV case as seen in Figure 5.13(a). The concentration of electrons is also three magnitudes higher for the 2 kV case compared to the 1 kV case, having peak concentrations on the order of 10^{20} m^{-3} and 10^{17} m^{-3} in Figure 5.13(b) respectively.

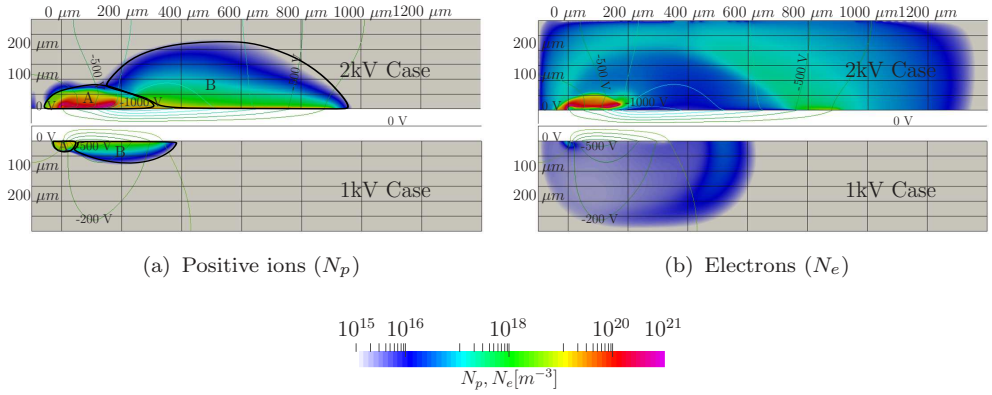

(a) Positive ions (N_p) (b) Electrons (N_e)

Figure 5.13: Charged particle concentrations at the end phase of cycle 1

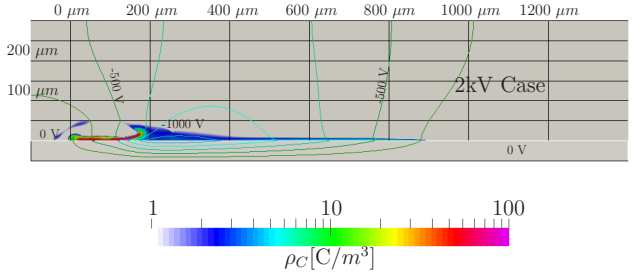

Figure 5.14: Charge density (ρ_c) at 100 ns

The negative charge on the dielectric has been reduced slightly in magnitude in Figure 5.15 compared to the values observed at the 3/4 phase in Figure 5.12 but the extent has increased for both cases. The region of the negative surface charge now extends to 900 μm and 350 μm for the 2 kV and 1 kV case respectively representing a growth of approximately 40% for the 2 kV case and 35% for the 1 kV case. The overall charge on the surface remains largely unchanged for the 1 kV case, however, the 2 kV case now has a slightly less negative hump following the initial negative peak and before returning to a similar peak negative value as seen at the 3/4 phase of the cycle (approximately 0.0025 C/m^2). This hump coincides with the maximum concentration of positive ions in the ion bubble A in Figure 5.13(a) and the ion sheath identified by the charge density in Figure 5.14 which reduces the negative charge on the dielectric in this area.

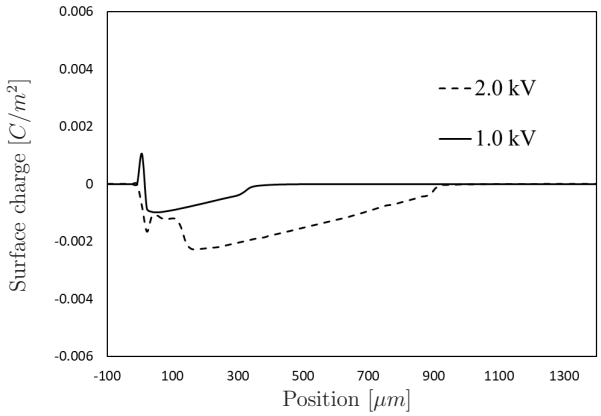

Figure 5.15: Dielectric surface charge at the end phase of cycle 1

At the end of the first voltage cycle (t = 100 ns), the conditions in the domain are significantly different from start-up (t = 0 ns). The concentration of electrons has increased by 7 orders of magnitude for the 2 kV case and 4 orders of magnitude for the 1 kV case compared to the original concentration of 10^{13} m^{-3} for both cases. Additionally, there is now a residual negative surface charge on the dielectric compared to the original uncharged surface. Both these factors facilitate ionization at the beginning of the second cycle.

5.2.2 Cycle 2

The distribution of positive ions and electrons as the potential on the electrode reaches its peak positive value for a second time are displayed in Figures 5.16(a) and (b). An ion sheath is clearly visible for the 1 kV case from the electric potential lines in Figure 5.16(a) and the positive downstream peak in the surface charge in Figure 5.18. Meanwhile, the ion sheath for the 2 kV case is more diffuse at this time and is identified through the charge density displayed in Figure 5.17. In this figure the ion sheath is observed to expand along the dielectric surface, generating a positive surface charge (see Figure 5.18), with the maximum concentration of positive ions

located at the downstream extent of the plasma region. Although the plasma regions do not significantly increase in size, the concentration of positive ions increases by an order of magnitude for both cases. The concentration of electrons has also increased by an order of magnitude for the 2 kV case and by four orders of magnitude for the 1 kV case as shown in Figure 5.16(b). Additionally, the ion bubbles have merged resulting in the formation of one large plasma region that spans approximately 900 μm for the 2 kV case and 300 μm for the 1 kV case as shown in Figure 5.16(a). These values coincide with the extent of the negative residual surface charge observed for both cases in Figure 5.15. This suggests that the residual negative surface charge significantly impacts the plasma development by increasing the levels of ionization.

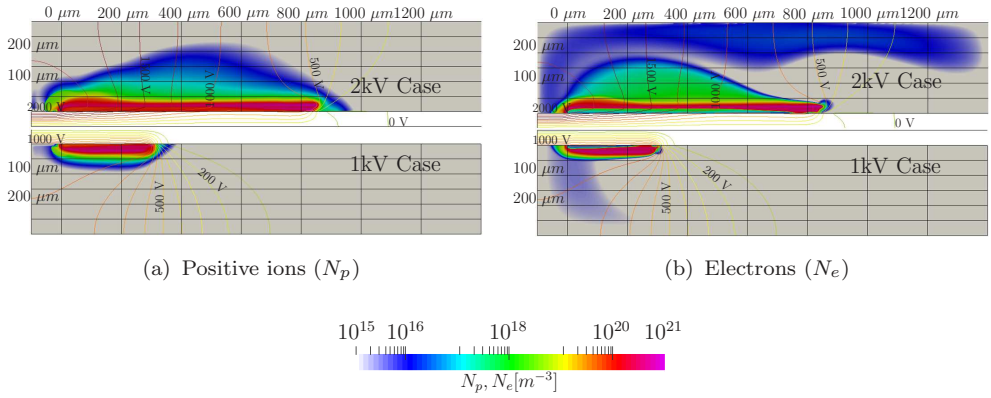

(a) Positive ions (N_p) (b) Electrons (N_e)

Figure 5.16: Charged particle concentrations at 1/4 phase during cycle 2

At the 1/4 phase of cycle 2, a positive charge has now developed on the surface of

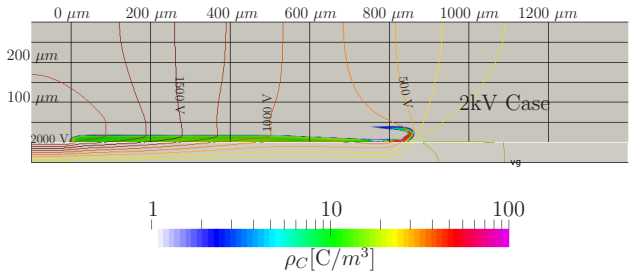

Figure 5.17: Charge density (ρ_c) for 2 kV case at 125 ns

the dielectric as seen in Figure 5.18 similar to that seen at the 1/4 phase during cycle 1 in Figure 5.6. A positive peak in the surface charge is observed for the 1 kV case approximately 300 μm downstream from the electrode, identifying the position of the ion sheath. The surface charge generated from the 2 kV case also has positive peaks; one at the edge of the electrode and another lower in magnitude at the downstream extent of the plasma region. The peaks are not as sharp as previously noted at the 1/4 phase during the first cycle (see Figure 5.6), suggesting that the ion sheath has become more diffuse for the 2 kV case (as observed in Figure 5.17). The surface charge developed from both cases is observed to become slightly negative at the downstream extent of the plasma, where the maximum concentration of electrons is located (see Figure 5.16(b)), before returning to 0.

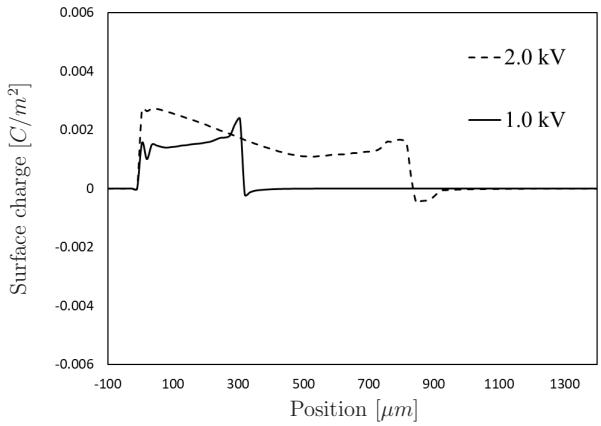

Figure 5.18: Dielectric surface charge at 1/4 phase during cycle 2

As the potential of the electrode decreases, returning to 0 V at the 1/2 phase of the second cycle, the positive ions are observed to split for both cases with high concentrations located at the electrode and the downstream extent of the plasma as seen in Figure 5.19(a). For both cases, the potential on the dielectric surface is higher than the exposed electrode causing the positive ions to move away from the positively charged location on the dielectric surface to areas of lower potential (the electrode and

further downstream on the dielectric surface). The positive charge on the dielectric results in the plasma region expanding, increasing the length by approximately 100 μm for both the 2 kV and 1 kV case. Similar behaviour of the positive ions was observed during the 1/2 phase of the first cycle in Figure 5.7.

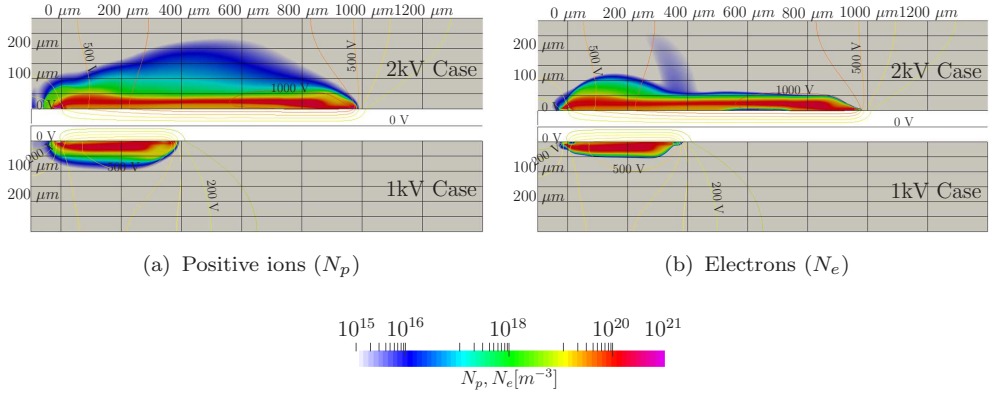

(a) Positive ions (N_p) (b) Electrons (N_e)

Figure 5.19: Charged particle concentrations at 1/2 phase during cycle 2

The surface charge remains positive on the dielectric as the potential on the electrode returns to 0 V with two positive peaks once again observed in Figure 5.20 (as previously seen in Figure 5.9 at the 1/2 phase of the first cycle). The first positive peak for the 2 kV case has decreased by 11% compared to the peak observed at this time during the first cycle, while the magnitude of the second peak at the downstream extent of the plasma region has increased by 50%. The increase in the peak surface charge at the downstream extent of the plasma suggests that a higher concentration of positive ions remain at the downstream extent as the voltage on the electrode decreases during the second cycle in contrast to the first cycle where a majority of the ions moved towards the electrode.

By the 1/2 phase in the first cycle only one positive peak was observed for the 1 kV case in Figure 5.9. However, now two positive peaks are seen for the 1 kV case in Figure 5.20. The surface charge peak next to the electrode has increased by

approximately 40% during the second cycle compared to the peak observed during the first cycle, while the downstream peak is 12% lower than the peak from the first cycle. These values are very similar to the changes observed in the 2 kV case, however, for the 2 kV case the peak next to the electrode decreased in magnitude while the downstream peak increased (opposite to what is observed for the 1 kV case). This could be due to the delay of the formation of the ion sheath during the first cycle, which resulted in a higher concentration of positive ions accumulating next to the electrode.

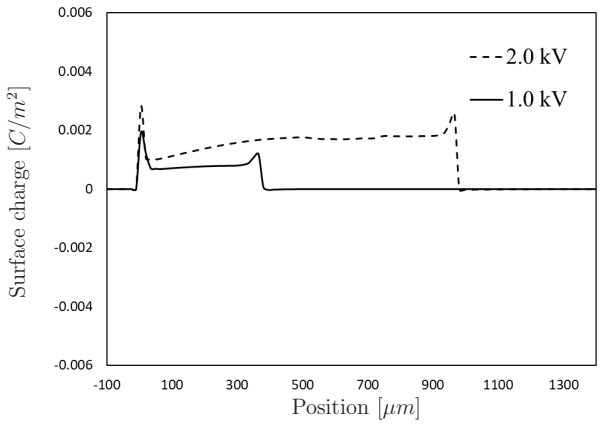

Figure 5.20: Dielectric surface charge at 1/2 phase during cycle 2

During the negative half of the second cycle, the positive ions in the 1 kV case behave similarly to the first cycle and separate into two ion bubbles as shown in Figure 5.21(a). The regions in the 1 kV case are now significantly larger compared to the first cycle with the ion bubble A spanning 400 μm and ion bubble B extending the plasma region to 600 μm. In contrast to the 1 kV case, the two ion bubbles have merged into one large plasma region for the 2 kV case that spans just over 1000 μm. Meanwhile, the electrons have begun diffusing throughout the domain due to the negative charge on the electrode as seen in Figure 5.21(b). The charged particle concentrations are similar in magnitude for both cases, with the 2 kV case generating

a plasma that is approximately 400 μm longer and 125 μm taller than the resulting plasma for the 1 kV case.

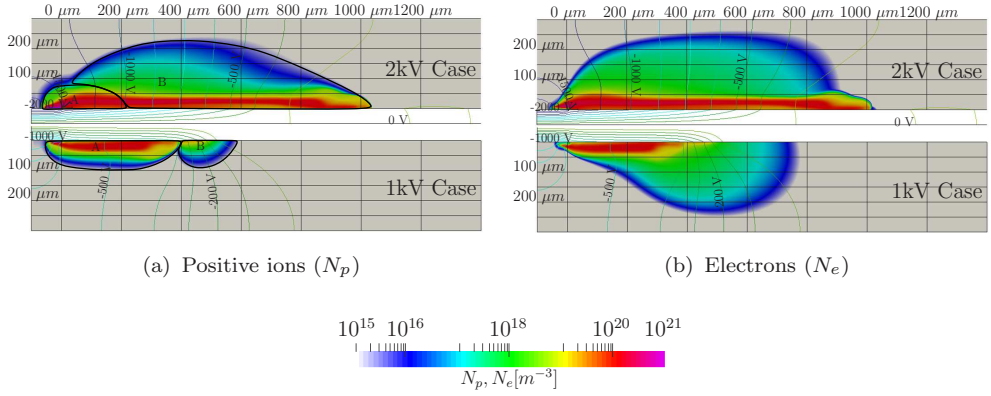

(a) Positive ions (N_p) (b) Electrons (N_e)

Figure 5.21: Charged particle concentrations at 3/4 phase during cycle 2

The surface charge on the dielectric is predominantly negative for both cases as shown in Figure 5.22. Both cases have positive peaks next to the exposed electrode due to an increased concentration of positive ions. The surface charge remains negative for the 1 kV case and gradually returns to 0, however, the 2 kV case has a slight positive charge located at the downstream extent of the plasma. This positive charge spans from approximately 800 to 1050 μm and coincides with the downstream positive surface charge peak observed during the 1/2 phase in Figure 5.20. As previously mentioned, the downstream positive peak observed at the 1/2 phase of the second cycle for the 2 kV case is approximately 40% higher than what was seen during the first cycle (see Figure 5.9). This increase in magnitude results in a stronger ion sheath with higher levels of ionization and thus a larger concentration of positive ions congregates in this region. The increase in the concentration of positive ions and resulting positive surface charge delays the influence of the electrons generating a negative surface charge on the dielectric surface as they move away from the negative electrode, resulting in the residual positive charge observed in Figure 5.20 at the

downstream extent of the plasma.

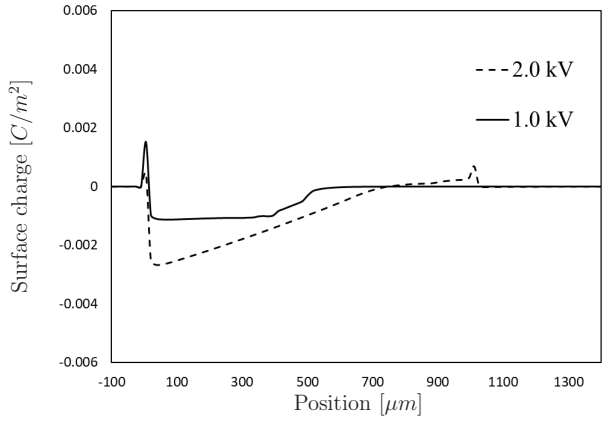

Figure 5.22: Dielectric surface charge at 3/4 phase during cycle 2

As the potential on the electrode returns to 0 V, a third ion bubble (region C) is observed to form at the downstream extent of the 2 kV plasma region in Figure 5.23(a). Region C forms as if the edge of the plasma (approximately 1000μm in Figure 5.21(a)) is the edge of the exposed electrode and increases the plasma length by approximately 250 μm. Figure 5.24 displays the reaction rates occurring at this time for the 2 kV case, where ion bubbles A and B are now located almost entirely within the recombination region while the newly formed ion bubble C is in the ionization region. This is similar to the behaviour observed during the first cycle (see Figures 5.10(a) and 5.11), where ion bubble B formed as if ion bubble A was the electrode and consisted entirely of new positive ions generated from the diffuse electrons.

The ion bubble B for the 1 kV case extends down the dielectric as well, increasing the plasma length by approximately 100 μm. The electrons behave comparably to the first cycle diffusing throughout the domain, however, a significant void of electrons is observed in Figure 5.23(b) from 400 to 650 μm in the 1 kV case. This location coincides with ion bubble B. A slight decrease in the concentration of electrons is seen from 600 to 800 μm in the 2 kV case, however, this region is much smaller than that

observed in the 1 kV case.

The negative electric potential along the surface in these areas attracts the positive ions while also repelling the electrons to areas of higher potential, thus generating electron voids. The lack of electrons in these areas limits the level of ionization. This is why the ion bubble C in the 2 kV case and the ion bubble B in the 1 kV case are smaller than those upstream of them. The electron voids also hinder the development of plasma downstream of these locations for future cycles as the plasma will have to pull electrons from upstream to facilitate ionization at the downstream extent of the plasma region.

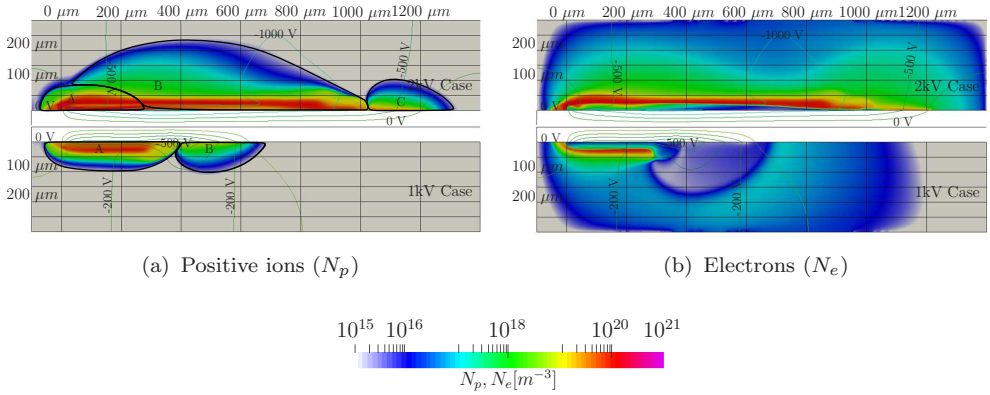

(a) Positive ions (N_p) (b) Electrons (N_e)

Figure 5.23: Charged particle concentrations at the end phase of cycle 2

The surface has become completely negatively charged for both cases by the

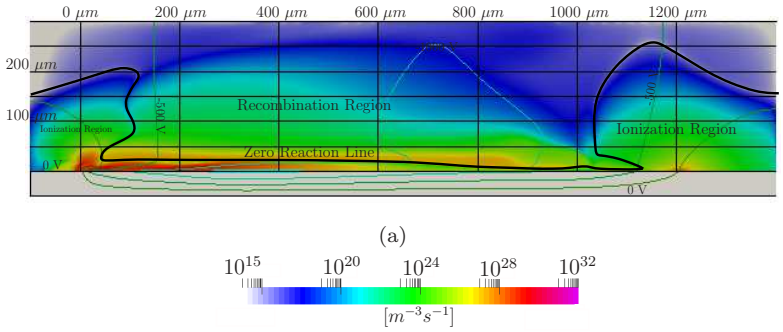

(a)

Figure 5.24: Reaction rate for 2 kV case at the end phase of cycle 2

end of cycle 2 as shown in Figure 5.25. The positive peaks previously observed next to the edge of the electrode are no longer present. Instead, similar behaviour to the cycle 1 end phase results in Figure 5.15 are seen where the dielectric becomes slightly less negative in regions of elevated positive ion concentrations. By the end of the second cycle, the surface charge extent has increased by approximately 300 μm for both the 2 kV and 1 kV case.

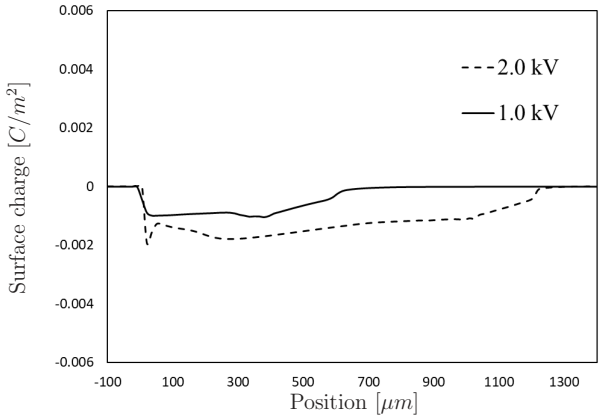

Figure 5.25: Dielectric surface charge at the end phase of cycle 2

5.2.3 Cycles 3-5

As more cycles are completed, the charged particles begin to achieve quasi-steady configurations as shown in Figure 5.26, Figure 5.27, and Figure 5.28 for the positive ions, electrons, and dielectric surface charge respectively.

Beginning from the third cycle and onwards, the electric field is no longer able to transition smoothly from the charged electrode to the grounded electrode for both cases as shown in Figures 5.26(a), (e), and (i). Instead of completely positive parallel potential lines as seen in previous cycles (Figures 5.5(a) and 5.16(a)), a transition to negative electric potential lines is now observed beginning around 350 μm for the 1 kV case and 700 μm for the 2 kV case. Comparing the electric potential lines in

Figures 5.26(a), (e), and (i) to the surface charge in Figures 5.28(a), (e), and (i), the transition in electric potential coincides with a transition of the surface charge from positive to negative. As the charge on the exposed electrode returns to 0 V at 250 ns the concentration of positive ions is reduced by an order of magnitude from 10^{20} to 10^{19} m^{-3} for both cases near the surface of the dielectric in Figures 5.26(b), (f), and (j).

For the negative half of the cycle, the positive ions experience little change in shape and density. The 2 kV case maintains its size, covering approximately 1350 μm of the dielectric, while the 1 kV case spans 600 μm for the third and fourth cycle, increasing to nearly 800 μm during the end phase of the fourth cycle in Figure 5.26(h) and throughout the fifth cycle. At the 1/4 phase of the fourth cycle, the concentration of positive ions increased by an order of magnitude compared to the third cycle (see Figure 5.26(e)). The increase in positive ions results in a stronger ion sheath forming (as identified by the charge density) and allows the plasma region produced by the 1 kV case to expand further downstream.

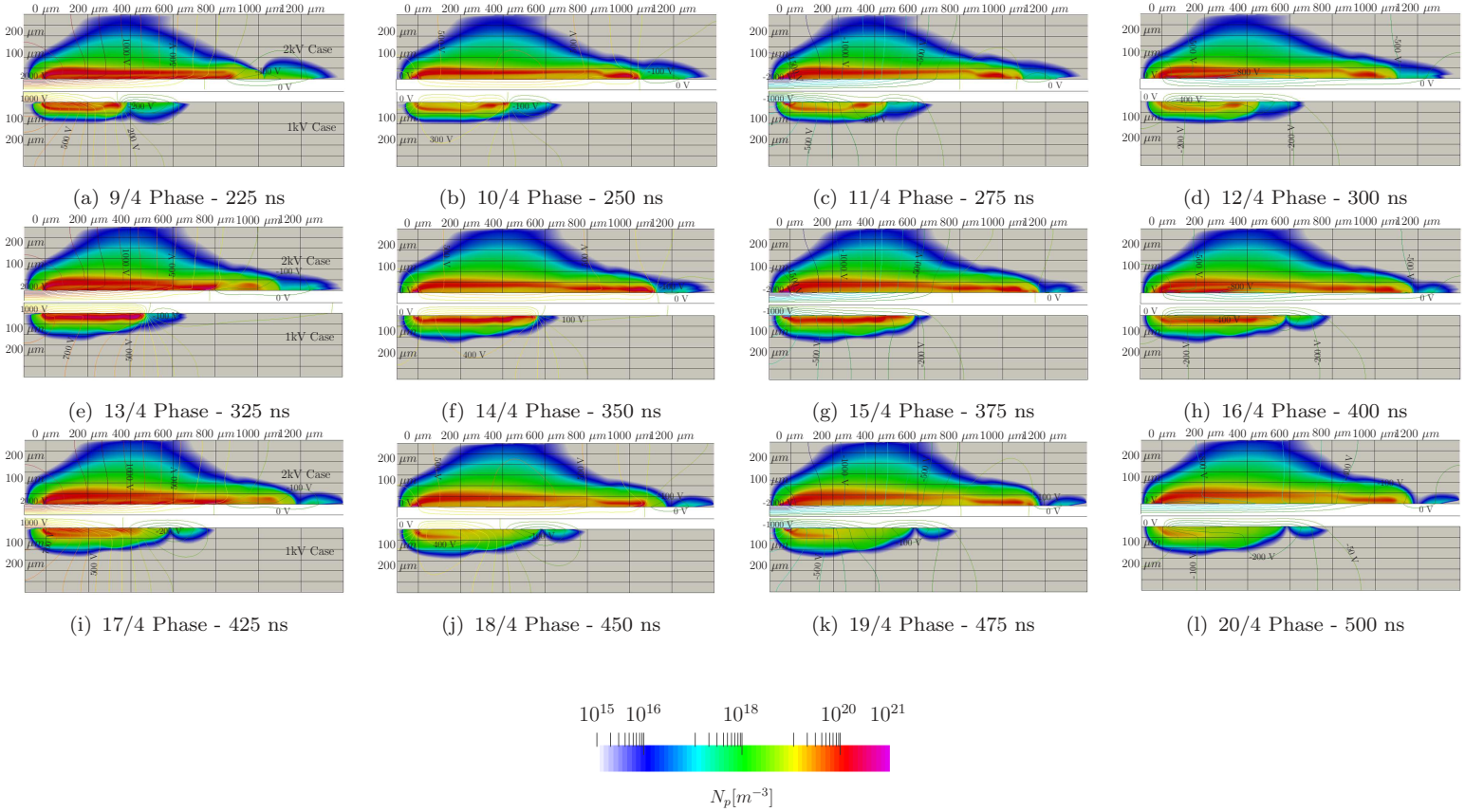

(a) 9/4 Phase - 225 ns (b) 10/4 Phase - 250 ns (c) 11/4 Phase - 275 ns (d) 12/4 Phase - 300 ns

(e) 13/4 Phase - 325 ns (f) 14/4 Phase - 350 ns (g) 15/4 Phase - 375 ns (h) 16/4 Phase - 400 ns

(i) 17/4 Phase - 425 ns (j) 18/4 Phase - 450 ns (k) 19/4 Phase - 475 ns (l) 20/4 Phase - 500 ns

Figure 5.26: Positive ion distributions for the remaining cycles

The residual negative surface charge at the end of the second cycle (Figure 5.25) and the regions void of free electrons (Figure 5.23(b)) continue to further reduce ion sheath development at the 1/4 phase of subsequent cycles such that the surface charge cannot become completely positive again as in Figures 5.6 and 5.18 for the remaining cycles as shown in Figures 5.27(a), (e), and (i). This suggests that the plasma will not be able to extend further down the dielectric and a quasi-steady plasma configuration has been achieved (the distribution of positive ions in Figure 5.26 supports this, as little change is observed in the plasma from the third cycle onwards).

Similar to cycles 1 and 2, during the negative half of the remaining cycles the electrons diffuse throughout the domain. The electron void noted in the 1 kV case in Figure 5.23(b) is clearly visible in Figures 5.27(d), (h), and (l). The void continues to grow in size as more cycles are completed for the 1 kV case, initially spanning from 400-650 μm in Figure 5.27(d) and almost doubling in size by the fifth cycle in Figure 5.27(l) where the concentration of electrons along the dielectric is significantly reduced. The 2 kV case still has a slight decrease in electrons along the dielectric from 600-800 μm, however, it does not grow in size like the 1 kV case. As discussed, the electron void reduces ionization in the plasma region and limits further plasma development indicating that the plasma has achieved a quasi-steady state.

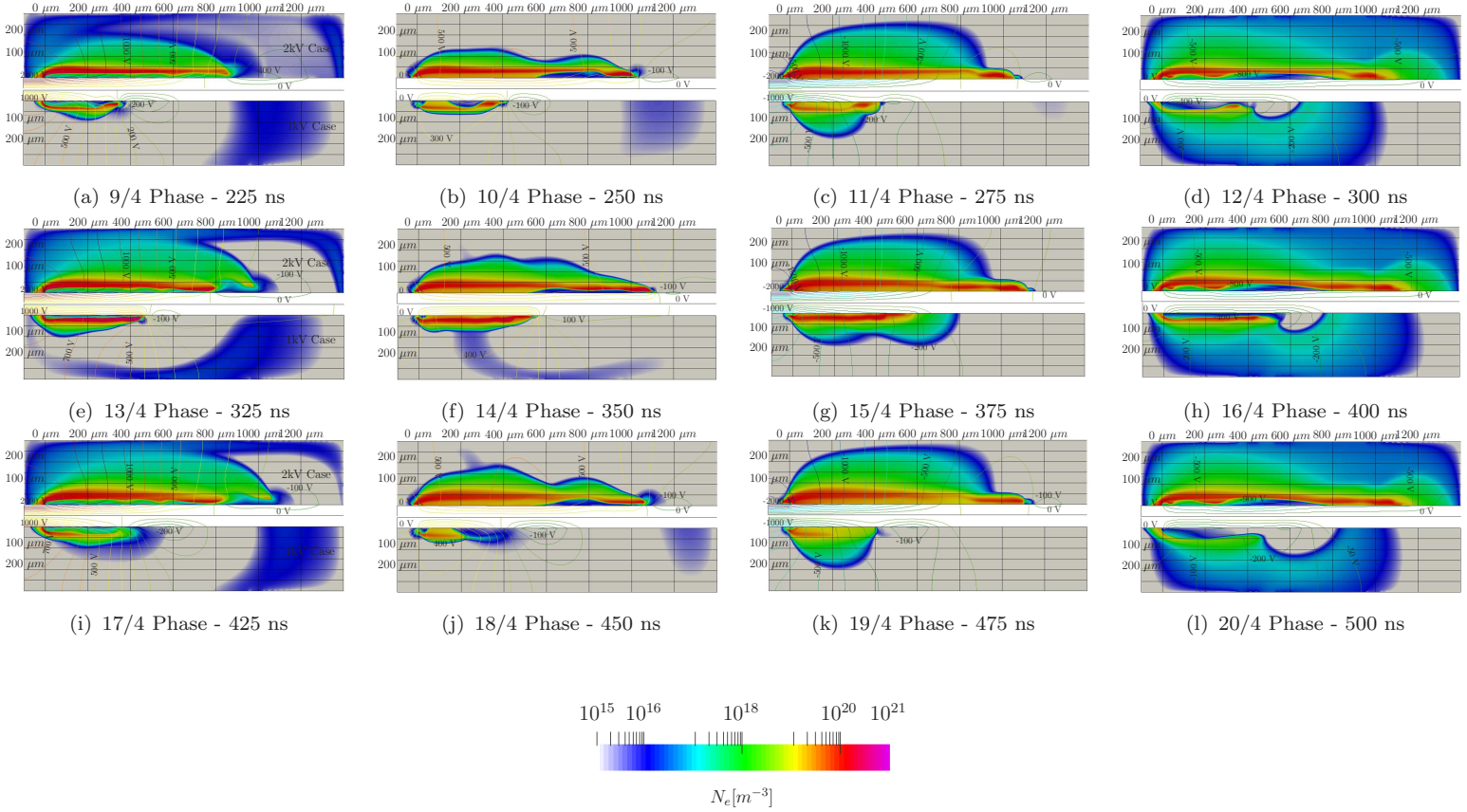

(a) 9/4 Phase - 225 ns (b) 10/4 Phase - 250 ns (c) 11/4 Phase - 275 ns (d) 12/4 Phase - 300 ns

(e) 13/4 Phase - 325 ns (f) 14/4 Phase - 350 ns (g) 15/4 Phase - 375 ns (h) 16/4 Phase - 400 ns

(i) 17/4 Phase - 425 ns (j) 18/4 Phase - 450 ns (k) 19/4 Phase - 475 ns (l) 20/4 Phase - 500 ns

Figure 5.27: Electron distributions for the remaining cycles

As mentioned in the previous discussion on the positive ion distributions, from the third cycle and onwards the surface charge transitions from positive to negative as the electrode reaches its peak potential in Figures 5.28(a), (e), and (i). The change in polarity coincides with the area where the electric field also reverses from positive to negative as noted by the negative potential lines in Figures 5.26(a), (e), and (i). This negative surface charge repels the electrons away from the dielectric and assists with the formation of the electron voids observed at the downstream extent of the plasma in Figures 5.27(a), (e), and (i).

The surface charge displayed in Figures 5.28(b), (f), and (j) show that by the end of the positive half of the voltage cycle the dielectric has a primarily positive charge. However, there is a negative residual surface charge on the dielectric at the downstream extent of the plasma region. As the strength of the ion sheath reduces, the dielectric surface is unable to become completely positively charged as in Figures 5.9 and 5.20.

When the voltage of the electrode reverses polarity the surface becomes negatively charged by the end of the the voltage cycle. This is consistent with the movement of the charged particles in Figures 5.26 and 5.27. Slightly positive and negative peaks are observed in the surface charge diagrams over the cycles, where the peaks coincide with locations of increased concentrations of positive ions or electrons. Nevertheless, the surface charge on the dielectric shows repeating behaviour from the third cycle and onwards.

This section analysed the behaviour of the charged particles and the resulting surface charge generated on the dielectric. The main difference between the 1 and 2 kV cases is the size of the plasma generated. Although the plasma from the 2 kV case extends further downstream on the dielectric surface, both cases produce plasmas

with positive ion and electron concentrations on the order of 10^{20} m^{-3}. Additionally, significant changes were noted during the first two voltage cycles before the charged particle distributions and surface charge on the dielectric display repeating behaviour for both cases. The results indicate care must be taken when analysing plasma parameters during the initial voltage cycles, as the plasma requires multiple cycles before it becomes time-independent. For further analysis of the time dependency of the plasma and the effects of the applied voltage, the following sections will examine the propagation of the ion sheath over the five cycles.

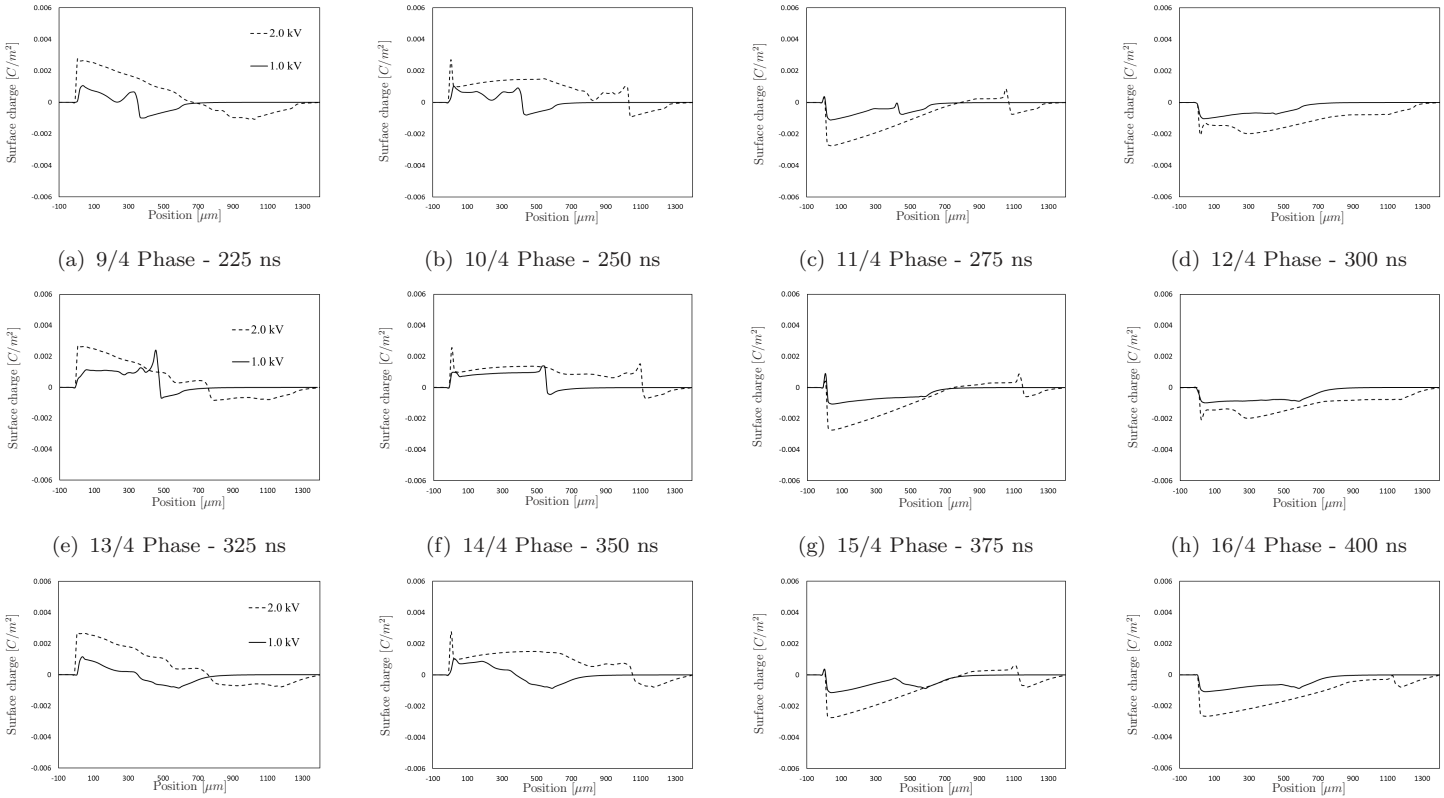

(a) 9/4 Phase - 225 ns (b) 10/4 Phase - 250 ns (c) 11/4 Phase - 275 ns (d) 12/4 Phase - 300 ns

(e) 13/4 Phase - 325 ns (f) 14/4 Phase - 350 ns (g) 15/4 Phase - 375 ns (h) 16/4 Phase - 400 ns

(i) 17/4 Phase - 425 ns (j) 18/4 Phase - 450 ns (k) 19/4 Phase - 475 ns (l) 20/4 Phase - 500 ns

Figure 5.28: Dielectric surface charge for the remaining cycles

5.3 Applied voltage effect on plasma length and ion sheath speed

As previously mentioned, multiple variables can be used to identify the ion sheath such as the positive ion concentration, the electric field strength, the charge density, and the reaction rates occurring within the plasma. For this section, the position of the ion sheath is estimated based on the maximum positive value of the horizontal electric field (E_x) along the surface of the dielectric. Figure 5.29(a) displays the position of the ion sheath along the dielectric surface over time, while Figure 5.29(b) shows the maximum extent reached during each cycle versus the applied voltage amplitude. The previous section examined the charged particle distributions and resulting surface charge where significant changes were noted in the conditions at the start of the second cycle compared to the first cycle. The increase in electrons and residual charge on the dielectric increases ionization at the beginning of the second cycle and encourages rapid propagation of the ion sheath along the dielectric surface. The rapid propagation of the ion sheath can be observed in Figure 5.29(a), where the plasma extent increases by approximately 280% for the 2 kV case, 380% for the 1.5 kV case, 575% for the 1.2 kV case ,and 1530% for the 1 kV case as compared to the first cycle. The lower voltages (1 kV and 1.2 kV) experience higher percent increases as the electric field is insufficient to generate a region of plasma during the positive half of the first cycle. The plasma is observed to gradually expand downstream during each cycle in Figure 5.29(a). Similar behaviour was observed by Deng et al. [63] when AC voltages ranging from 15-18 kV were applied at a frequency of 50 kHz.

The previous results indicated a minimum of three voltage cycles are required before the plasma reaches a quasi-steady configuration. Therefore, Figure 5.29(b) compares the maximum extent the ion sheath to the voltage supplied to the electrode

over cycles 3 through 5. The average of each voltage level over these cycles is indicated by an "X" marker, with a trend line plotted which generates an expression to predict the plasma length for voltage levels within the range tested here. This function can be implemented in a simple phenomenological model to predict the size of the area the plasma region will cover.

As the applied voltage increases, the maximum plasma length increases almost linearly. Similar behaviour has been observed for AC-DBD actuators, where the plasma extent increases linearly with the applied voltage [15,22,52]. All cases reach a maximum extent during the fourth cycle. The analysis of the electron distribution in the previous section shows a growing electron void at the end phase as more voltage cycles are completed. The void forces ionizing electrons to be pulled from upstream and limits further propagation of the plasma region. However, only a very small electron void is noted in the 2 kV case throughout the cycles which is why the 2 kV case is able to reach a maximum extent of approximately 1100 μm during both the fourth and fifth cycles.

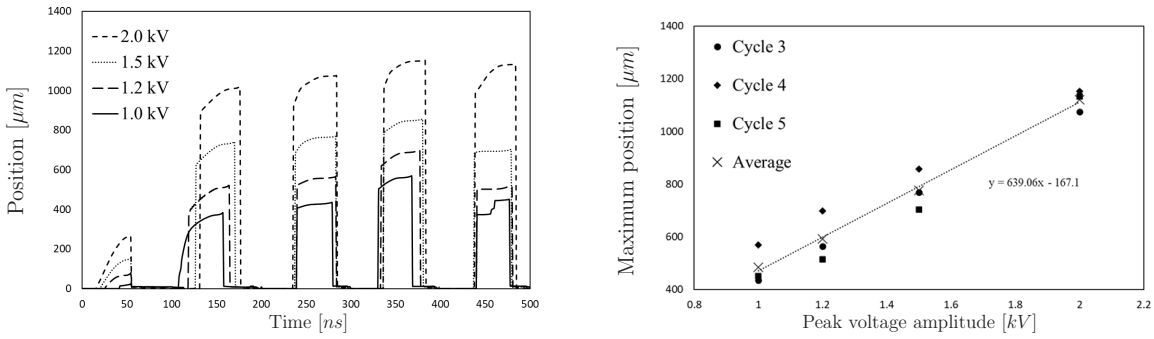

(a) Position of the ion sheath

(b) Maximum position of ion sheath for cycles 3-5

Figure 5.29: Ion sheath position for multiple applied voltage amplitudes

The instantaneous speed of the ion sheath as found by differentiating the ion sheath position over the five cycles is displayed in Figure 5.30(a), while the maximum

positive speed reached during cycles 3 through 5, and their averages, versus the applied voltage is displayed in Figure 5.30(b). The various voltages supplied to the electrode produce ion sheath speeds between 180 and 570 μm/ns, where a positive speed indicates the ion sheath is propagating away from the electrode and a negative speed indicates the ion sheath is moving towards the exposed electrode. Similar magnitudes have been observed in the literature where the numerical simulations of NS-DBD actuators by Takashima et al. [62] and Unfer and Boeuf [60] produced ion sheath speeds of 500-570 μm/ns. As the voltage increases, the ion sheath speed increases approximately linearly as seen by the trend line included in Figure 5.30(b), similar to the results obtained by Takashima et al. [62]. The ion sheath speed increases as the voltage levels increase due to a larger plasma region forming on the surface of the dielectric, thus causing the ion sheath to have to propagate a further distance to reach the downstream extent of the plasma. Due to the plasma region gradually expanding during each cycle, the ion sheath travels a further distance when returning to the edge of the exposed electrode. This results in higher ion sheath speeds in the negative direction. During the fifth cycle, the plasma extent is reduced for all cases except the 2 kV case, therefore a reduction in the ion sheath speed occurs as shown in Figure 5.30(b).

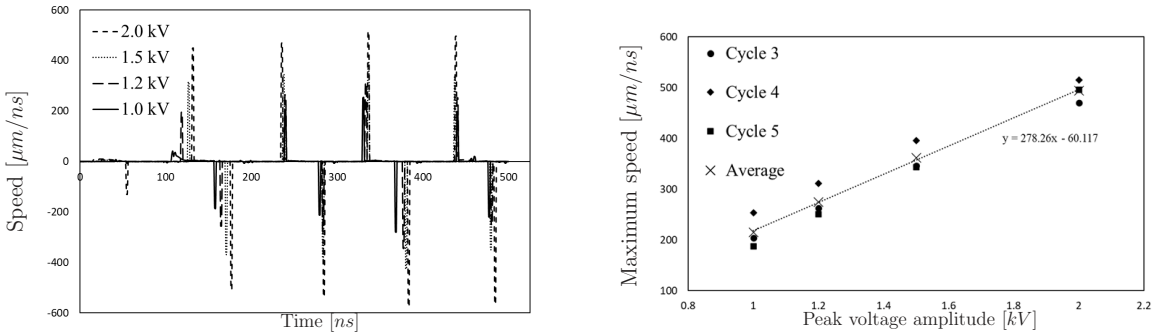

(a) Speed of ion sheath

(b) Maximum speed of ion sheath for cycles 3-5

Figure 5.30: Ion sheath speed for multiple applied voltage amplitudes

Simulations supplying DBD actuators with a constant voltage pulse of similar magnitudes to this work have produced plasma front speeds on the order of 1 μm/ns, where secondary electron emission from the dielectric surface is the only source of free electrons in front of the plasma [25, 79]. The position of the ion sheath throughout each cycle in Figure 5.29(a) shows the ion sheath rapidly propagating to the downstream extent of the plasma, gradually expanding further down the dielectric surface, and then rapidly propagating back towards the edge of the electrode. The rapid propagation of the ion sheath from the edge of the exposed electrode to the downstream extent of the plasma produces speeds on the order of hundreds of μm/ns. However, during the times when the plasma region is gradually expanding (highlighted for the 2 kV case in Figure 5.31(a)) the ion sheath obtains speeds on the order of one to ten μm/ns. Therefore, Figure 5.31(b) is included to analyse the ion sheath speed during the first cycle and gradual expansion of the plasma. Here, similar speeds to Boeuf and Pitchford [25] and Nishidia and Abe [79] are observed. This suggests that during the time of gradual plasma expansion, secondary electron emission is the main mechanism influencing the propagation of the ion sheath. Additionally, during the positive half of the first cycle, the plasma gradually expands along the dielectric surface as shown in Figures 5.31(a). Here, the ion sheath speeds are significantly lower compared to the following cycles, indicating that the first cycle is only dependent on secondary electron emission for plasma propagation as the original surface is uncharged.

The ion sheath speeds during the first cycle and the times of gradual expansion are significantly lower than those achieved by the NS-DBD actuator throughout the voltage cycles. This suggests that a combination of secondary electron emission and the residual surface charge coupled with an increased concentration of charged particles influences the propagation of NS-DBD produced plasmas. Previous works by

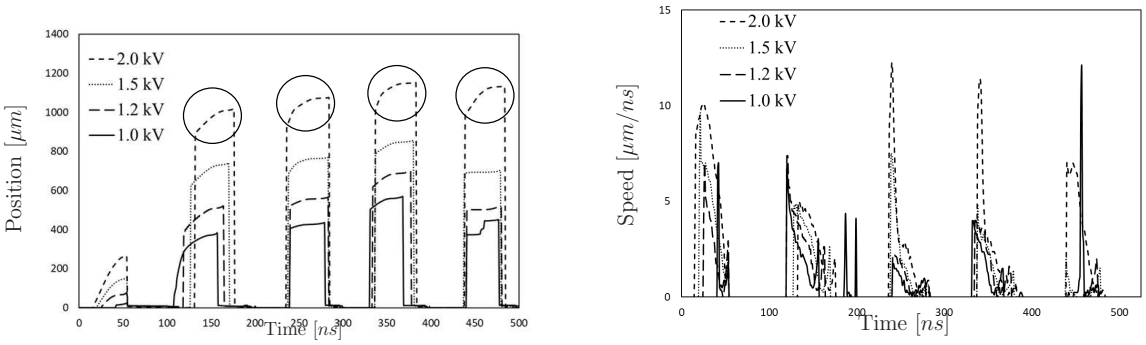

(a) Position of ion sheath

(b) Ion sheath speed

Figure 5.31: Ion sheath speed during gradual plasma propagation

Boeuf et al. [40] and Benard and Moreau [41] have shown a significant dependence of plasma development on the slew rate of the applied voltage signal. Therefore it is expected that the NS-DBD actuators, which employ high slew rates, would have significantly higher propagation rates compared to constant pulse or AC-DBD actuators with small slew rates. The experimental work of Deng et al. [63] observed a 3-8 times increase in the ion sheath speed during the second cycle compared to the first on an uncharged surface, indicating that the residual surface charge significantly influences the plasma front propagation rate. This is in agreement with the results presented here where the speed of all plasmas increased by a minimum factor of 6 from cycle 1 to 2.

This section analysed the resulting plasma formation when the voltage supplied to the electrode was varied from 1 - 2 kV with the pulse duration kept constant at 100 ns. Significant changes are observed in the positive ion and electron distributions over the first two cycles before achieving a quasi-steady configuration for the remaining cycles. The results also show that increasing the voltage increases both the length and height of that plasma, where further analysis of the ion sheath position shows an approximately linear relationship between the plasma length and applied voltage.

Additionally, the ion sheath speeds are shown to range from tens of μm/ns to hundreds of μm/ns throughout each cycle indicating the ion sheath propagation is dependent on a combination the residual surface charge on the dielectric and secondary electron emission from the dielectric.

Chapter 6

Results: Effects of pulse duration on plasma development

To observe the effect of the pulse duration on the results, simulations are run with the pulse durations of 50, 100, and 200 ns while the peak voltage amplitude is kept constant at 1.5 kV as shown in Figure 6.1. All simulations are run over five complete voltage cycles.

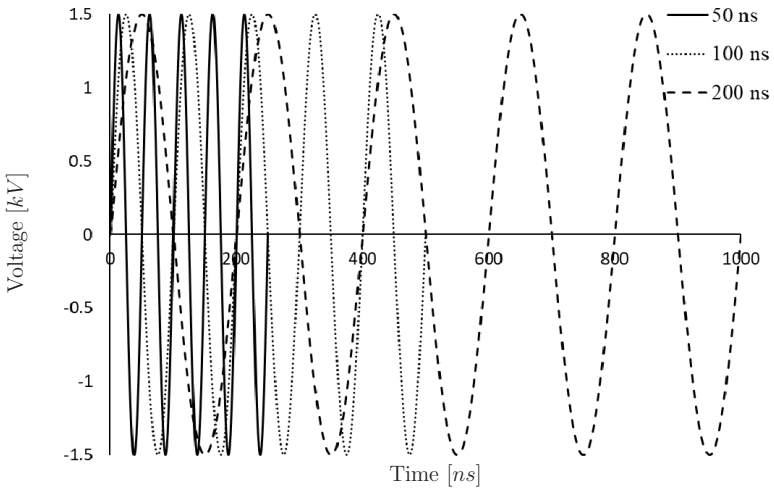

Figure 6.1: Various applied voltage profiles

6.1 Pulse duration effect on charged particle distribution and surface charge

This section compares the resulting charged particle distributions and the surface charge generated on the dielectric from the 200 ns case and the 50 ns case. For all figures, the top figure displays the 200 ns results and the bottom figure displays the 50 ns results which have been flipped in the vertical direction to mirror the 200 ns case.

6.1.1 Cycle 1

The distribution of positive ions as the electrode first reaches the peak positive potential is displayed in Figures 6.2. By this time, the 200 ns case has developed a plasma region significantly larger than the 50 ns case. Both cases have similar electric fields, however, as the pulse duration is increased the electric field has longer to expand throughout the domain which allows for ionization to occur further downstream from the exposed electrode and thus generates a larger plasma region. An ion sheath is visible for for the 200 ns case in Figure 6.2 while ionization is observed to just be starting for the 50 ns case.

A negligible surface charge has developed along the dielectric in Figure 6.3 for the 50 ns case while a positive surface charge spanning approximately 150 μm is observed for the 200 ns case. The positive peak coincides with the maximum concentration of positive ions and is used to identify the location of the ion sheath. The difference in the surface charge generated by the two cases shows that increasing the pulse duration increases the size of the plasma generated as the potential on electrode has longer to ionize the flow.

As the charge on the electrode returns to 0 V, ion sheath generated by the 200

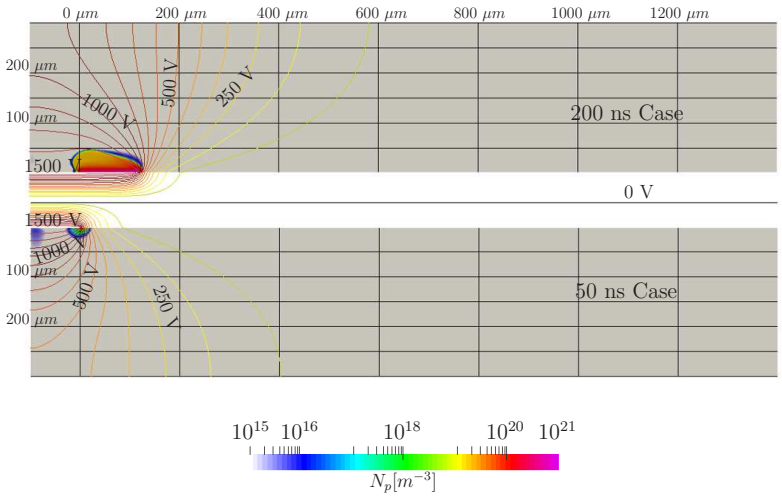

Figure 6.2: Positive ion concentration at 1/4 phase during cycle 1

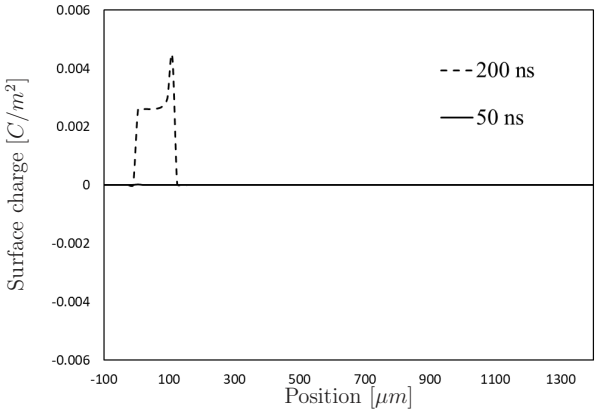

Figure 6.3: Dielectric surface charge at 1/4 phase during cycle 1

ns case is observed to split as indicated by the electric potential lines in Figure 6.4 and the two positive peaks in the surface charge as seen in Figure 6.5. The plasma length has increased by 200 μm for the 200 ns case, now spanning 350 μm down the dielectric while the plasma generated by the 50 ns case has only slightly increased in size. Additionally, the electric potential for the 50 ns case is significantly lower than the 200 ns case, having a maximum value of 250 V compared to 400 V in the 200 ns case due to the late formation of the ion sheath for the 50 ns case (similar to the behaviour observed from the 1 kV case in the previous chapter).

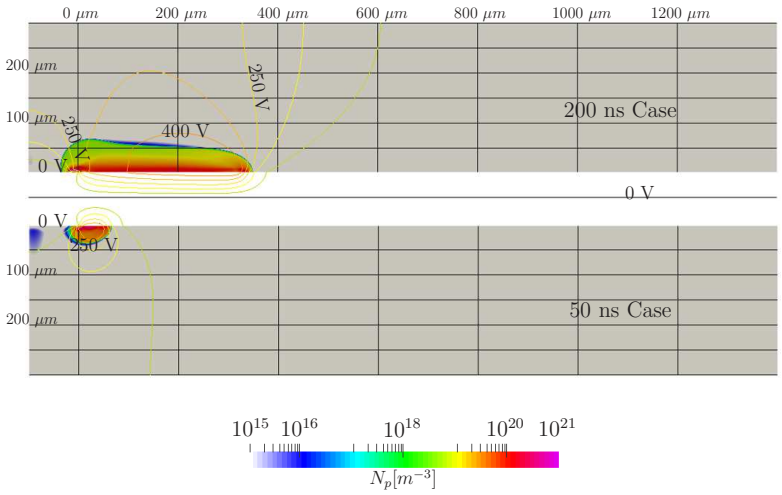

Figure 6.4: Positive ion concentration at 1/2 phase during cycle 1

The positive surface charge on the dielectric continues to develop as the plasma expands along the surface as shown in Figure 6.5. Both cases have positive peaks of similar magnitude as the maximum concentration of positive ions in Figure 6.4 are both on the order of 10^{20} m^{-3}. Due to both cases having the same potentials applied to the electrode it is expected that surface charges of similar magnitudes should develop, with the charge expanding further down the dielectric as the pulse duration is increased. The positive peak in the surface charge for the 50 ns case indicated that an ion sheath formed between 25 and 50 ns as the slope of the voltage began to decrease similar to the results of the 1 kV case in the previous section (see Figure 5.9).

The distribution of positive ions during the negative half of the cycle is displayed in Figure 6.6 where similar behaviour seen in Figures 5.10(a) and 5.13(a) is observed. Two ion bubbles form, with the ion bubble A extending 300 μm further downstream for the 2 ns case compared to the 50 ns case. This is because the electric field generated by the potential of the electrode has more time to expanded further throughout the domain for the 200 ns case, allowing for ionization to occur at further extents

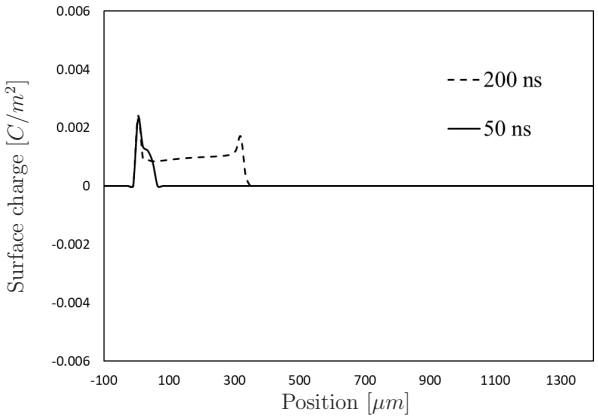

Figure 6.5: Dielectric surface charge at 1/2 phase during cycle 1

downstream. The positive ion bubbles expands as the voltage returns to zero on the dielectric in Figure 6.6(b) while the concentration of positive ions in ion bubble A significantly decreases in the 200 ns case. Because the potential changes polarity quicker for the 50 ns case, the charged particles have less time to travel resulting in a higher concentration of positive ions remaining next to the electrode for the 50 ns case.

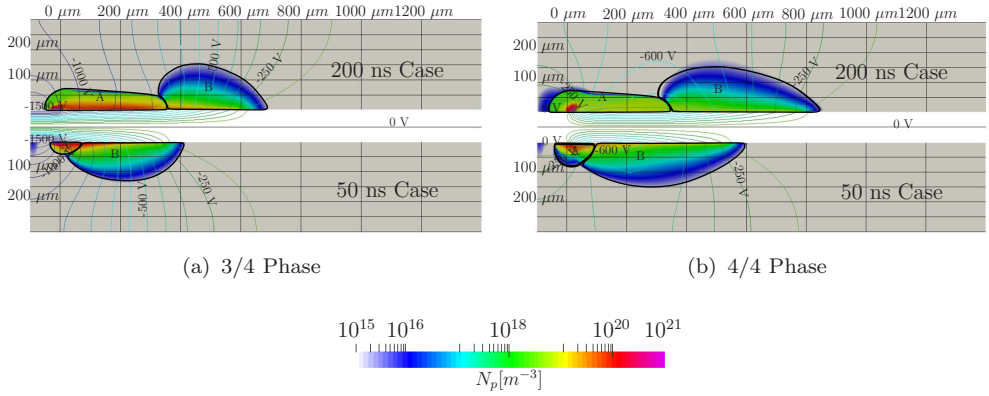

(a) 3/4 Phase

(b) 4/4 Phase

Figure 6.6: Positive ion concentrations at 3/4 and end phase of cycle 1

As the charge on the electrode becomes negative, a negative surface charge develops along the dielectric as the electrons propagate down the surface away from the electrode as shown in Figure 6.7. Both cases have positive peaks in Figure 6.7(a)

corresponding to the location of the ion sheath. The peak is larger for the 50 ns case due to the late formation of the ion sheath next to the exposed electrode. This results in the 50 ns case having a higher concentration of positive ions next to the electrode compared to the 200 ns case where the ion sheath is split as the voltage begins to decrease during the positive half of the cycle. Similar behaviour is noted for the 1 kV case as seen in Figures 5.12 and 5.15. The negative charge on the surface is similar in magnitude for the two cases in both Figures 6.7(a) and (b) with the charge from the 200 ns case extending approximately 350 μm further than the resulting 50 ns charge.

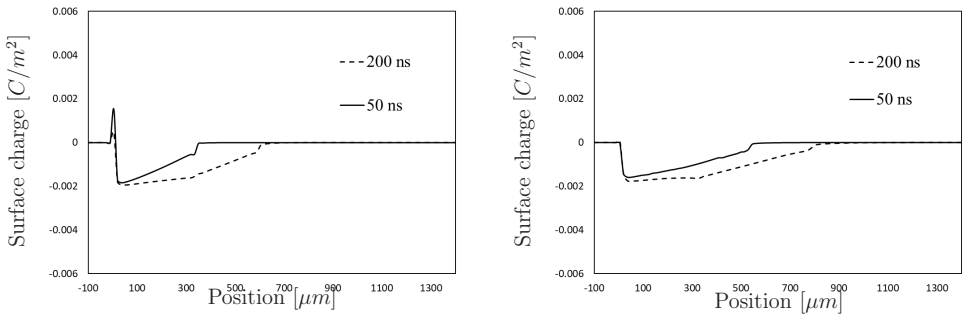

(a) 3/4 Phase

(b) 4/4 Phase

Figure 6.7: Dielectric surface charge at 3/4 and end phase of cycle 1

By the end phase of both voltage cycles, the maximum concentration of electrons has increased by approximately seven orders of magnitude. Additionally, a negative residual surface charge is present along the dielectric, extending 900 μm and 550 μm for the 200 ns and 50 ns cases respectively. The results observed during the first cycle are similar to the previous chapter, however, a difference worth noting is the increased electron density observed for the shorter pulse where the concentration of diffuse electrons being between 10^{17} and 10^{18} m^{-3}. The concentration of electrons is two orders of magnitudes larger in the 50 ns case than what is observed in the 200 ns case, therefore the reaction rates within the plasma generated from the 50 ns case will be significantly higher.

6.1.2 Cycle 2

The distribution of positive ions and electrons during the positive half of the second cycle is displayed in Figures 6.8 and 6.9, with the surface charge displayed in Figure 6.10. The distribution of the charged particles and surface charge during the negative half are included in Figures 6.11, 6.12, and 6.13. As noted during the end phase of the first cycle, the increased concentration of electrons in the 50 ns case generates a plasma region with a significantly higher concentration of both positive ions and electrons compared to the 200 ns case as seen in Figures 6.8(a) and 6.9(a). This trend is maintained throughout the entire cycle, where the charged particle concentrations are notably higher for the 50 ns case. A similar result is noted by Forte et al. [47], where ionization in the plasma region is enhanced as the period of the AC cycle was reduced.

Throughout the second cycle, the plasma behaviour is similar to that discussed in the previous chapter. The ion sheath becomes more diffuse as the electric potential lines are now observed to penetrate through the plasma in Figures 6.8(a) and (b), while the surface charge developed as displayed in Figures 6.10(a) and (b) is similar to that seen in Figures 5.18 and 5.20.

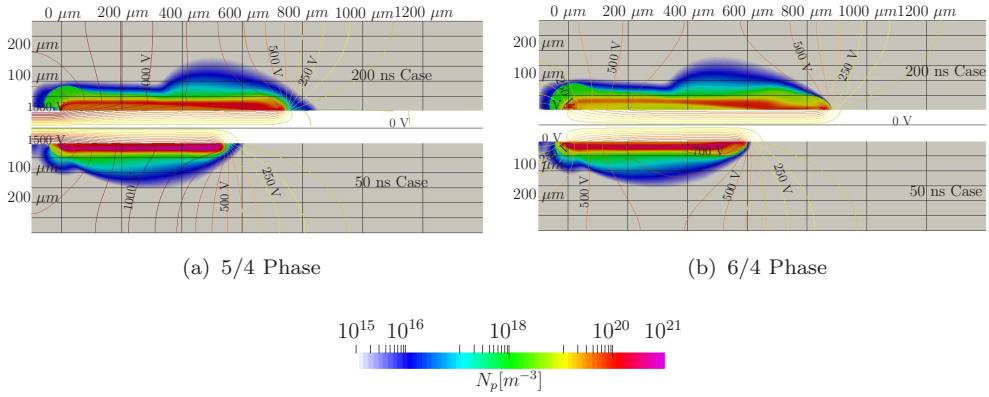

(a) 5/4 Phase

(b) 6/4 Phase

Figure 6.8: Positive ion distribution during the positive half of cycle 2

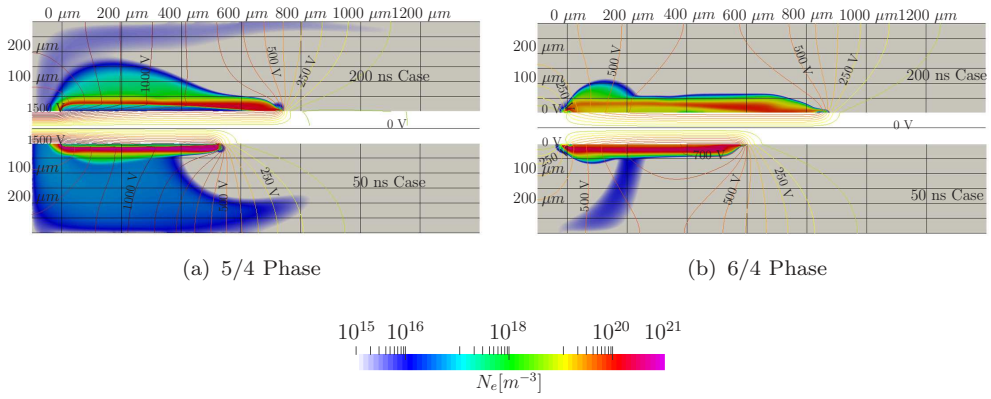

(a) 5/4 Phase (b) 6/4 Phase

Figure 6.9: Electron distribution during the positive half of cycle 2

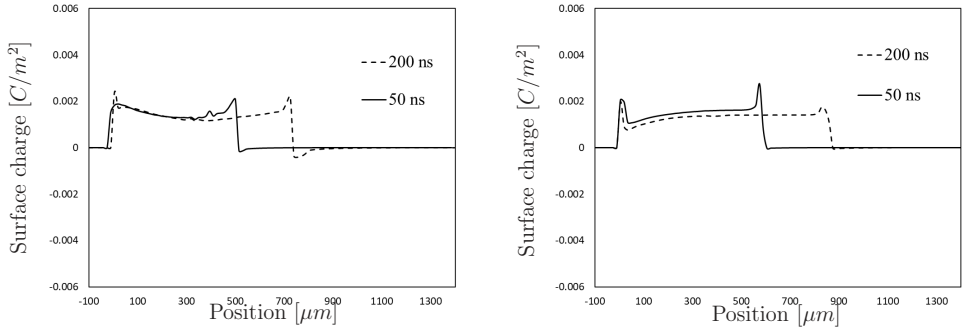

(a) 1/4 Phase (b) 1/2 Phase

Figure 6.10: Dielectric surface charge during the positive half of cycle 2

Throughout the negative half of the cycle, the ions behaviour in Figures 6.11(a) and (b) is similar to that seen in Figures 5.21(a) and 5.23(a). However, a difference noted is the presence of a positive electric field just ahead of the plasma region in the 200 ns case. As previously discussed, the electric field can expand further throughout the domain for the 200 ns case due to the increase in the pulse duration. This also means it will take longer for the electric field in the domain to be impacted by the charge on the exposed electrode, resulting in a residual positive electric field being present during the negative half of the cycle. Another difference between the two cases at this time is the formation of a small ion bubble C at the end of the plasma region in the 50 ns case in Figure 6.11(a). By the end phase of the cycle this third ion

bubble is observed for both cases in Figure 6.11(b). Once again, the concentration of charged particles for the 50 ns case is higher than that of the 200 ns case, indicating that as the pulse duration is decreased, the charged particles remain closer to the surface of the dielectric.

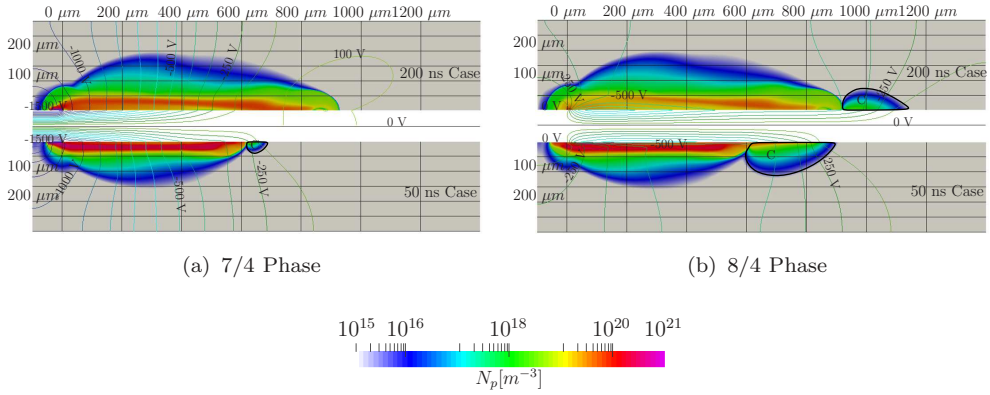

(a) 7/4 Phase (b) 8/4 Phase

Figure 6.11: Positive ion distribution during the negative half of cycle 2

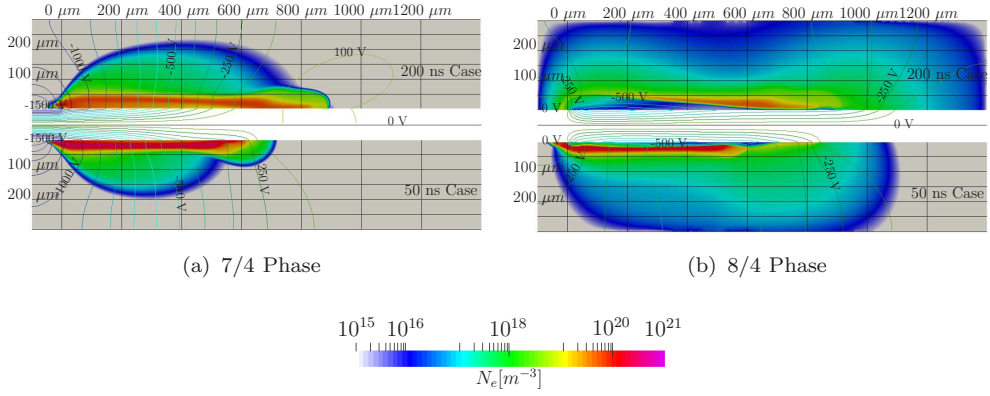

(a) 7/4 Phase (b) 8/4 Phase

Figure 6.12: Electron distribution during the negative half of cycle 2

6.1.3 Cycles 3-5

As more cycles are completed, the charged particles begin to achieve quasi-steady configurations. This indicates that the pulse duration does not significantly impact the number of voltage cycles required to achieve a steady-state plasma. Therefore,

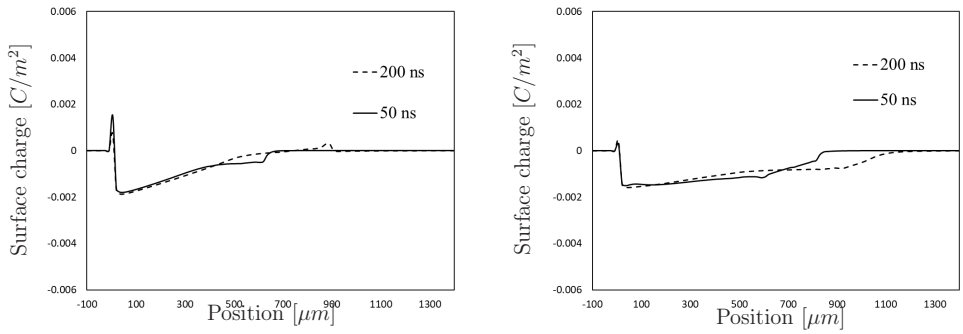

(a) 3/4 Phase

(b) End Phase

Figure 6.13: Dielectric surface charge during the negative half of cycle 2

from the third cycle and onwards the positive ions are displayed in Figure 6.14, the electrons in Figure 6.15, and the surface charge in Figure 6.16.

The distribution of positive ions does not significantly change throughout each voltage cycle or as more cycles are completed. Observing Figure 6.14, the plasma spans approximately 1000 μm for the 200 ns pulse case and 900 μm for the 50 ns pulse case. Although there is not a large difference in the size of the plasma region between the two cases, there is a significant difference in the amount of positive ions within the plasma. The 50 ns case has a fairly uniform region of positive ions along the dielectric surface that is an order of magnitude higher than the concentration seen in the 200 ns case. Both cases produce plasma having heights of approximately 200 μm, and both develop small ion bubbles at the downstream extent of the plasma region in Figures 6.14(h) and (l). Overall, the positive ion distribution is fairly similar once a quasi-steady plasma configuration has been achieved regardless of the pulse duration.

Similar results are observed in the electron distribution over the remaining cycles in Figures 6.15. Like the positive ions, the 50 ns case has a uniform region of an increased concentration of electrons near the surface of the dielectric. Although

the electrons are highly mobile, the short pulse duration of the 50 ns pulse prevents them from diffusing throughout the domain to the same extent observed in the 200 ns case. This also causes residual electrons to remain in the domain throughout the voltage cycle as seen in Figures 6.15(b), (f), and (j).

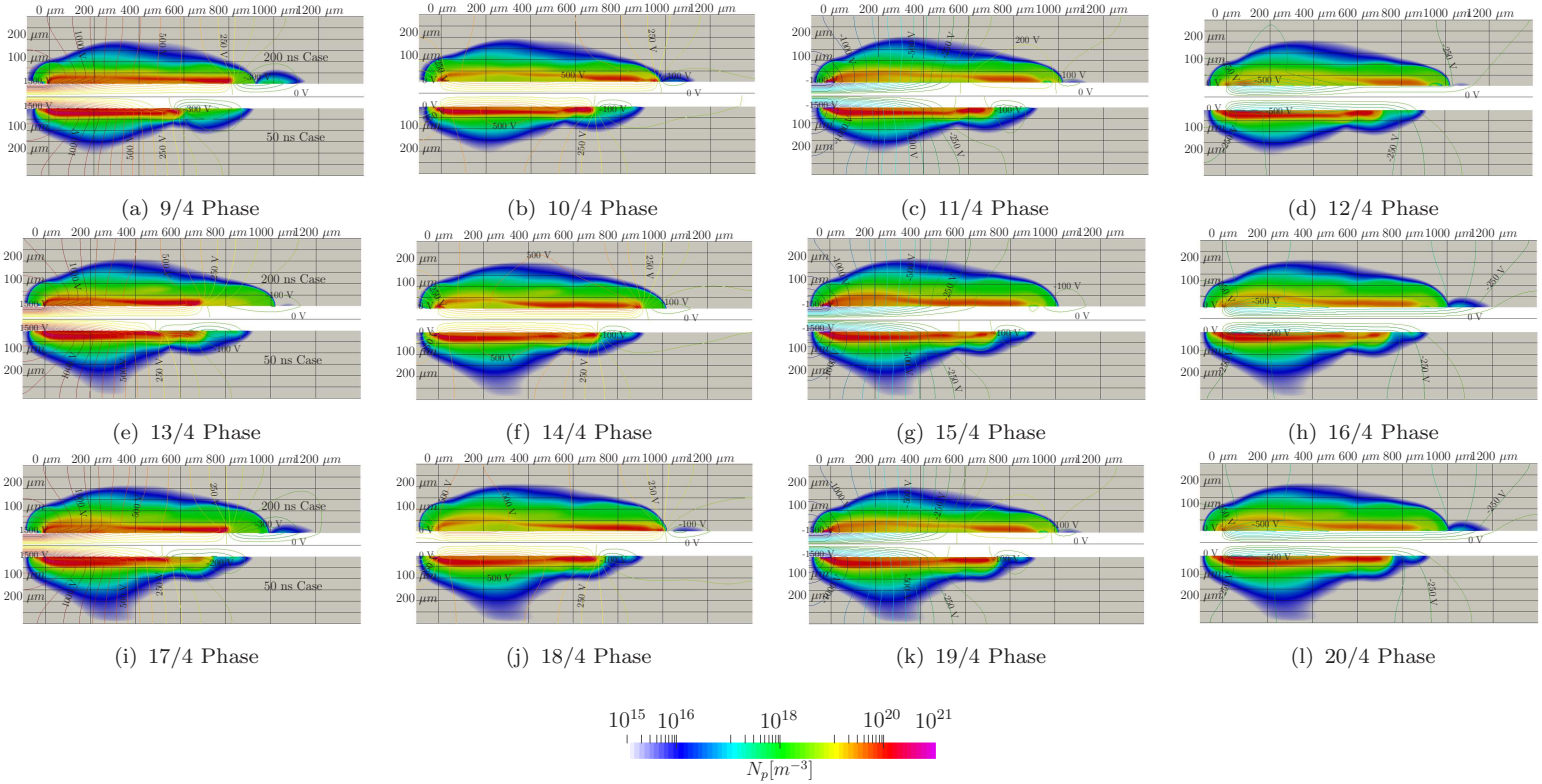

(a) 9/4 Phase (b) 10/4 Phase (c) 11/4 Phase (d) 12/4 Phase

(e) 13/4 Phase (f) 14/4 Phase (g) 15/4 Phase (h) 16/4 Phase

(i) 17/4 Phase (j) 18/4 Phase (k) 19/4 Phase (l) 20/4 Phase

Figure 6.14: Positive ion distribution for the remaining cycles

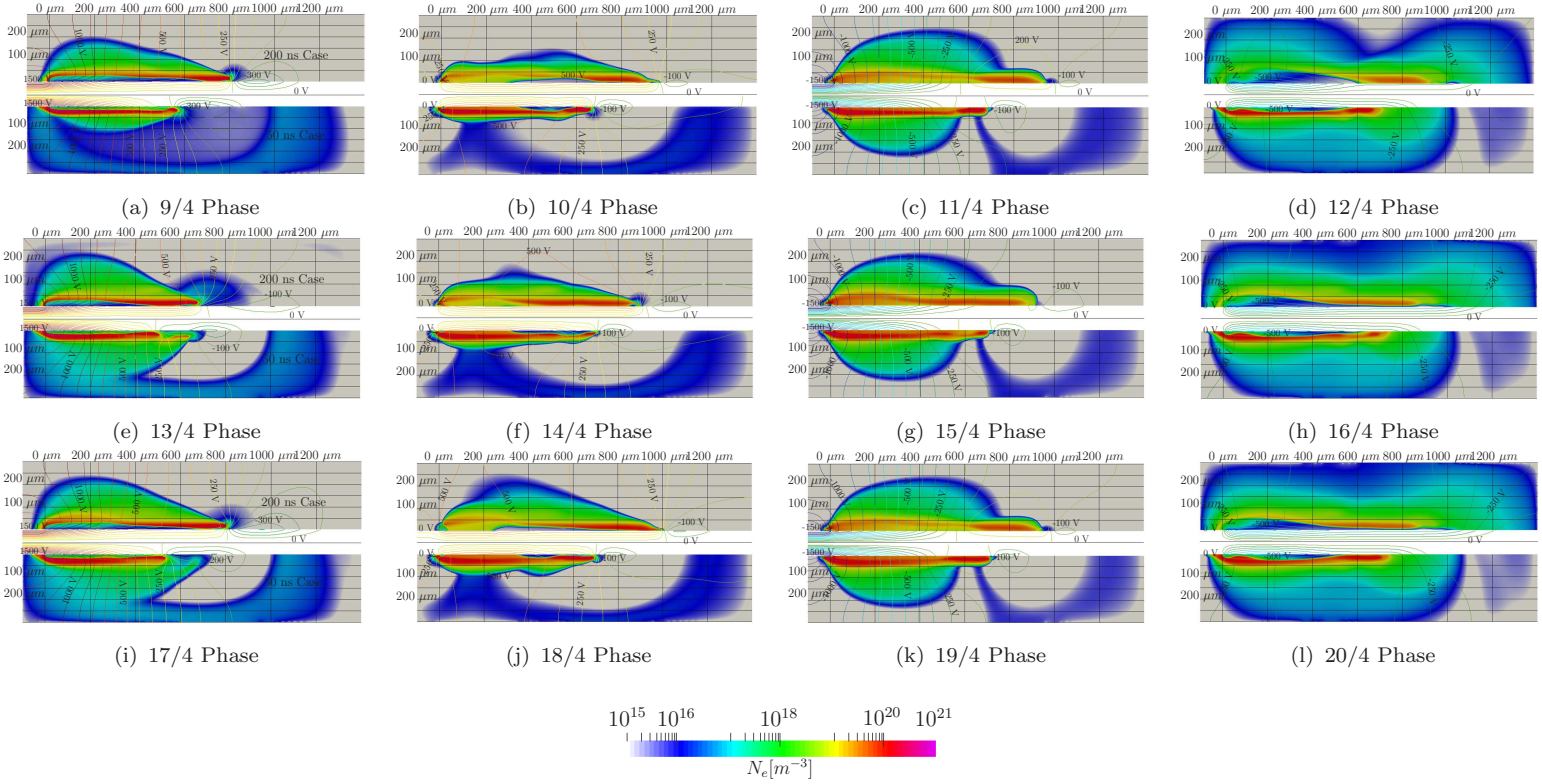

(a) 9/4 Phase (b) 10/4 Phase (c) 11/4 Phase (d) 12/4 Phase

(e) 13/4 Phase (f) 14/4 Phase (g) 15/4 Phase (h) 16/4 Phase

(i) 17/4 Phase (j) 18/4 Phase (k) 19/4 Phase (l) 20/4 Phase

Figure 6.15: Electron distribution for the remaining cycles

The surface charge developed along the dielectric has similar magnitudes for the different pulse durations, just different extents due to the longer pulse generating a larger plasma region as seen in Figure 6.16. During the positive half of the voltage cycle, the transition from a positive to negative surface charge is delayed for the 200 ns in Figures 6.16(a), (e), and (i). Here, the positive charge on the dielectric surface extends further downstream compared to the 50 ns case. This is also noted during the negative half of the voltage cycle in Figures 6.16(c), (g), and (k), where the residual positive charge on the dielectric surface at the downstream extent of the plasma region is more positive for the 200 ns case compared to the 50 ns case. Observing the positive ion distribution in Figures 6.14, an elevated concentration of ions remains downstream of the exposed electrode throughout the entire cycle for the 200 ns case, while the 50 ns case has a uniform distribution of ions along the dielectric surface. This contributes to the surface charge remaining more positively charged downstream from the electrode for the 200 ns case throughout the voltage cycles.

This section analyses the behaviour of the charged particles and the resulting surface charge generated on the dielectric when the pulse duration is varied. The main difference between the 200 ns and 50 ns cases is the size of the plasma generated and the concentration of charged particles within the plasma. The plasma from the 200 ns case extends further downstream on the dielectric surface, however, the 50 ns case produces a plasma having a higher concentration of charged particles that remains in a fairly uniform distribution along the dielectric. The surface charge generated on the dielectric from the plasma regions are very similar in magnitude for the two cases, where the main difference is the extent of the charge. For further analysis of the effects of the applied pulse duration, the following sections will examine the propagation of the ion sheath.

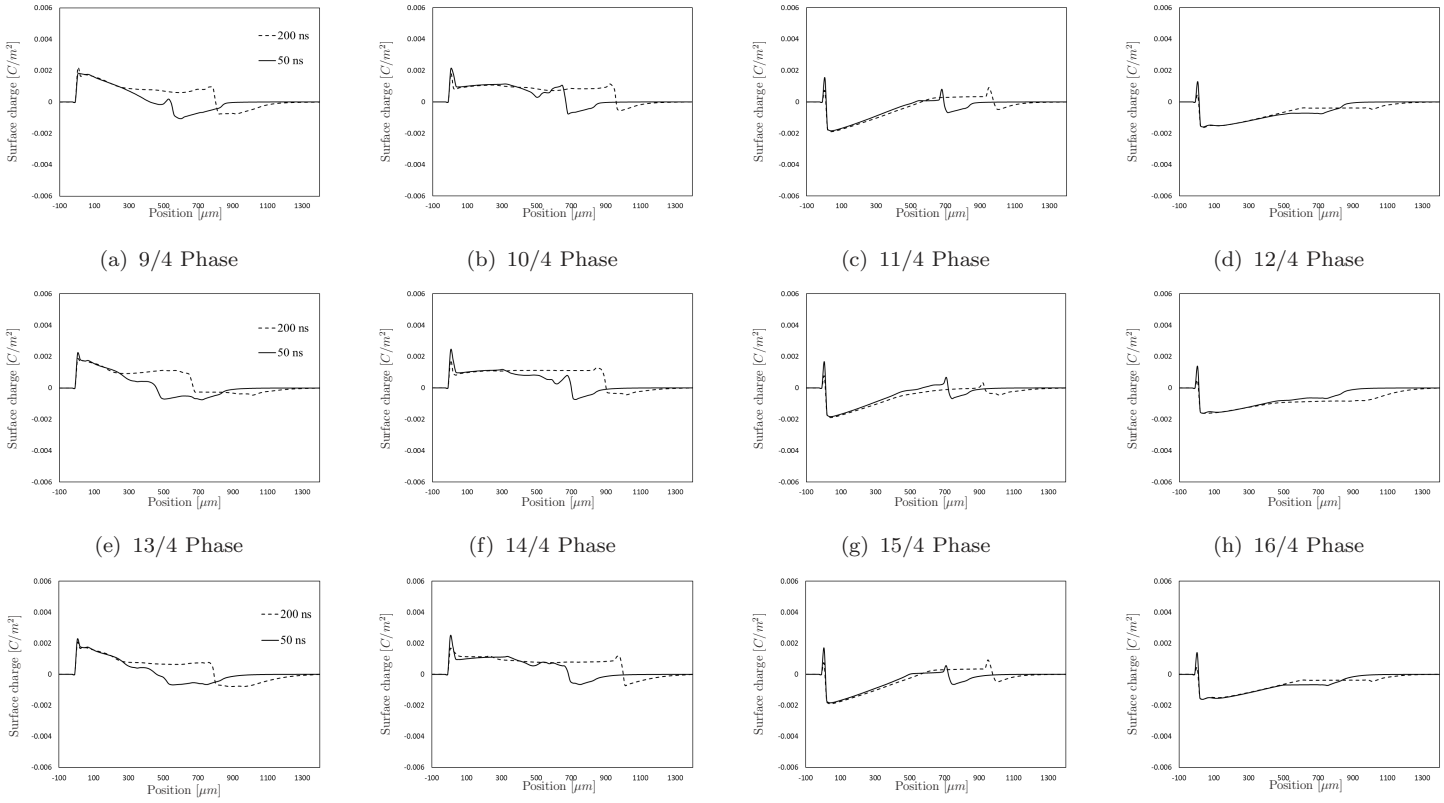

(a) 9/4 Phase (b) 10/4 Phase (c) 11/4 Phase (d) 12/4 Phase

(e) 13/4 Phase (f) 14/4 Phase (g) 15/4 Phase (h) 16/4 Phase

(i) 17/4 Phase (j) 18/4 Phase (k) 19/4 Phase (l) 20/4 Phase

Figure 6.16: Dielectric surface charge for the remaining cycles

6.2 Pulse duration effect on plasma length and ion sheath speed

Similar to the results presented in the previous chapter, the position of the ion sheath is estimated based on the maximum value of the horizontal electric field (E_x) along the surface of the dielectric. Figure 6.17(a) displays the position of the ion sheath along the dielectric surface over time, while Figure 6.17(b) shows the maximum extent of the ion sheath during cycles 3 through 5 versus the applied pulse duration. During the first cycle, the 200 ns pulse case is able to establish a plasma region significantly larger than the other cases due to the electric field having longer to expand throughout the domain, which results in the ion sheath travelling significantly further downstream compared to the 50 ns and 100 ns pulse cases. As the second voltage cycle begins, all cases display rapid ion sheath propagation, where the maximum ion sheath extent increases by 952% for the 50 ns case, 385% for the 100 ns case, and 168% for the 200 ns case compared to the first cycle. As noted in the previous chapter, the plasma gradually increases throughout each voltage cycle, where the 100 ns case reaches an approximate maximum during the fourth cycle. Similar to the voltage, the plasma region increases linearly with the pulse duration as seen by the trend line of the average maximum position values in Figure 6.17(b).

During the fifth cycle, the 50 ns pulse and 200 ns pulse cases are able to match the extents reached during the fourth cycle as seen in Figure 6.17(b). However, the maximum extent for the 100 ns case is significantly reduced in magnitude during the last cycle. Figure 6.18 displays the concentration of electrons during the fifth cycle for all cases. The presence of an electron void is discussed in the previous chapter, however, neither the 50 ns pulse or 200 ns pulse case develops one. Meanwhile, in the 100 ns case a significant electron void develops during the end phase of the voltage

cycle. This void limits the downstream propagation of the ion sheath due to the lack of electrons available for ionization and thus the extent of the plasma is reduced during the fifth cycle similar to the results from the 1 kV case in the previous section.

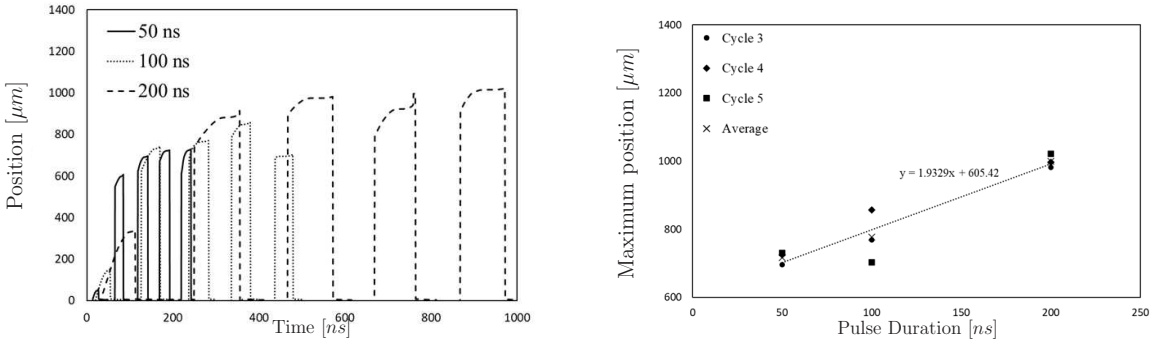

(a) Position of ion sheath

(b) Maximum position of ion sheath for cycles 3-5

Figure 6.17: Ion sheath position for multiple pulse durations

The speed of the ion sheath over the five voltage cycles is displayed in Figure 6.19(a), while the maximum positive speed reached during cycles 3 through 5 versus the pulse duration is displayed in Figure 6.19(b). Again, the ion sheath speeds are on the order of 100's of μm/s, where the values range from 315-675 μm/s, with the negative going speeds being higher than the positive going speeds due to the gradual increase in the plasma extent. Although the 200 ns case produces the largest plasma region, the 50 ns case is observed to obtain the highest speeds in Figure 6.19(b). This is attributed to the rapid change in polarity for the shorter pulse which forces the ion sheath to propagate quicker than the other cases. Examining Figure 6.19(b), the ion

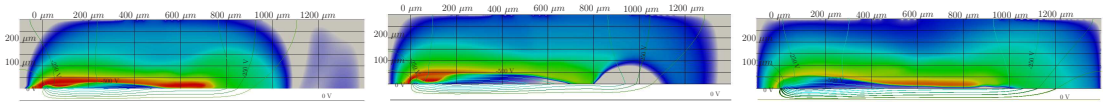

(a) 50 ns case

(b) 100 ns case

(c) 200 ns case

Figure 6.18: Electron distribution at the end phase of the fifth cycle for all pulse durations

sheath speeds are found to increase each cycle up until the fourth. A slight decrease in the speed is noted for the 50 and 100 ns cases, while a slight increase is observed for the 200 ns case during the fifth cycle due to the change in plasma extents.

Where the shorter pulses change polarity quicker than the longer cases, it would be expected that the ion sheath speed would decrease as the pulse duration would increase. While the results in Figure 6.19(b) do show that the ion sheath from the 50 ns pulse case travels significantly quicker than the other cases, the ion sheath from the 100 ns pulse case is observed to travel slower than the 200 ns pulse case. The reduction in ion sheath speed for the 100 ns case is due to the interference of the electron void in the 100 ns pulse case shown in Figure 6.18(b), where the maximum plasma extent is limited, thereby reducing the distance the ion sheath travels.

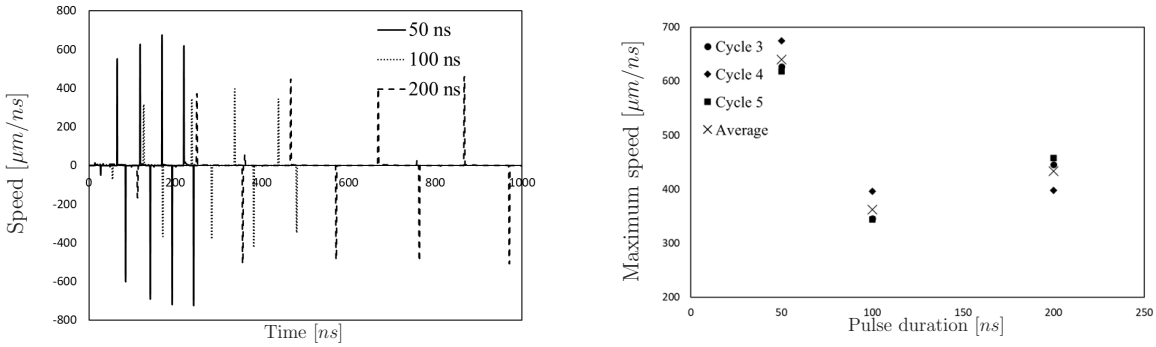

(a) Speed of ion sheath

(b) Maximum speed of ion sheath for cycles 3-5

Figure 6.19: Ion sheath speed for multiple pulse durations

This chapter analysed the resulting plasma when the pulse duration of the applied voltage is varied from 50 to 200 ns. The results show similar results to the various voltage cases, where a minimum of three cycles are required before the charged particles achieve a quasi-steady configuration. Varying the pulse duration did not significantly effect the overall length or heigh of the plasma region, however, as the pulse duration is decreased, the concentration of charged particles within the

plasma increases due to the rapid change in polarity of the charge on the electrode. The rapid change in polarity also increases the speed of the ion sheath where the ion sheath developed by the 50 ns case achieved the highest speeds.

Chapter 7

Conclusions and Recommendations

7.1 Conclusions

As mentioned in Section 2.5, this work aims to analyse how the plasma develops as the input electrical parameters are varied and to study the time dependency of the plasma properties. Simulations are performed in quiescent flow with a sinusoidal waveform supplied to the exposed electrode. The solver developed by Murzionak [74] has previously been validated by results in the literature when supplied with a constant voltage pulse and has been modified to supply the exposed electrode with a sinusoidal waveform. The voltage amplitude and pulse duration (sinewave frequency) are varied to analyse their effect on the plasma formation.

It is shown that supplying the plasma actuator with a higher voltage amplitude results in a larger plasma region forming along the dielectric. As the voltage amplitude is increased, an electric field sufficient for ionization is established earlier and expands further downstream from the electrode. Analysing the charged particle densities and the ion sheath propagation, the 2 kV case, 50 ns case, and 200 ns case successfully develops a plasma region free of electron voids at the downstream extent of the

plasma region over five voltage cycles. The results from the lower voltage cases and the 100 ns case show a growing electron void forming at the end phase of each voltage cycle. This void reduces ionization and restricts further plasma development. Ion sheath speeds similar to the literature are observed, with the speed increasing with the applied voltage. The ion sheath has a higher speed when travelling towards the exposed electrode due to the plasma gradually expanding throughout the voltage cycle. During the gradual expansion of the plasma, the ion sheath has speeds similar to those observed in the literature of DBD actuators supplied with constant voltage pulses of similar magnitudes. This suggests that when the plasma region is gradually expanding throughout the sinusoidal voltage cycle, secondary electron emission is the main mechanism influencing the plasma propagation at this time. However, due to the large difference in ion sheath speeds over the entire voltage cycle, the results suggest that a combination of both the residual surface charge on the dielectric surface and secondary electron emission are responsible for influencing the ion sheath propagation.

Additional simulations varying the pulse duration show that longer pulses establish larger plasma regions due to the electric field having more time to expand throughout the domain, allowing for ionization to occur further downstream. Although the longer pulse case generates a larger region of plasma, the charged particle densities in the 50 ns pulse case are significantly higher due to the particles having less time to diffuse throughout the domain. The rapid change in polarity for this case results in a fairly uniform distribution of charged particles along the surface of the dielectric, with the charged particle densities being at least one order of magnitude higher than the 200 ns pulse case over the same voltage cycles. The various pulse durations produce similar surface charge magnitudes, where the extent of the surface charge increases with the pulse duration due to the plasma expanding further along

the dielectric. When analysing the ion sheath propagation, the 50 ns and 200 ns pulses follows trends observed in the literature for AC DBD actuators. However, the 100 ns case developed a large electron void during the end phase of the voltage cycle which was not observed in the other cases.

Due to the conditions in the computational domain changing significantly at the start of the second cycle compared to the first cycle (at start-up), the plasma parameters vary largely throughout the first two voltage cycles. A notable increase in the concentration of charged particles and the ion sheath propagation is observed during the second cycle for all cases analysed in this work. From the third cycle onwards, the cases display a quasi-steady plasma configuration with little change in parameters, indicating a steady-steady state had been reached. The strong time dependency of the plasma during the first couple of cycles emphasizes that care should be taken when averaging plasma parameters for cyclic voltage cycles.

7.2 Recommendations

This work employed a high-fidelity numerical model of an NS-DBD actuator to gather the data discussed in the previous chapters. Although this model offers detailed insight into the behaviour of the charged particles within the plasma region, the mesh element size and time scale required to properly resolve the plasma is computationally demanding and thus incorporating features such as negative ions or a non-quiescent background flow is difficult. Therefore, some methods that could improve the computational performance of the current solver include using a dynamic mesh instead of a static mesh or incorporating the model proposed by Parent et al. [80].

A dynamic mesh is a mesh that allows for refinement to occur throughout the simulation as certain conditions are met. By implementing a dynamic mesh into the

current solver, the refinement of the mesh could be restricted to the plasma region while a coarser mesh would be employed everywhere else, thus reducing the number of elements in the computational domain. Reducing the number of elements would allow the solver to be implemented into larger models without drastically increasing the number of elements. Preliminary work on this modification has been completed, however, more time dedicated to ensuring the stability of the code during the initialization of the simulation is required.

The model proposed by Parent et al. [80] involves using Ohm's law in place of Gauss' law to solve the electric field. Current fluid models, including the one used for this work, solve the electric field using Gauss's law, however, when discretized these models become significantly stiff in regions where the positive charge density approaches the negative charge density (quasi-neutral regions). This stiffness is significantly reduced when using Ohm's law and the time-step can be increased. The results from Parent et al. [80] show a hundredfold reduction in the number of iterations required to reach convergence in quasi-neutral plasma while producing a numerical error no larger than the model based on Gauss's law.

Incorporating these modifications into the current solver would significantly reduce the computational cost. This would allow for the solver to be implemented into models to study plasma effects on background flows, including shockwave-boundary layer interactions in hypersonic flow, where early studies have shown promise in using plasmas to prevent inlet unstart in scramjets and airbreathing engines.

References

[1] W. Shyy, B. Jayaraman, and A. Andersson. Modeling of glow discharge-induced fluid dynamics. *Journal of Applied Physics*, 92(11):6434–6443, 12 2002.

[2] *Applications to Nonthermal Plasma Processing*. IOP Bristol, 2001.

[3] J. Roth, Daniel Sherman, and Stephen Wilkinson. *Boundary layer flow control with a one atmosphere uniform glow discharge surface plasma*.

[4] Young-Chang Cho and Wei Shyy. Adaptive control of low-reynolds number aerodynamics in uncertain environments: Part 1. disturbance regimes and flow characteristics. *Computers & Fluids*, 86:582–596, 2013.

[5] Young-Chang Cho and Wei Shyy. Adaptive control of low-reynolds number aerodynamics in uncertain environments: Part 2. vortex dynamics and system modeling under stall. *Computers & Fluids*, 86:597–610, 2013.

[6] Hatem Abdelraouf, Ahmed M. Nagib Elmekawy, and Sadek Z. Kassab. Simulations of flow separation control numerically using different plasma actuator models. *Alexandria Engineering Journal*, 59(5):3881–3896, 2020.

[7] P. F. Zhang, B. Yan, A. B. Liu, and J. J. Wang. Numerical simulation on plasma circulation control airfoil. *AIAA Journal*, 48(10):2213–2226, 2010.

[8] C. L. Enloe, Thomas E. McLaughlin, Robert D. VanDyken, K. D. Kachner, Eric J. Jumper, and Thomas C. Corke. Mechanisms and responses of a single dielectric barrier plasma actuator: Plasma morphology. *AIAA Journal*, 42(3):589–594, 2004.

[9] YB Suzen, PG Huang, JD Jacob, and DE Ashpis. Numerical simulations of plasma based flow control applications. In *35th Fluid Dynamics Conference and Exhibit*, pages 1–11. American Institute of Aeronautics and Astronautics, 2005.

[10] Y. B. Suzen, P. G. Huang, and D. E. Ashpis. Numerical simulations of flow separation control in low-pressure turbines using plasma actuators. In *45th AIAA Aerospace Sciences Meeting and Exhibit*, Reno, Nevada, 2007. American Institute of Aeronautics and Astronautics.

[11] Kendall Dennis, Yildirim Suzen, and Nihan Uygun. *Simulations of Plasma Flow Control in Low-Pressure Turbines*.

[12] Daniel Reasor, Raymond Lebeau, and Yildirim Suzen. *Unstructured Grid Simulations of Plasma Actuator Models*.

[13] Arvind Santhanakrishnan, Jamey Jacob, and Yildirim Suzen. *Flow Control Using Plasma Actuators and Linear/Annular Plasma Synthetic Jet Actuators*.

[14] Junhui Huang, Thomas C. Corke, and Flint O. Thomas. Plasma actuators for separation control of low-pressure turbine blades. *AIAA Journal*, 44(1):51–57, 2006.

[15] D.M. Orlov. *Modelling and Simulation of Single Dielectric Barrier Discharge Plasma Actuators*. PhD thesis, University of Notre Dame, 2006.

[16] C. Enloe, Thomas McLaughlin, Robert Van Dyken, and John Fischer. *Plasma Structure in the Aerodynamic Plasma Actuator*.

[17] Martiqua L. Post and Thomas C. Corke. Separation control on high angle of attack airfoil using plasma actuators. *AIAA Journal*, 42(11):2177–2184, 2004.

[18] Benjamin Mertz and Thomas Corke. *Time-Dependent Dielectric Barrier Discharge Plasma Actuator Modeling*.

[19] Flint O. Thomas, Alexey Kozlov, and Thomas C. Corke. Plasma actuators for cylinder flow control and noise reduction. *AIAA Journal*, 46(8):1921–1931, 2008.

[20] Gabriel Font. *Boundary Layer Control with Atmospheric Plasma Discharges*.

[21] G. Font and W. Morgan. *Plasma Discharges in Atmospheric Pressure Oxygen for Boundary Layer Separation Control*.

[22] C. L. Enloe, T. E. McLaughlin, G. I. Font, and J. W. Baughn. Parameterization of temporal structure in the single-dielectric-barrier aerodynamic plasma actuator. *AIAA Journal*, 44(6):1127–1136, 2006.

[23] Gabriel Font, Lon Enloe, Tom Mclaughlin, and D Orlov. *Plasma Discharge Characteristics and Experimentally Determined Boundary Conditions for a Plasma Actuator*.

[24] Alexandre Likhanskii. *Particle-in-Cell Modeling of the Pulsed DBD Plasma Actuator*.

[25] J. P. Boeuf and L. C. Pitchford. Electrohydrodynamic force and aerodynamic flow acceleration in surface dielectric barrier discharge. *Journal of Applied Physics*, 97(10):103307, 05 2005.

[26] Alexandre V. Likhanskii and Jonathan Poggie. *On the validation of fluid plasma model for pulsed DBD plasma actuator simulations against full kinetic approach.*

[27] K.P. Singh, Subrata Roy, and Datta Gaitonde. *Modeling of Dielectric Barrier Discharge Plasma Actuator with Atmospheric Air Chemistry.*

[28] Subrata Roy and Datta Gaitonde. *Modeling Surface Discharge Effects of Atmospheric RF on Gas Flow Control.*

[29] Subrata Roy and Datta Gaitonde. *Multidimensional Collisional Dielectric Barrier Discharge for Flow Separation Control at Atmospheric Pressures.*

[30] Kunwar Pal Singh and Subrata Roy. Force approximation for a plasma actuator operating in atmospheric air. *Journal of Applied Physics*, 103(1):013305, 01 2008.

[31] Hiroyuki Nishida and Takashi Abe. *Numerical Analysis for Plasma Dynamics in SDBD Plasma Actuator.*

[32] Hiroyuki Nishida and Takashi Abe. *Validation Study of Numerical Simulation of Discharge Plasma on DBD Plasma Actuator.*

[33] C. L. Enloe, G. I. Font, T. E. McLaughlin, and D. M. Orlov. Surface potential and longitudinal electric field measurements in the aerodynamic plasma actuator. *AIAA Journal*, 46(11):2730–2740, 2008.

[34] Yuji Takizawa, Atsushi Matsuda, Kousuke Kikuchi, Akihiro Sasoh, and Takashi Abe. *Optical Observation of Discharge Plasma Structure in DBD Plasma Actuator.*

[35] Dmitri M. Orlov, Gabriel I. Font, and Daniel Edelstein. Characterization of discharge modes of plasma actuators. *AIAA Journal*, 46(12):3142–3148, 2008.

[36] C. Enloe, T. McLaughlin, J. Gregory, R Medina, and W Miller. *Surface Potential and Electric Field Structure in the Aerodynamic Plasma Actuator.*

[37] Hiroyuki Nishida, Taku Nonomura, and Takashi Abe. *Numerical Analysis on Three-dimensional Body Force Field of DBD Plasma Actuator.*

[38] Hiroyuki Nishida, Taku Nonomura, and Takashi Abe. *Numerical Study of Three-dimensional Effects of Plasma Structure on Flow Field around DBD Plasma Actuator.*

[39] Hiroyuki Nishida, Taku Nonomura, and Takashi Abe. Numerical study on spanwise nonuniformity in body-force field of dielectric-barrier-discharge plasma actuator. *AIAA Journal*, 54(2):659–669, 2016.

[40] J P Boeuf, Y Lagmich, Th Unfer, Th Callegari, and L C Pitchford. Electrohydrodynamic force in dielectric barrier discharge plasma actuators. *Journal of Physics D: Applied Physics*, 40(3):652, jan 2007.

[41] N. Benard and E. Moreau. Role of the electric waveform supplying a dielectric barrier discharge plasma actuator. *Applied Physics Letters*, 100(19):193503, 05 2012.

[42] Asa Nakano and Hiroyuki Nishida. The effect of the voltage waveform on performance of dielectric barrier discharge plasma actuator. *Journal of Applied Physics*, 126(17):173303, 11 2019.

[43] Asa Nakano, Yutaka Kaneko, and Hiroyuki Nishida. *Investigation on Voltage Waveform Characteristics of Plasma Actuators with Different Electrode Geometry for High Performance*.

[44] Jérôme Pons, Eric Moreau, and Gérard Touchard. Asymmetric surface dielectric barrier discharge in air at atmospheric pressure: electrical properties and induced airflow characteristics. *Journal of Physics D: Applied Physics*, 38(19):3635, sep 2005.

[45] J. Reece Roth, Xin Dai, Jozef Rahel, and Daniel Sherman. *The Physics and Phenomenology of Paraelectric One Atmosphere Uniform Glow Discharge Plasma (OAUGDP) Actuators for Aerodynamic Flow Control*.

[46] Luc Leger, Eric Moreau, and Gérard Touchard. *Electrohydrodynamic Airflow Control Along a Flat Plate by a DC Surface Corona Discharge - Velocity Profile and Wall Pressure Measurements*.

[47] Maxime Forte, Jerome Jolibois, Eric Moreau, Gerard Touchard, and Michel Cazalens. *Optimization of a Dielectric Barrier Discharge Actuator by Stattionary and Non-stationary Measurements of the Induced Flow Velocity - Application to Airflow Control*.

[48] C A Shi, K Adamiak, and G S P Castle. Numerical study of the characteristics of a dielectric barrier discharge plasma actuator. *Journal of Physics D: Applied Physics*, 51(9):095201, feb 2018.

[49] Anbang Sun, Chao Huo, and Jie Zhuang. Formation mechanism of streamer discharges in liquids: a review. *High Voltage*, 1(2):74–80, 2016.

[50] Eric Moreau, Pierre Audier, and Nicolas Benard. Ionic wind produced by positive and negative corona discharges in air. *Journal of Electrostatics*, 93:85–96, 2018.

[51] R Valdivia-Barrientos, J Pacheco-Sotelo, M Pacheco-Pacheco, J S Benítez-Read, and R López-Callejas. Analysis and electrical modelling of a cylindrical dbd configuration at different operating frequencies. *Plasma Sources Science and Technology*, 15(2):237, mar 2006.

[52] Anthony Tang, Ravi Sankar Vaddi, Alexander Mamishev, and Igor V Novosselov. Empirical relations for discharge current and momentum injection in dielectric barrier discharge plasma actuators. *Journal of Physics D: Applied Physics*, 54(24):245204, mar 2021.

[53] Dmitriy Roupassov, Andrei Nikipelov, Maria Nudnova, and Andrei Starikovskii. *Flow Separation Control by Plasma Actuator With Nanosecond Pulse Periodic Discharge*.

[54] D. V. Roupassov, A. A. Nikipelov, M. M. Nudnova, and A. Yu. Starikovskii. Flow separation control by plasma actuator with nanosecond pulsed-periodic discharge. *AIAA Journal*, 47(1):168–185, 2009.

[55] Jesse Little, Keisuke Takashima, Munetake Nishihara, Igor Adamovich, and Mo Samimy. *High Lift Airfoil Leading Edge Separation Control with Nanosecond Pulse DBD Plasma Actuators*.

[56] Jesse Little, Keisuke Takashima, Munetake Nishihara, Igor Adamovich, and Mo Samimy. Separation control with nanosecond-pulse-driven dielectric barrier discharge plasma actuators. *AIAA Journal*, 50(2):350–365, 2012.

[57] Keisuke Takashima, Yvette Zuzeek, Walter Lempert, and Igor Adamovich. *Characterization of Surface Dielectric Barrier Discharge Plasma Sustained by Repetitive Nanosecond Pulses*.

[58] Munetake Nishihara, Keisuke Takashima, Joseph Rich, and Igor Adamovich. *Mach 5 Bow shock Control by a Nanosecond Pulse Surface DBD*.

[59] Igor Adamovich, Jesse Little, Munetake Nishihara, Keisuke Takashima, and Mo Samimy. *Nanosecond Pulse Surface Discharges for High-Speed Flow Control*.

[60] T Unfer and J P Boeuf. Modelling of a nanosecond surface discharge actuator. *Journal of Physics D: Applied Physics*, 42(19):194017, sep 2009.

[61] A Yu Starikovskii, A A Nikipelov, M M Nudnova, and D V Roupassov. Sdbd plasma actuator with nanosecond pulse-periodic discharge. *Plasma Sources Science and Technology*, 18(3):034015, jul 2009.

[62] Keisuke Takashima, Zhiyao Yin, and Igor Adamovich. *Measurements and Kinetic Modeling Analysis of Energy Coupling in Nanosecond Pulse Dielectric Barrier Discharges*.

[63] Junbo Deng, Shigeyasu Matsuoka, Akiko Kumada, and Kunihiko Hidaka. The influence of residual charge on surface discharge propagation. *Journal of Physics D: Applied Physics*, 43(49):495203, nov 2010.

[64] M Simeni Simeni, Y Tang, K Frederickson, and I V Adamovich. Electric field distribution in a surface plasma flow actuator powered by ns discharge pulse trains. *Plasma Sources Science and Technology*, 27(10):104001, oct 2018.

[65] Bangfa Peng, Nan Jiang, Zhengyan Liu, Xiaomei Yao, Jie Li, and Yan Wu. Discharge dynamics of primary and secondary streamers in a repetitively pulsed surface dielectric barrier discharge. *Journal of Applied Physics*, 131(11):113301, 03 2022.

[66] K Kourtzanidis, G Dufour, and F Rogier. Self-consistent modeling of a surface ac dielectric barrier discharge actuator: In-depth analysis of positive and negative phases. *Journal of Physics D: Applied Physics*, 54(4):045203, nov 2020.

[67] Kumi Nakai, Asa Nakano, and Hiroyuki Nishida. Validity of three-fluid plasma modeling for alternating-current dielectric-barrier-discharge plasma actuator. *AIAA Journal*, 59(4):1313–1327, 2021.

[68] T Unfer and J-P Boeuf. Modeling and comparison of sinusoidal and nanosecond pulsed surface dielectric barrier discharges for flow control. *Plasma Physics and Controlled Fusion*, 52(12):124019, nov 2010.

[69] Bernard Parent, Kyle M. Hanquist, and Ajjay Omprakas. *Fully-Coupled Simulation of Plasma Discharges, Turbulence, and Combustion in a Scramjet Combustor*. 2020.

[70] S. Sato, M. Takahashi, and N. Ohnishi. *Induced Flow Simulation with Detailed Discharge Modeling in Dielectric-Barrier-Discharge Plasma Actuator*.

[71] I. S. Grigoriev and E. Z. Meilikhov. *Handbook of Physical Quantities*, chapter 20. CRC Press, 1997.

[72] G. W. C. Kaye and T. H. Laby. *Tables of Physical and Chemical Constants*, chapter 4. Longman, 1995.

[73] Y. P. Raizer. *Gas Discharge Physics*. Springer-Verlag, 1997.

[74] A. Murzionak. *Numerical analysis of Dielectric Barrier Discharge Plasma Actuators for supersonic flow applications*. PhD thesis, Carleton University, February 2023.

[75] P. J. Roache. Perspective: A Method for Uniform Reporting of Grid Refinement Studies. *Journal of Fluids Engineering*, 116(3):405–413, 09 1994.

[76] Lewis Fry Richardson and J. Arthur Gaunt. VIII. The deferred approach to the limit. *Philosophical Transactions of the Royal Society of London. Series A, Containing Papers of a Mathematical or Physical Character*, 226(636-646):299–361, 1927.

[77] J. W. Slater. Examining Spatial (Grid) Convergence, 2021. Accessed: 07/04/2024.

[78] M. Abdollahzadeh, J.C. Páscoa, and P.J. Oliveira. Two-dimensional numerical modeling of interaction of micro-shock wave generated by nanosecond plasma actuators and transonic flow. *Journal of Computational and Applied Mathematics*, 270:401–416, 2014. Fourth International Conference on Finite Element Methods in Engineering and Sciences (FEMTEC 2013).

[79] Hiroyuki Nishida and Takashi Abe. Numerical analysis of plasma evolution on dielectric barrier discharge plasma actuator. *Journal of Applied Physics*, 110(1):013302, 07 2011.

[80] Bernard Parent, Mikhail N. Shneider, and Sergey O. Macheret. Sheath governing equations in computational weakly-ionized plasmadynamics. *Journal of Computational Physics*, 232(1):234–251, 2013.